Technical University
of Munich

Max Planck Institute
for Physics
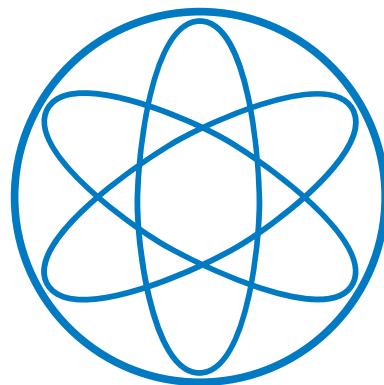
Graduation paper from the Master of Science in Physics

Investigation of the Detector Response to Electrons of the TRISTAN Prototype Detectors

Untersuchung der Detektorantwort auf Elektronen der TRISTAN Prototyp Detektoren

Daniel Benedikt Siegmann
03640314

15 April 2019

Faculty for Physics

Primary reviewer: Prof. Dr. S. Mertens
Supervisors: Tim Brunst
Secondary reviewer: Prof. Dr. S. Schönert

Abstract

Sterile neutrinos are a minimal extension to the standard model of particle physics and can tackle a large number of open questions. One of them is the composition of dark matter in the universe, which could be explained by sterile neutrinos in the kilo-electron-volt mass range. Laboratory experiments that measure β-decay spectra to a high precision can be sensitive to these particles, since their mass eigenstate would manifest itself as a kink-like structure in the spectrum. To measure this imprint of sterile neutrinos the TRISTAN project aims to extend the KATRIN setup with a sophisticated multi-pixel detector system, which can handle high rates with an excellent energy resolution.

In the scope of this thesis, the first TRISTAN silicon drift detector prototypes were characterized with electrons. For this purpose a scanning electron microscope that can produce electrons between $0.5\,\mathrm{keV}$ and $30\,\mathrm{keV}$ has been used. Since the entrance window thickness of the silicon drift detectors influences the shape of the detector response, this detector property had to be minimized in the detector fabrication process and measured precisely. To achieve this goal, two measurement techniques were developed and compared to estimate the thickness of the entrance window. The first method uses the overall energy shift between the deposited energy in the sensitive detector volume and the true incoming energy to determine the entrance window thickness. For the second method the detector has been tiled, which artificially increases effective entrance window thickness. This change of the effective entrance window is measured by an energy shift of the spectrum and is then correlated to the entrance window thickness. For both methods the entrance window is modeled as a completely dead layer. In the results presented in this thesis both methods are in good agreement with each other.

For the standard detector technology a dead-layer thickness of $(52\pm7)\,\mathrm{nm}$ were measured. Additionally, two detectors with different entrance window technologies were investigated. Nevertheless, no major advantage of these detectors for the TRISTAN project were found.

The first steps to model the response of the detector with Monte Carlo simulations of electrons in silicon were performed. In addition to this an empirical model was developed to describe the response with analytic functions.

Contents

1 Introduction to Neutrino Physics

The properties of neutrinos are one of the main questions of modern particle physics. They take a unique role in the Standard Model, since they only interact via the weak interaction and investigations of their mass and the possibility of them being Majorana particle are topic of current experiments.

To give insight to neutrino physics a brief introduction is given in this chapter, starting with the weakly interacting neutrinos, also called left-handed or active neutrinos. Thereby, the theory of the massless neutrino in the standard model and its extension to neutrinos with a mass, predicted by neutrino oscillations, is discussed. Section 1.1.4 briefly reviews some experimental methods to determine neutrino mass.

The second part of this chapter focuses on the theory of sterile neutrinos which can be right-handed. In detail the motivation, coming from particle physics and cosmological observations, for these particles is discussed in section 1.2.1 and 1.2.2. The main focus is set on keV-sterile neutrinos and current constrains by cosmology.

1.1 Active Neutrino Physics

At the beginning of this section, a brief summary of the discovery of the neutrino will be given, which leads to the role of neutrinos in the Standard Model. First, neutrinos are assumed to be massless, even though neutrino oscillations demonstrate that neutrinos have a non-zero mass as described in section 1.1.3. Experiments to measure the neutrino mass are described in section 1.1.4.

1.1.1 Brief Summary of the Discovery of Neutrinos

In 1930, the neutrino was first postulated by Wolfgang Pauli to explain the continuous spectrum observed in β-decays. The observed spectrum contradicted the well understood mono-energetic lines seen in α- and γ-decays. The predicted particle had to be orders of magnitudes lighter than the nucleus and the electron, while it also had to be electrically

neutral to explain the decay.[1]

Frederick Reines and Clyde Cowan detected the (electron anti-) neutrino via the inverse β-decay process in 1955.

$$\overline{\nu}_e + p \longrightarrow e^+ + n \tag{1.1}$$

To obtain an intense anti-neutrino flux, they built their detector next to the Savannah River reactor. The detector consisted of a water tank and scintillators to detect the γ-rays created by the annihilation of the positron. An additional signal of photons with an energy of $2.2\,\text{MeV}$ is created by capturing the neutron on cadmium in water. This process occures with a time delay of $200\,\text{ns}$. With this coincident signal the inverse β-decay could be detected and the observed cross section agreed with the prediction by weak interaction theory [2].

In addition to the detection of the electron anti-neutrino, the team led by Leon Ledermann, Melvin Schwartz and Jack Steinberg could show that more than one flavor of neutrinos exists. In 1962, they used the decay of charged pions to produce muons and their associated neutrino ν_μ. The third type of neutrino was discovered at the Stanford Linear Accelerator Center in 1975 and was identified as the tau neutrino ν_τ.

Studies on the decay of the Z-boson could determine the total number of light neutrinos. The total decay width Γ_Z of the Z^0-resonance includes the hadronic decay width Γ_{had} ($Z^0 \rightarrow q\overline{q}$), the common partial leptonic width Γ_l ($Z^0 \rightarrow l\overline{l}$) for the charged leptons and the invisible width $\Gamma_{inv} = N_\nu \cdot \Gamma_\mu$ for the neutrinos. From a combination of experiments at the Large Electron-Positron Collider at CERN, the number of light neutrinos has been obtained as $N_\nu = 2.9841 \pm 0.0083$ [3], which is in excellent agreement with the theoretical expectation of three light active neutrinos[2].

1.1.2 Neutrinos in the Standard Model

The Standard Model of particle physics includes six quarks of different flavors and three charged leptons, which all exist with left- and right-handed chirality. In addition to these fermions three neutral leptons, the neutrinos, are included with the same flavors as their charged leptonic partners. The model for all fermions can be seen in figure 1.1. In the further discussion only particles will be treated, even though the arguments can easily be transferred to their anti-partner.

Neutrinos are unique in the standard model in such a way that they solely interact through the weak interaction.[4] Since the weak interaction only couples to left-handed particles and neutrinos are electrically neutral, a right-handed neutrino would not interact at all.
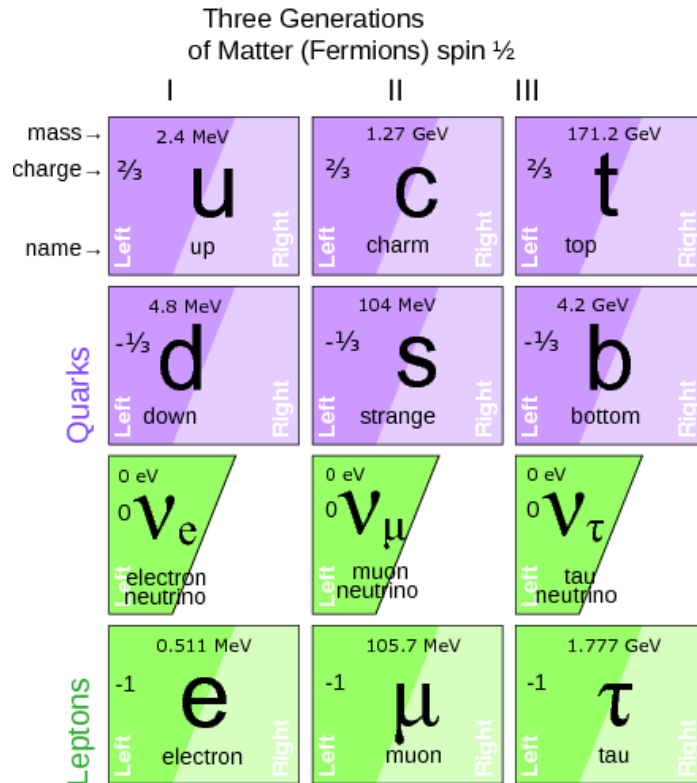
FIGURE 1.1: **Standard model of elementary particle physics for fermions**
In purple the six quarks are shown with left- and right-handed chirality, while all known leptons are marked in green. The charged leptons are represented in both chirality states like the quark, in contradiction to neutrinos, which are introduced in the Standard Model as massless and only left-handed. (Scheme adapted from [5])

Therefore, neutrinos can only exist as left-handed particles in this model.

1.1.3 Neutrino Oscillations

In the 1960s, the first neutrino detectors that could measure neutrinos from the sun were built. The measurements performed by experiments like the Homestake experiment [6] by Ray Davis observed a deficite of a factor of three of the neutrino flux from the sun with respect to the predictions. This lead to the so-called solar neutrino problem in the late 1960s. These oberservations were confirmed by various experiments with different detector technologies like the experiments GALLEX [7] and Super-Kamiokande [8].

With the SNO Experiment [9] around the turn of the millennium, it was possible to measure all neutrino flavors via the neutral current interactions. The total neutral rate was in agreement with the solar model, only the flavor was not in accordance, what can be explained by the capability of neutrinos to change their flavor on the way between the

sun and the earth.

This phenomenom is called neutrino oscillation and is further confirmed by the observations of reactor, accelerator and atmospheric neutrinos [10]. The oscillation is raised by the mixing between the flavor and the mass eigenstates of neutrinos. Neutrinos are produced and interact in their flavor eigenstates $(\nu_e, \nu_\mu, \nu_\tau)$ of the weak interaction, but they propagate in their mass eigenstates (ν_1, ν_2, ν_3). To connect the two different types of eigenstates the **P**ontecorvo–**M**aki–**N**akagawa–**S**akata (PMNS) matrix can be introduced.

$$\underbrace{\begin{pmatrix} \nu_e \\ \nu_\mu \\ \nu_\tau \end{pmatrix}}_{\text{flavor eigenstates}} = \underbrace{\begin{pmatrix} U_{e1} & U_{e2} & U_{e3} \\ U_{\mu1} & U_{\mu2} & U_{\mu3} \\ U_{\tau1} & U_{\tau2} & U_{\tau3} \end{pmatrix}}_{\text{PMNS matrix}} \cdot \underbrace{\begin{pmatrix} \nu_1 \\ \nu_2 \\ \nu_3 \end{pmatrix}}_{\text{mass eigenstates}} \tag{1.2}$$

The PMNS matrix for three neutrinos can be parameterized to three mixing angles $(\theta_{12}, \theta_{13}, \theta_{23})$ and a phase δ_{CP}. In the following the probability to oscillate from flavor eigenstate α to the then measured eigenstate β is given by (1.3). For simplicity reasons only the two-flavor case is shown, but it can be further extended to more flavors.

$$P_{\alpha \to \beta} = \sin^2(2\theta) \cdot \sin^2 \left(\frac{1.27 \cdot \Delta m^2 [\,\text{eV}^2] \cdot L [\,\text{km}]}{E_\nu [GeV]} \right) \tag{1.3}$$

L denotes the traveled distance and E_ν gives the energy of the neutrino, while the mixing angle between the mass eigenstates is given by θ. $\Delta m^2 = m_2^2 - m_1^2$ is assigned to the difference of the squared masses of the mass eigenstates. If neutrinos were massless $\Delta m = 0$, no oscillation would be possible. Hence neutrinos have to have mass.

1.1.4 Direct Neutrino Mass experiments

With the discovery of neutrino oscillations, it is clear that neutrinos have to be massive. Nevertheless, oscillations reveal only the mass differences Δm_{ij} and the mixing angles θ_{ij} but are not capable of measuring the absolute mass of the neutrino mass eigenstates.

From cosmological models, limits to the neutrino masses can be set. Nevertheless since they depend on more parameters than the neutrino masses itself, the focus of this thesis will be on the direct measurement techniques in laboratory based experiments.

Single β-decay

One approach to measure the effective mass of the electron anti-neutrino are single β-decay experiments. Here the energy of β-decay electrons from e.g. tritium are measured

precisely close to their kinematic endpoint, as it depends on the neutrino mass and is shifted to lower energies compared to the massless case. The current resolution of the measurement of the endpoint of the spectrum is not precise enough to resolve all three mass eigenstates. Therefore, the effective electron anti-neutrino mass is introduced.

$$m_{\nu_e} = \sqrt{\sum_i m_i^2 |U_{ei}|^2} \leq 2.05 \,\text{eV} \qquad (1.4)$$

Examples for experiments that measured the (single) β-decay precisely are the Mainz [11] and Troisk Experiment [12] that set the current best limit for the effective electron anti-neutrino mass of $2 \,\text{eV}$ (95%C.L.) [12] [11]. The **KA**rlsruher **TRI**tium **N**eutrino (KATRIN) experiment [13] is expected to surpass this limit in the next years to reach a sensitivity of

$$m_{\nu_e} \leq 0.2 eV \ (90\% \ \text{C.L.}) \qquad (1.5)$$

Neutrinoless double β-decay ($0\nu\beta\beta$)

Another method to measure the neutrino mass is the neutrinoless double β-decay ($0\nu\beta\beta$). This process is forbidden in the Standard Model due to the violation of the total lepton number and is only feasible, if the neutrinos are Majorana particles and therefore their own anti-particles.

For this second-order weak interaction process the nuclei has to have an even proton number Z and even neutron number N where the singe β-decay is energetically forbidden. The discovery of the hypothetical $0\nu\beta\beta$-decay would be a direct detection of physics beyond the Standard Model and prove that neutrinos are Majorana particles. In addition to this, the effective Majorana mass m_{ee} of the neutrino could be observed by the half-life of the decay [15].

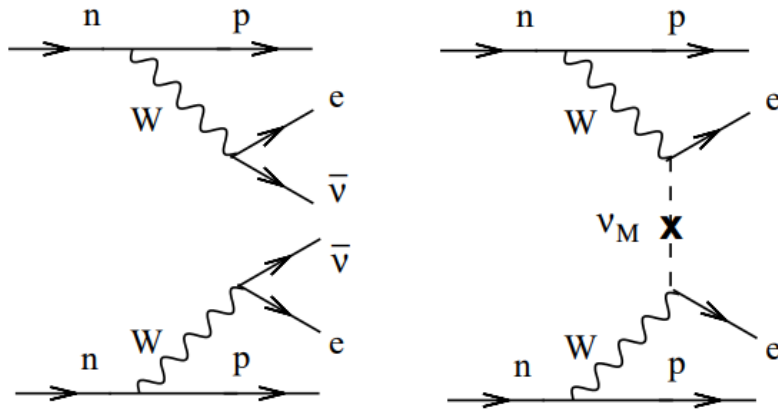$$m_{ee} = \left| \sum_{i=1}^{3} U_{ei}^2 m_i \right| \qquad (1.6)$$

FIGURE 1.2: **Feynman diagrams for double β-decays**
On the left-hand side the Feynmann diagram for the double β-decay ($2\nu\beta\beta$) is shown. The right-hand side demonstrates the neutrinoless double β-decay ($0\nu\beta\beta$). In this case the neutrino has to be its own anti-particle and is therefore a Majorana particle.(Scheme adapted from [14])

1.2 Sterile Neutrino Physics

As shown in section 1.1.2 neutrinos take a unique role in the Standard Model, as they are introduced only with left-handed chirality, while all the other leptons can have both. A natural extension to this model are right-handed neutrinos. Since neutrinos only interact with the weak force a right-handed neutrino would not interact at all, except of the mixing to (left-handed) active neutrinos. Therefore this kind of neutrinos is also called sterile neutrino.

This expansion of the Standard Model is shown in figure 1.3 where now all fermions would have left- and right-handed partners, which would mace the families of fermions more uniform between each other. In addition to this 'natural' extension, sterile neutrinos could explain the lightness of the active neutrinos and are also dark matter candidates. In the following sections, these topics are briefly discussed. The main focus will be set on hypothetical keV-sterile neutrino, which the TRISTAN project aims to look for.

1.2.1 Motivation from Particle Physics

One motivation for right-handed neutrinos is that their existence can introduce mass for neutrinos. This is accomplished by adding a mass-term to the Standard Model Lagrangian. The combination of the left- and right-handed neutrino with the Higgs field leads to a Dirac mass-term for neutrinos to give them mass, similar as for the other fermions in the Standard Model. Taking into account the current limits for the neutrino
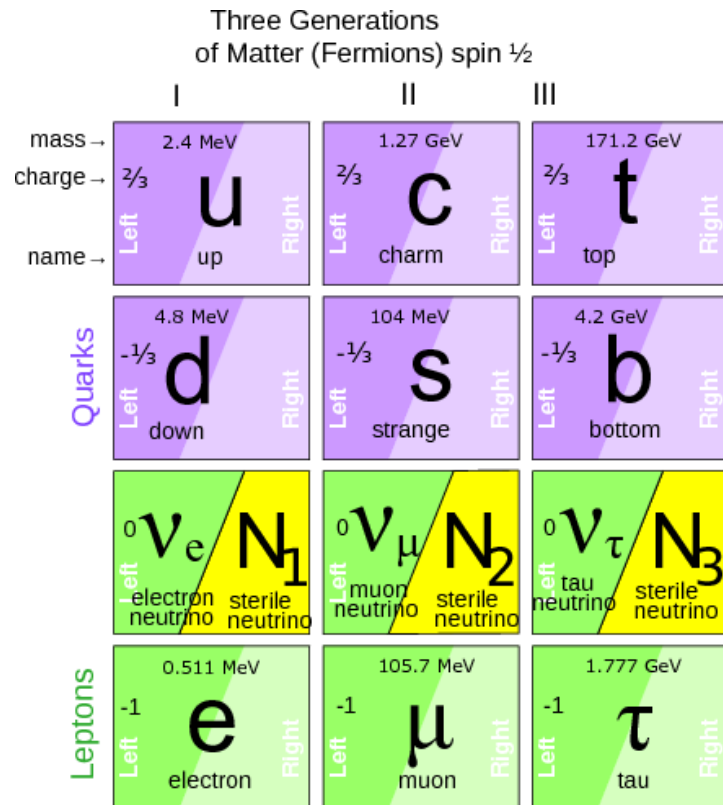
FIGURE 1.3: **Standard model of elementary particle physics for fermions in addition of three sterile neutrinos**
In purple the six quarks are shown with left- and right-handed chirality, while all known leptons are marked in green and are also represented in both chiral states. In addition to the known neutrinos three right-handed neutrinos are in yellow. (Scheme adapted from [5])

mass of $2\,\mathrm{eV}$ this requires a Yukawa coupling in the order of 10^{-12}, which is five orders of magnitude smaller than the coupling for electrons.

Another way to introduce mass for neutrinos is described by the See-Saw mechanism. For this model, the neutrino is assumed to be a Majorana particle, with the possibility of a transition from a neutrino to an anti-neutrino. By allowing this, the neutrino mass matrix for a single generation can be written with the Dirac mass term m_D and a Majorana mass term m_R as seen in equation 1.7.

$$M = \begin{pmatrix} 0 & m_D \\ m_D & m_R \end{pmatrix}, \quad \lambda_1 \approx m_R, \quad \lambda_2 \approx \frac{-m_D^2}{m_R} \tag{1.7}$$

The diagonalization of M leads to the eigenvalues λ_1 and λ_2. These eigenvalues are proportional to the physical neutrino masses. Introducing a heavy Majorana mass m_R in the order of GeV or higher could explain the lightness of the active neutrino, as the other mass-eigenvalue λ_2 is inverse proportional to m_R.

1.2.2 Motivation from Cosmology

Recent observations of the Planck satellite show that the universe is composed of about 68% dark energy, 27% dark matter and 5% baryonic matter. This raises the question about the composition and origin of dark energy and dark matter. The term dark energy describes an unknown form of energy, which is hypothesized to be the reason for the accelerated expansion of the universe and will not be discussed in this thesis. Dark matter on the other hand is defined as a form of matter that is non-luminous and only interacts weakly. For this dark matter the Standard Model does not provide any suitable candidates that are electrically neutral and stable with respect to the age of the universe. In this thesis, keV-sterile neutrinos will be discussed as dark matter candidates.

The possibility that active neutrinos explain dark matter is firmly ruled out, since they form **H**ot **D**ark **M**atter (HDM) which leads to a washing-out of small scale structures. This disagrees with observations on the scale of galaxies. Currently the best agreement of observation and simulation is obtained with **C**old and **W**arm **D**ark **M**atter (CDM and WDM)[16].

Sterile neutrinos in the mass range of $\mathcal{O}(\mathrm{keV})$ are candidates for both warm and cold dark matter. Both scenarios fit equally well on large scale structures of the size of galaxy clusters and larger. On smaller scales, the observation of dwarf galaxies and the galactic density profiles fit better to the WDM model and solve many of the existing tensions of the CDM model[17].
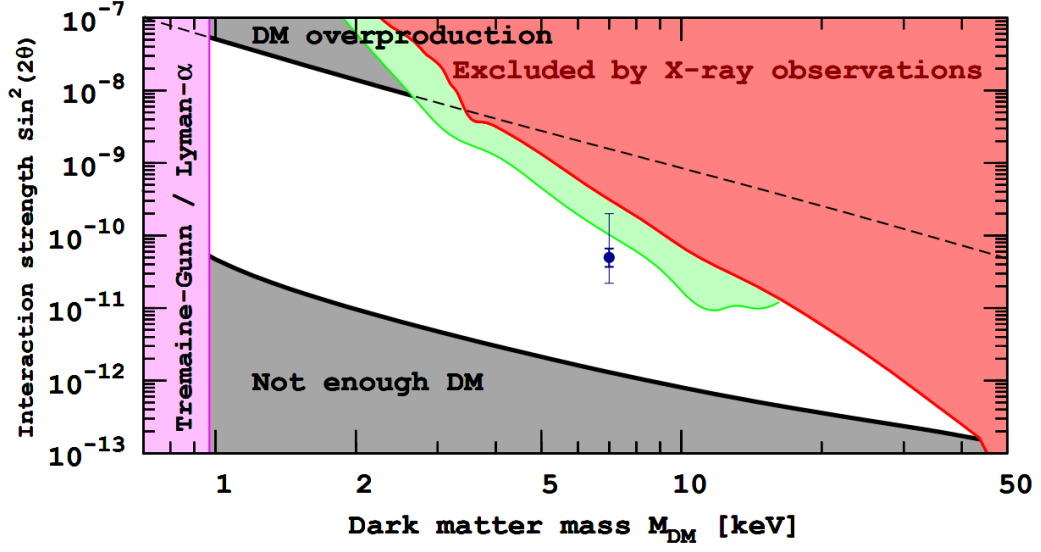
FIGURE 1.4: **Constraints on the sterile neutrino dark matter mass and mixing angle**
The white area describes the allowed area for the case where the sterile netrino contributes to
100% to dark matter. The grey area is excluded due to an overproduction or underproduction
of dark matter in the early universe. In purple the constraints from the observation of the
Lyman-α forest and the Tremaine-Gunn bound is shown. The red and green area is excluded
due to the non-observation of the decay of sterile neutrinos seen in mono-energetic X-ray
lines. The blue data point corresponds to a controversial unidentified $3.5\,\text{keV}$ emission line in
stacked galaxy cluster measurements. (Plot adapted from [19])

Astronomical observations set further constraints on the allowed parameter space of the
sterile neutrino mass m_s and the mixing angle θ_s. This can be seen in figure 1.4. The
white region describes the allowed keV-sterile neutrino parameter space for the case in
which sterile neutrinos form the entire dark matter. Calculations of the formation of the
early universe set constraints to this parameter space due to over- or underproduction of
dark matter for very large and small mixing angles. In addition to these confinements
from the model of the early universe, a robust and model-independent bound is given
by the phase space density of fermionic dark matter, which has to be smaller than the
density of a degenerated Fermi gas [18]. Therefore, a lower limit of $m_s > 1\text{keV}$ can be set.
The non-observations of mono-energetic X-ray lines originating from the decay of sterile
neutrinos to an active neutrino and a photon set further bounds on the allowed parameter
space.

The combination of all these constraints lead to a partly model-dependent but stringent
allowed parameter space of $1\,\text{keV} < m_s < 50\,\text{keV}$ and $10^{-13} < \sin^2(2\theta_s) < 10^{-7}$. [16]

2 keV-Sterile Neutrino Search in a KATRIN-like Experiment

Sterile neutrinos could manifest themselves in β-decay spectra as a kink like structure. In this chapter the KATRIN experiment is introduced, since it has, next to the measurement of the effective neutrino mass m_{ν_e}, the potential to search for sterile neutrinos. To accomplish this task, a detector upgrade after its measurement phase for the neutrino mass is required. The requirements to build such a novel detector system are presented in section 2.3.

2.1 KATRIN Experiment

The KATRIN experiment is a tritium β-decay experiment, using a **M**agnetic **A**diabatic **C**olliminator and **E**lectrostatic high-pass filter (MAC-E). It is designed to measure the effective electron anti-neutrino mass seen in equation (1.4). The effect of the neutrino mass on the energy spectrum of tritium is a shift of the endpoint energy Q of the electrons as illustrated in figure 2.1.

KATRIN is designed to reach a sensitivity of 200 meV at 90% confidence level (C.L.) for the effective neutrino mass m_ν[13]. In this chapter, the major components of the KATRIN experiment shown in figure 2.2 are shortly introduced. For a more detailed explanation refer to the KATRIN design report [13].

2.1.1 Windowless Gaseous Tritium Source

The **W**indowless **G**aseous **T**ritium **S**ource (WGTS) provides an ultra stable and highly luminous gaseous tritium source. The tritium gas with a purity of more than 95% is continuously injected into the source and monitored to keep the decay rate stable at 10^{11} decays per second wit a maximal variation of 0.1% [13]. This leads to a throughput of 40 g of tritium per day. To ensure a high tritium density for the rate and a reasonable pressure to reduce the Doppler broadening, the source is cooled to 30 K with a stability
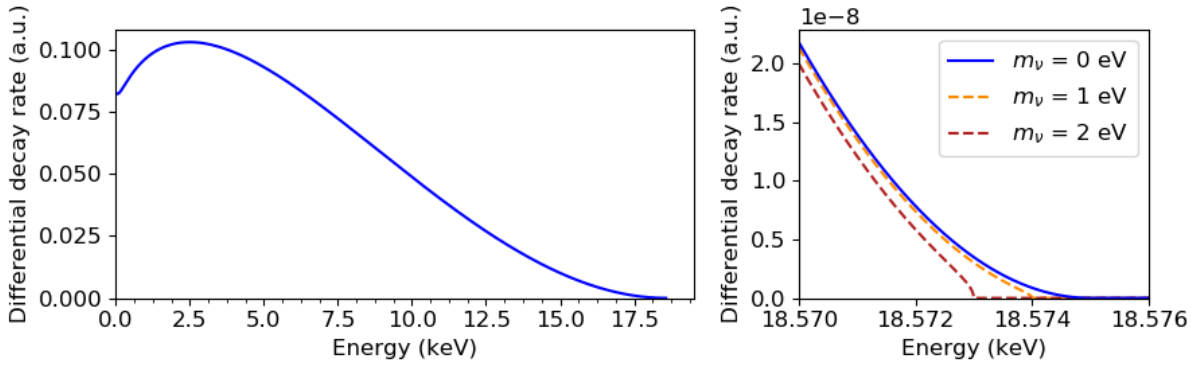
FIGURE 2.1: **Theoretical differential tritium β-decay spectrum**
In blue the tritium spectra with a neutrino mass of $m_\nu = 0\,\text{eV}$ is shown. A zoom on the endpoint region with various effective neutrino masses m_ν is shown on the right-hand side. (Plot adapted from [20])
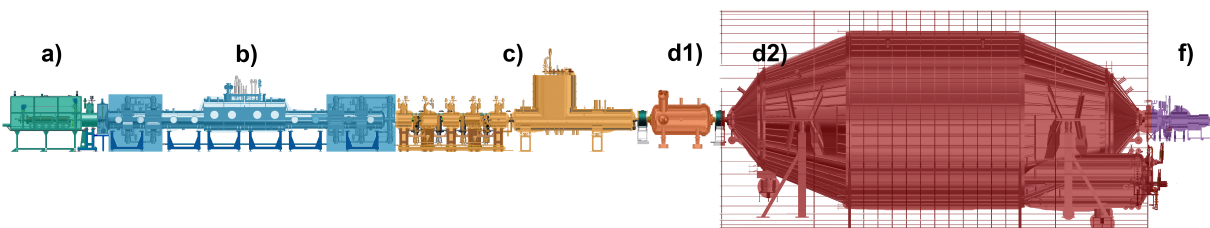

FIGURE 2.2: **Schematic of KATRIN Experiment**
a) rear section, b) **W**indowless **G**aseous **T**ritium **S**ource (WGTS), c) transportation section, d1) pre-spectrometer, d2) main spectrometer, f) **F**ocal **P**lane **D**etector (FDP) (Scheme adapted from [21])

of 0.1%.

The gas gets injected in the center of the WGTS and streams freely to both ends. Here, the tritium gets pumped away by multiple turbo-molecular pumps and later is re-injected after passing through a sophisticated process of purification and cleaning performed in the looped system of the **K**arlsruher **T**ritium **L**aboratory (TLK) [22][13].

2.1.2 Transport and Pumping Section

The tritium in the WGTS must not reach the spectrometer, as it would create a mayor source of background. To prevent this, the **D**ifferential and **C**ryogenic **P**umping **S**ections (DPS and CPS) reduce the tritium flow continuously by 14 orders of magnitude. The DPS decreases it by five orders of magnitude with four differential turbo-molecular pumps. The remaining tritium is then trapped in the CPS by cryo-absorption on argon frost with a temperature of $3\,\mathrm{K}$.

Additionally, the transport section is built in a chicane shape to further prevent that neutral molecules enter the spectrometer. Using these techniques, it is possible to guide the electrons from the source to the spectrometer without passing any solid divider where they could lose energy.

2.1.3 Spectrometers

The main spectrometer is a large MAC-E filter. A negative electrical potential in the middle of the spectrometer at an energy qU filters the electrons by their energy like a high-pass filter. Electrons with lower energy will be reflected by the electric field, while electrons with higher energy will overcome the potential and make their way to the detector. Because the electrons are guided along magnetic field lines, they perform a cyclotron motion as shown in figure 2.3. There momentum is therefore not parallel to the electric field lines and electrons can be rejected even though they would have enough energy. To minimize this effect, a gradient in the magnetic field is created by setting the magnetic field of the source B_S and the detector B_D to several magnitudes higher values than the magnetic field B_{min} in the middle of the spectrometer. This performs an adiabatic transformation of the orthogonal part of the electron's momentum $p_\perp$ to the parallel momentum $p_\parallel$. This behavior can be seen at the bottom of figure 2.3. The energy resolution ΔE of the MAC-E filter is given by

$$\frac{\Delta E}{E} = \frac{B_{\mathrm{Min}}}{B_{\mathrm{Max}}} \tag{2.1}$$
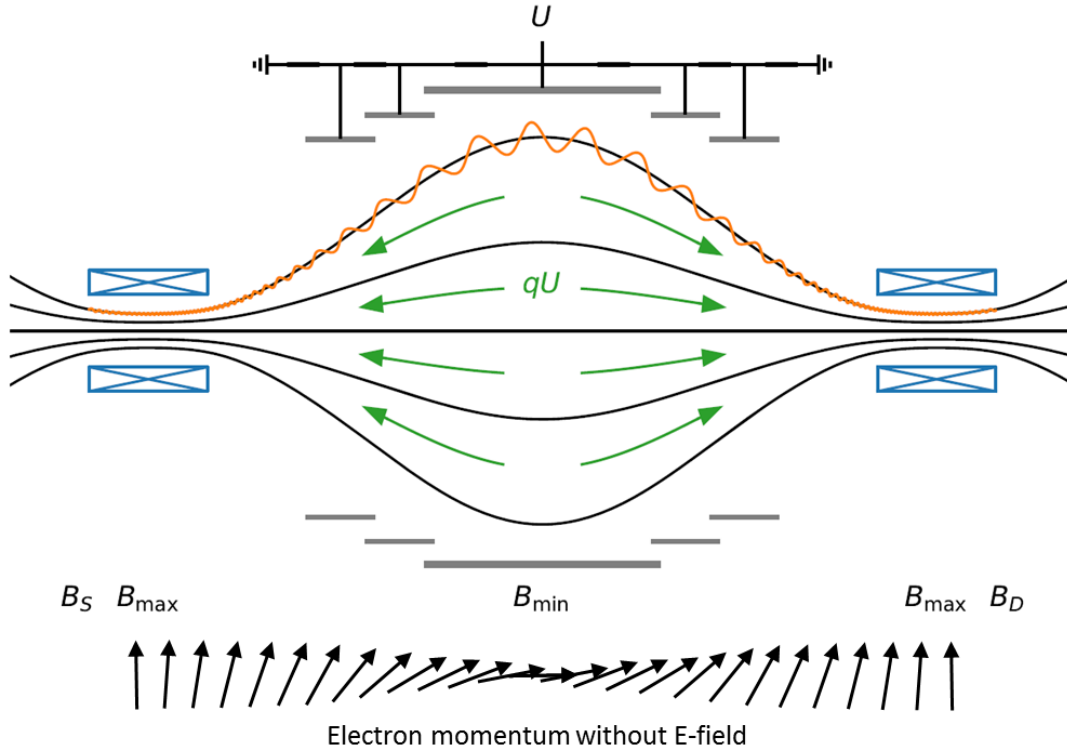
FIGURE 2.3: **Working principle of a MAC-E filter**
The black lines illustrate the magnetic field lines between the two pinch magnets in blue. The electric field is represented by the green arrows with the maximal potential in the middle of the Spectrometer. In orange the cyclotron motion of an exemplary electron along the magnetic field lines is shown. The change of the momentum for the electrons through the spectrometer can be seen at the bottom. (Scheme adapted from [22])

Since the magnetic flux $\Phi = B \cdot A$ is constant, the spectrometer must be larger than the source. The dimensions of the main spectrometer of 23.28 m length and a diameter of 9.8 m in the cylindrical section allow an excellent energy resolution of about 1 eV [13] for magnetic fields of $B_{max} = 6\text{T}$ and $B_{min} = 3 \cdot 10^{-4}\,\text{T}$.

The common operation mode for KATRIN is an integral measurement, meaning that the count rate for different retarding potentials qU of the MAC-E filter is measured.

2.1.4 Focal Plane Detector

The **F**ocal **P**lane **D**etector (FPD) is positioned downstream the main spectrometer. It is segmented into 148 pixels to account for the radial dependence of the incoming electrons. The detector consists of an monolithic silicon p-i-n diode, whose working principle is explained in chapter 3.1. The detector is grouped into 12 concentric rings of each 12
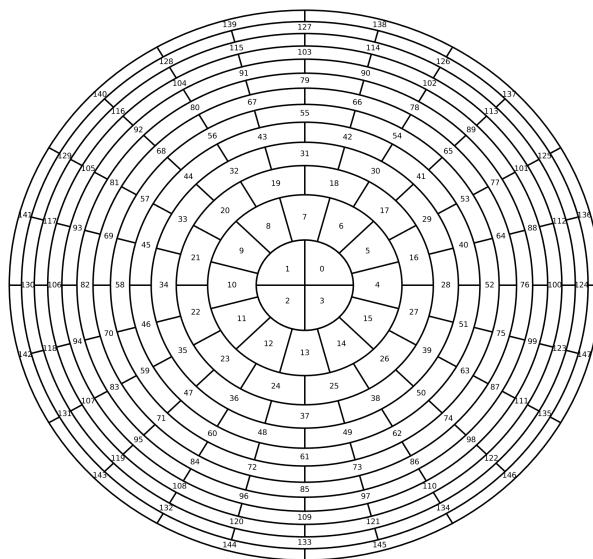
FIGURE 2.4: **Pixel layout of Focal Plane Detector (FPD)**
The detector is segmented into 12 rings with each 12 segments and the bullseye in the middle with four segments. Resulting in 148 segments of same size. (Layout adapted from [21])

TABLE 2.1: **Table of measured and calculated properties for the FPD[23]**

Detector Property 1	Value
Waver thickness	$503\,\mu$m
Dead layer thickness ('insert-slap')	$(155 \pm 0.5_{stat} \pm 2.2_{sys})\,$nm
Detection efficiency	$(95 \pm 1.8_{stat} \pm 2.2_{sys})\%$
Energy resolution (FWHM) at $18.6\,$keV	$(1.52 \pm 0.01)\,$keV
Detector capacity	$8.2\,$pF (design value)
Energy threshold at shaping time $0.8\,\mu$s	$\approx 8.5\,$keV
Energy threshold at shaping time $6.4\,\mu$s	$\approx 4.0\,$keV

segments and a bulls-eye of four pixels in the middle. The diameter of the detector is $90\,$mm and each pixel has a size of $44\,$mm^2. Further properties of the detector can be seen in table 2.1.

Since the energy resolution is given by the MAC-E filter and the region of interest is the energetic endpoint of the tritium spectrum, the FPD is designed to reliable detect electrons at low rates. The current read-out speed allows a maximal rate of $62\,$kcps for the entire detector (i.e. ≈ 420 cps per pixel) [23].

In the operated integral mode of KATRIN this read-out speed is adequate. However, for possible future measurements of sterile neutrinos in the decay spectra of tritium it is of significant importance to handle much higher rates to scan deeper into the spectrum. This topic is discussed in the next section.

2.2 Imprint of Sterile Neutrinos in β-Decay Spectra

As described in sections 1.1.4 and 2.1, the mass eigenstates ν_1, ν_2 and ν_3 of the neutrino show an (effective) imprint of themselves near the endpoint Q of the spectrum. A similar imprint could be seen for the addition of a fourth mass eigenstate ν_4 resulting in an additional sterile neutrino flavor ν_s. The effect on the spectra is described in equation 2.2 and can be seen largely amplified in figure 2.5.

$$\frac{d\Gamma}{dE} = \underbrace{\cos^2\left(\frac{d\Gamma}{dE}\right)_{m_{\nu_e}} \Theta(E_0 - E - m_{\nu_e})}_{\text{Active neutrino part}} + \underbrace{\sin^2\left(\frac{d\Gamma}{dE}\right)_{m_s} \Theta(E_0 - E - m_s)}_{\text{Sterile neutrino part}} \quad (2.2)$$

The kinetic energy of the emitted electron is described as E and the endpoint of the spectrum as E_0. The mixing angle between sterile and active neutrino is denoted as θ. The superposition of the effective neutrino spectra and the sterile spectra would lead to a kink at an energy of $E_0 - m_s$.

One of the main advantages of the KATRIN experiment is the strength of the high-luminous tritium source in the WGTS. The endpoint energy of $E_0 = 18.6\,\text{keV}$ would theoretically allow the investigation of sterile neutrino masses up to this value. Sensitivity studies that fit the entire tritium spectrum, including a keV-sterile neutrino, show a possible statistical sensitivity with the KATRIN framework to mixing angles of $\sin^2(\theta) = 10^{-6}$ to 10^{-8}[24] which can be seen as well in figure 2.6. The study is performed for two working modes of KATRIN, the integral measurement as described before, with the variation of the retarding potential qU, only scanning to lower energies where the energy resolution is given by the MAC-E filter and the detector only counts the arriving electrons. For the differential mode the MAC-E filter is turned off or set to a fixed retarding potential qU. Therefore the resolution is completely given by the detector. The sensitivity study [24] shows that the imprint of the kink-like structure is stronger for the differential mode. Using the current source strength of KATRIN of $N = 8.3 \cdot 10^{18}$ decays in three years the limits set by cosmology can be cross-checked and even further improved.
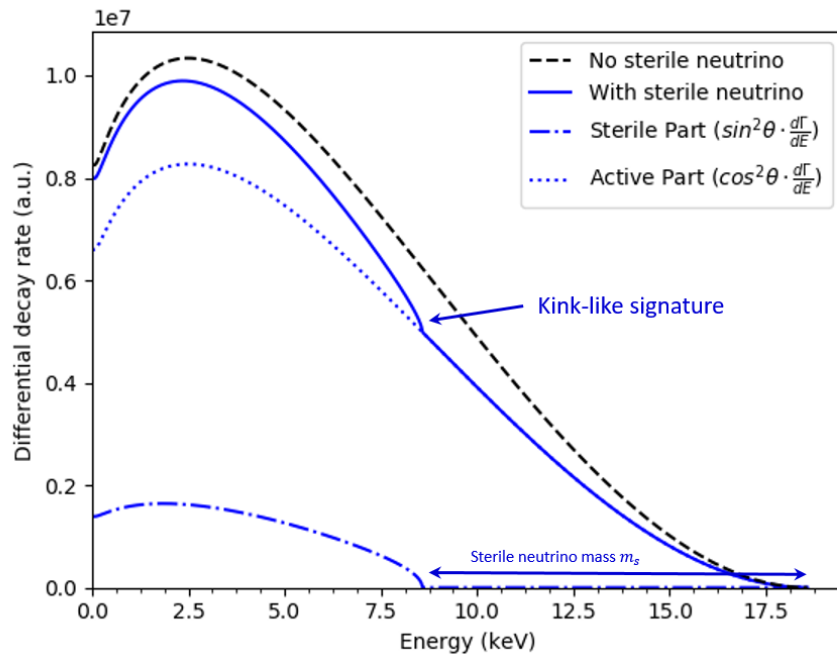
FIGURE 2.5: **Signature of sterile neutrino in differential tritium spectrum**
The theoretical differential tritium β-decay spectrum without any sterile neutrino is represented in black. In blue a total spectrum with a sterile neutrino of mass $m_s = 10\,\mathrm{keV}$ and an unreasonably high mixing angel of $\sin^2(\theta) = 0.2$ is shown. The dotted blue lines mark the sterile part and the active part of the spectrum. (Plot adapted from [20])
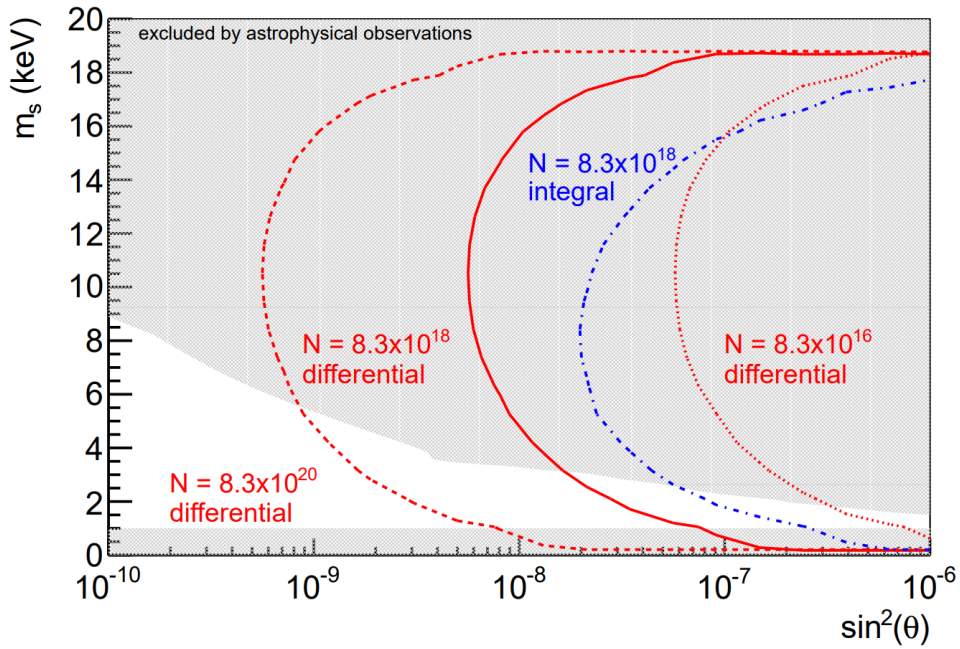
FIGURE 2.6: **Statistical sensitivity plot for sterile neutrino parameters**
The statistical exclusion plot limits for both differential and integral measurement at 90%C.L. within three years of measurement for a generic detector efficiency of 90% are shown in this plot. The solid red and blue lines correspond to the sensitivity using the designed source strength (total decays $N = 8.3 \cdot 10^{18}$ in three years) of KATRIN for a differential and integral measurement. In gray the exclusions from cosmology are shown. (Plot adapted from [24])

2.3 Requirements to a Novel Detector System

Since the current detector system for KATRIN has been designed for an active neutrino search, it does not fulfill most of the requirements set for the search for sterile neutrinos. Therefore, the **TR**itium **I**nvetigations of **ST**erile to **A**ctive **N**eutrino mixing (TRISTAN) project has been created to developed a novel detector system that can handle the necessary requirements for the sterile neutrino search with KATRIN. Since the demands to the detector system for the differential mode are higher, the requirements for a detector operation in the differential mode is discussed. Nevertheless, such a detector can be used in the integral mode as well. The technology of silicon drift detectors is a promising candidate to fulfill all requirements for the keV-sterile neutrino search. Therefore they will be discussed with this detector type in mind.

To reach a statistical sensitivity to the mixing angle $\sin^2(\Theta)$ and sterile mass m_s of interest as shown in figure 2.6 a strong source is required. The designed source strength of KATRIN results in approximately one electron per second at the detector, for an retarding potential qU set to one electron volt above the endpoint Q. For the TRISTAN Project this will rise to more than 10^{10} electrons per second at the designed KATRIN source strength. To handle such high rates it is required to distribute the overall rate among many pixel. In addition to this it is necessary for the readout system to perform at small shaping times τ to reduce the effect of pile-up and increase the rate that can be handled.

The second major requirement of the TRISTAN project is the precise understanding of the entire spectra, to probe the parameter space for mixing angles $\sin^2(\theta_s)$ of cosmological interest. To accomplish this, the entire spectrum has to be understood to the **p**arts-**p**er-**m**illion (ppm) level, which can only be achieved with an excellent energy resolution and a precise understanding of the detector response. If the energy resolution is too bad, this feature will be washed-out. The sensitivity studies described in chapter 2.2 suggest an energy resolution better than $300\,\mathrm{eV}$ at $20\,\mathrm{keV}$ to detect the kink-like feature.

As one can see in equation (2.3) these two requirements are liked together, since the serial or voltage noise Q_{series}, and therefore the energy resolution, is anti proportional to the shaping time τ [25].

$$Q_{\mathrm{series}} = \sqrt{4kTR_s + e_{na}^2} \cdot \frac{C_d}{\sqrt{\tau}} \tag{2.3}$$

Therefore all other parameters that influence this correlation have to be as small as possible. One crucial parameter is the capacity C_d of the detector, which can be very small
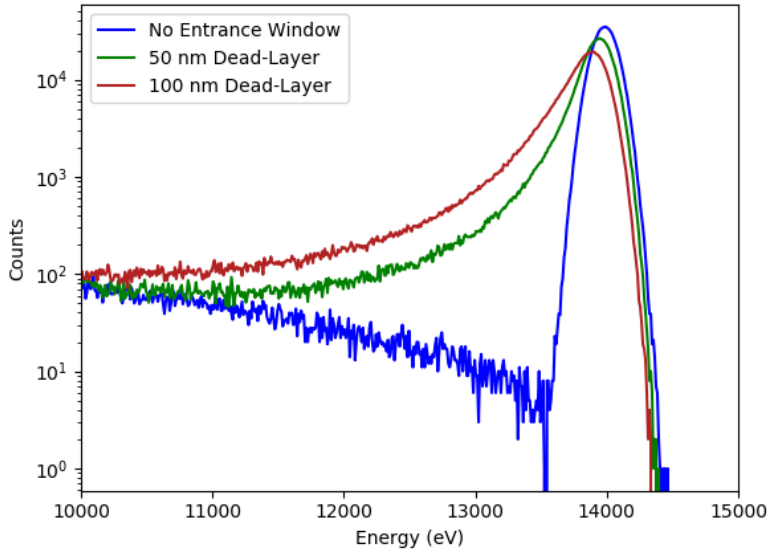
FIGURE 2.7: **Visualization of dead-layer effects on the energy spectrum**
The simulation of the energy spectrum for mono-energetic electrons with $14\,\text{keV}$ interacting with a silicon detector are represented. For the simulation an Noise with a FWHM of $220\,\text{eV}$ is assumed and electrons can back scatter and leave the detector as well. In blue the energy spectrum without any effects by the entrance window is shown. In green and red the same simulation with effects by an dead-layer is shown. The simulation is performed with the simulation software KESS [26].

for silicon drift detectors down to $C_d = 110\text{fF}$. In addition to this the noise e_{na} coming from the amplifier has to be small. Cooling to lower Temperatures T can further decrease the overall noise in the system and allows for shorter shaping times. The Boltzmann constant is denoted as k and R_s describes the series resistance of the detector.

Since electrons continuously deposit energy when they travel through matter effects close to the surface can worsen the overall energy resolution. For silicon drift detectors a lower or non-sensitive volume is always present at their surface, that does not collect all the deposit energy. This effect results in a lower charge collection efficiency at the entrance window side or in the case of a completely non-sensitive area, in a dead-layer. A simulation of mono-energetic electrons at $14\,\text{keV}$ under the assumption of the dead-layer model is shown in figure 2.7. One can see that the overall shape of the spectrum changes with increasing thickness of the entrance window and the entire spectrum is also shifted to lower energies. The distortion of the detector response by the entrance window effects as well the resolution as one can see in figure 2.8. A simulation of the **F**ull **W**idth **H**alf **M**aximum (FWHM) of a mono-energetic electron peak at $20\,\text{keV}$ is
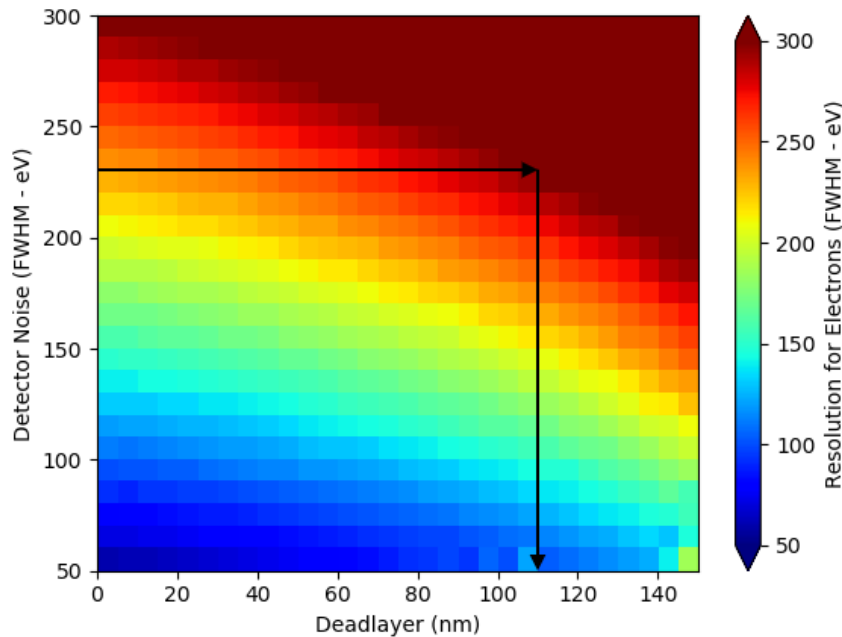
FIGURE 2.8: **Energy Resolution for electrons over the noise and dead-layer thickness**
The visualization shows the energy resolution in therms FWHM for mono-energetic electrons
at $20\,\mathrm{keV}$ for different noise width and dead-layer thickness. Values for the energy resolution
for electrons that exciede the $300\,\mathrm{eV}$ level are shown in dark red. This sets maximum thickness
for the dead-layer of $110\,\mathrm{nm}$. The simulation is performed with the simulation software KESS
[26].

shown over the given noise in the system and the thickness of an dead-layer. Given the
defined limit for the energy resolution of $300\,\mathrm{eV}$ at $20\,\mathrm{keV}$ all values that excited this
limit are shown in dark red and can show the allowd properties for the detector system.
Characterization measurements of the TRISTAN prototype detector show that an energy
resolution for photons is possible down to $142\pm3\,\mathrm{eV}$ at $6\,\mathrm{keV}$[27]. With a rough estimation
of the electronic noise and the Fano limit as shown in section A.1, one can estimate the
resolution for the noise and Fano of $235\,\mathrm{eV}$. Using this estimation for the detector noise
width in figure 2.8 one can set an upper allowed limit for the thickness of the dead-layer
of about $110\,\mathrm{nm}$.

The effects of the entrance window depend on the energy of the incoming electron and
are larger for low-energy electrons, since their mean free path is smaller and they interact
more often close to the surface. Therefore they deposit most of their energy close to the
surface of the detector. For electrons between $1\,\mathrm{keV}$ to $6\,\mathrm{keV}$ the total deposit energy
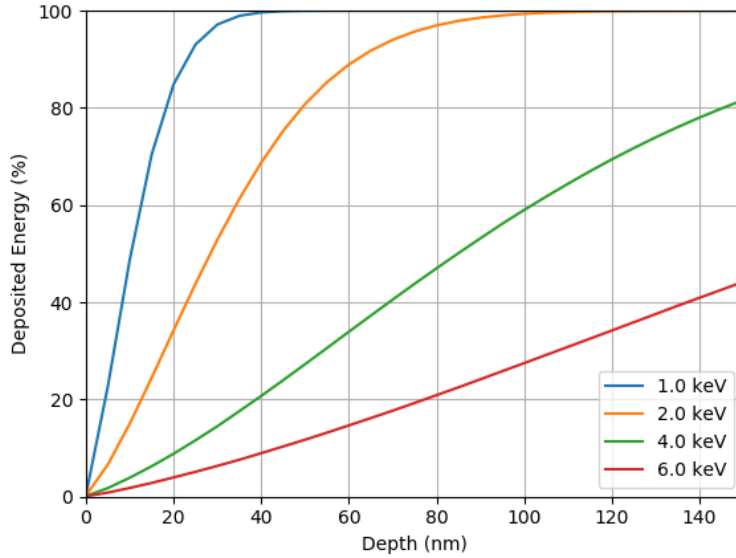over the depth is shown in figure 2.9. As an example an electron of $1\,\mathrm{keV}$ will in average

FIGURE 2.9: **Average stopping distance of electrons in silicon**
The total ratio of deposited energy inside the detector as a function of the depth in the detector is shown. The lines represent the energies between $1\,\mathrm{keV}$ to $6\,\mathrm{keV}$ and are calculated using simulations with KESS[26] for mono-energetic electrons.

deposit all its energy in the first $40\,\mathrm{nm}$. If this area would be a dead-layer the electron could not be detected and would lead to a detection threshold given by the thickness of the entrance window. This detection threshold limits on one hand the parameter space for the sterile neutrino search, but more importantly it reduces the information of back scattered electrons and charge sharing events in the detector. To guarantee the understanding of the energy spectrum to a ppm-level these low energy events have to measured as well and therefore a very thin entrance window is preferred.

In this thesis the effects created by the entrance window are investigated to understand the detector response of the TRISTAN prototype detectors. To accomplish this task four different silicon drift detectors with ultra thin entrance window technologies are investigated in this thesis. The first goal is to measure the imprint of the entrance window effects in mono-energetic electron spectra and relate it to a physical property of the detector. This will enable the comparison of the different entrance window technologies to select the most promising technology for further investigations as shown in chapter 6.5. In the next step an empirical model is designed to describe the entire energy spectrum for mono-energetic electrons and its dependency to the angle and energy of the incoming electrons as shown in chapter 7.2.

3 Silicon Drift Detectors

The TRISTAN project aims to fulfill the requirements seen in chapter 2.3 using the promising technology of **S**ilicon **D**rift **D**etectors (SDD). These detectors can handle high rates up to 100 kcps with an excellent energy resolution close to the Fano-limit. They are a special kind of semiconductor detectors, that can detect ionizing radiation like photons, electrons and other charged particles as explained in chapter 3.1. The working principle of the SDDs and the underlying technology of sideward depletion is shown in section 3.2. At the end of this chapter the partial event model for the effects at the entrance window of a SDD is introduced.

3.1 Basic Principle of Semiconductor Detectors

Semiconductor materials, whose conductivity lies between the one of metals and insulators. Since the the separation between them is fluid one of the important properties of semiconductors is the fact that their conductivity increases with temperature. Close to absolute zero the valence band is completely occupied while the conductive band is empty. Therefore no free charge carriers are available to allow conductivity. With increasing temperature the probability of electrons in the valence band to get thermally excited to the valence band increases. Therefore more free charge carriers occupies the valence band which increases the conductivity increases. The difference between semiconductors, metals and insulators in therms of their band structure can be seen in figure 3.1.

A frequently used semiconductor material for detectors is silicon, a type IV material of the periodic table. Next to its availability, the energy to produce a electron-hole pair is rather small with $w = 3.6\,\text{eV}$. This allows to create more electrons per deposited energy (e.g. incoming particle), which leads to a overall better resolution compared to other materials.

To alter the conductive behavior, it is also possible to add additional states in the band gap instead of heating the material. This decrease the energy to excite electrons form the valence band to the conductive band and creates free electrons and free holes. This can be achieved by doping the silicon with type V materials e.g. phosphorus to create
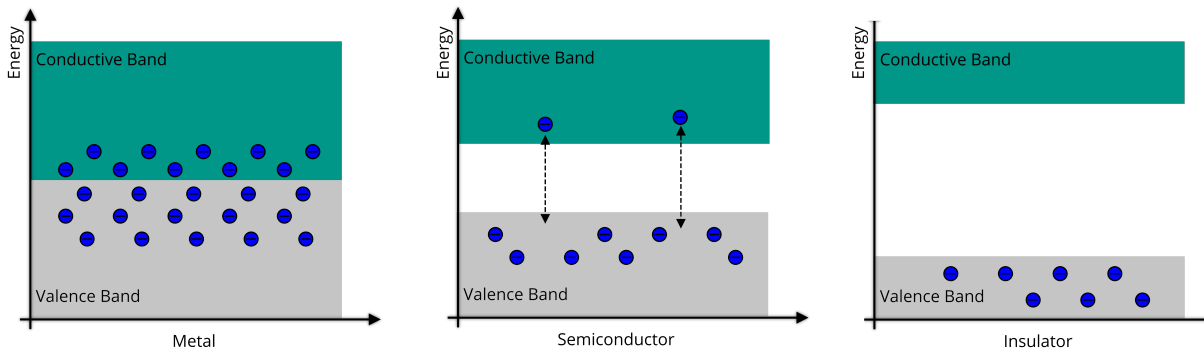
FIGURE 3.1: **Exemplary band structure for metals, semiconductors and insulators**
For metals the the valence band and the conductive band are in contact or even overlap. Electrons can move freely as charge carriers. Insulators on the other hand have a large band gap and all electrons are situated in the valence band which leads to no conductivity. Semiconductors lie in between these two extreme cases. They are neither good conductors nor insulators, however their conductivity can be increased and controlled by doping.

a n-type semiconductor or by adding material of type III e.g. boron to create a p-type semiconductor. For n-type doping this establishes an energy level close to the conductive band, that produces even at low temperatures free electrons in the conductive band. A similar behavior occurs for p-type doping to create an energy level close to the valence band, with the difference that an additional hole can be created in the valence band. Free holes increase the conductivity of a material in the same way as free electrons. A visualization of this process can be seen in figure 3.2.

Particles that penetrate material like silicon create electron-hole pairs at every interaction point. The number of these created charge carriers are many orders of magnitude smaller than the free charge carriers already existing in an intrinsic silicon substrate at room temperature. The signal can not be distinguished from the thermal charge carriers, whose number therefore has to be reduced to detect the signal charge carriers in between[28].

This can be achieved by cooling the substrate to very low temperatures close to absolute zero. Nevertheless, the easier solution is to deplete the detector volume, using the principle of a reversed-bias pn-junction to reduce the number of free charge carriers.

A pn-junction is created by connecting an n-doped and a p-doped material of the same concentration with each other. While the n-type material has an overflow of electrons, a p-type has an overflow of holes. These surplus charge carriers move to opposite regions and recombine leaving behind the fixed charged dopant atoms. These oppositely charged atoms create an electric field against the movement of the free charge carriers preventing further diffusion. The resulting 'built-in' voltage is called diffusion voltage $U_{\mathrm{diffusion}}$ and
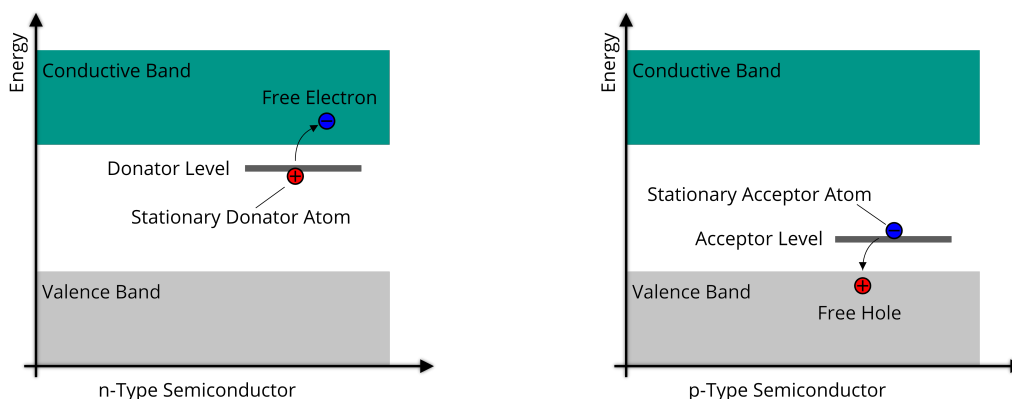
FIGURE 3.2: **Illustration of band structure for doped semiconductors**
On the left-hand side the band structure of an n-doped semiconductor is shown. The additional level in the forbidden gap is created by the placed impurity of type V of the periodic table. At room temperature the surplus electron can easily be excited to the conductive band. For the p-doped semiconductor on the right-hand side one electron is missing. This allows an electron to excite to the added acceptor level of the doped atom and leaves a free hole in the valence band. In both cases these free charge carriers increase the conductivity of the semiconductor.

establishes a dynamic equilibrium in the transition area without any free charge carriers, which is called depletion zone.[28]

By applying an additional external voltage U_{bias} in the same direction of the built-in voltage $U_{\mathrm{diffusion}}$, the depletion zone can be increased. The processes involved in the formation of a pn-junction are illustrated in figure 3.3. Incoming particles that interact inside the depletion zone will create a charge cloud of electron-hole pairs. The electrons drift against the electric field to the n-doped side, also called anode, where they can be read out. The holes move to the opposite side and end up at the cathode and can be detected as well. The collected charge at either side is proportional to the deposited energy of the particle. This kind of detector is called pin-diode.

3.2 Working Principle of Silicon Drift Detectors

In 1983, the sideward depletion was introduced by E. Gatti and P. Rehak to produce semiconductor detectors for ionizing particles with a low anode capacitance [29]. The resulting detector type is known as **S**ilicon **D**rift **D**etector (SDD).

To understand the working principle of SDDs and the sideward depletion, first a normal **p**ositive **i**ntrinsic **n**egative (pin)-diode is shown in the top part of figure 3.4. A pin-diode consists of differently doped electrodes on each side of the detector. The entrance side is containing a p^+-doped substrate and the bottom side is the anode with n^+-doping. With
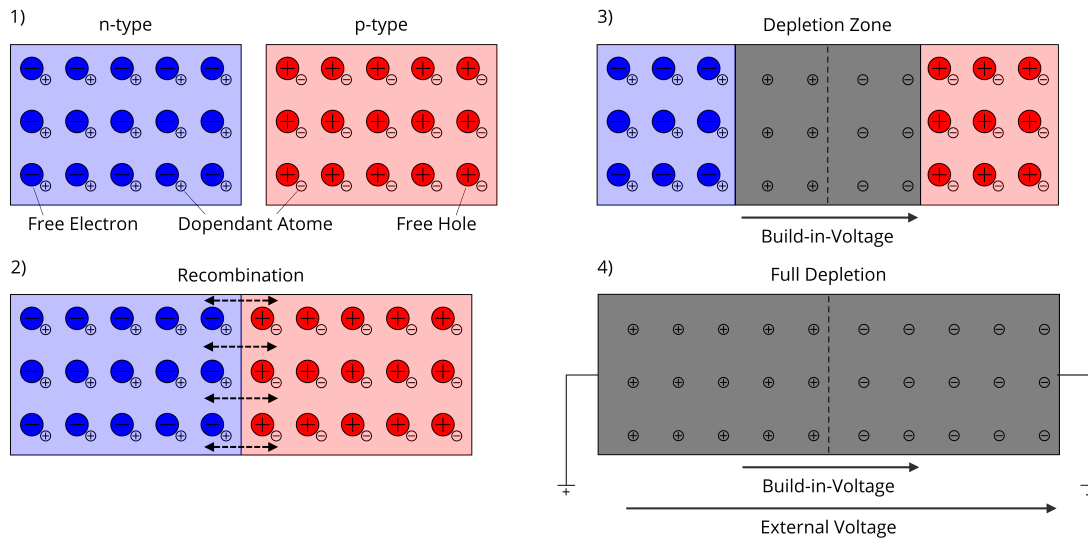
FIGURE 3.3: **Illustration of reverse-bias pn-junction**
The creation of a reversed-bias pn-junction is shown in several steps. In the first picture an n-doped semiconductor is shown in blue with additional free electrons and the p-doped semiconductor with additional free holes is shown in red. The corresponding remaining atoms with their charge are represented by the smaller charge symbols while the free charge carriers are described with the larger symbols. In picture 2) the recombination process is illustrated when the two doped materials are connected. The free charged particles recombine with each other and create a depleted zone (illustrated as the grey area) with no free charge particle inside. The diffusion current of the charge carriers and the build-in voltage $U_{\text{diffusion}}$ establishes an equilibrium. The depletion zone can be increased by applying an additional voltage U_{bias} as shown in the last part.

some voltage U smaller than the depletion voltage U_{dep}, the detector depletes partly as explained for the pn-junctions in chapter 3.1. The sideward depletion is possible since it is not necessary to extend the n^+ doped contact over the entire area. It can rather be placed anywhere on the undepleted area. The anode is scaled down and the additional space is filled with p^+-doped material. This leads to multiple separated space-charge regions as shown in the second part of figure 3.4. By applying a high enough voltage U_{Bias} the depleted zones will touch each other and deplete the entire detector. This double sided diode needs only a fourth of the voltage applied to the p^+- electrodes compared to pin-diode of the same size[29].

In this configuration a potential valley for electrons exist, but for regions apart from the anode, the electrons are not guided to the latter. Even though it is possible that these electrons reach the anode via thermal diffusion, the drift times for this will be too slow and it is not possible to associate the electrons to one common event. To solve this problem, an additional electric field is applied parallel to the surface. This is achieved by dividing the bottom p^+ bulk into smaller strips and applying a graded potential U_{Ring_X} to U_{Ring_1} on them. With this additional field electrons are guided to the anode from every point in the detector. A simulation of these fields can be seen in figure 3.5.

The charge collection at the anode is proportional to the measured energy and the drift times of the electrons can be used to calculate the interaction point of the incoming particle. In comparison to the classical pin-diode the anode is much smaller, which decreases the capacitance of the collecting anode to the order of $100\,\text{fF}$[29]. This value is mostly independent of the active area of the detector and therefore allows larger devices with good energy resolution.

The first SDDs were designed with multiple anodes arranged in stripes or matrix like patterns to reconstruct the particle interaction point inside the detector for high energy physics experiments. This could be achieved by measuring the drift times of the created particles to various anodes.

For the TRISTAN project one pixel is created by a radial drift field as shown in figure 3.6. One important benefit of this design, compared to the linear or matrix like devices, is that it is much easier to properly terminate the field lines. The radial symmetric potential valley guides the electrons to the point like anode which is placed in the center.
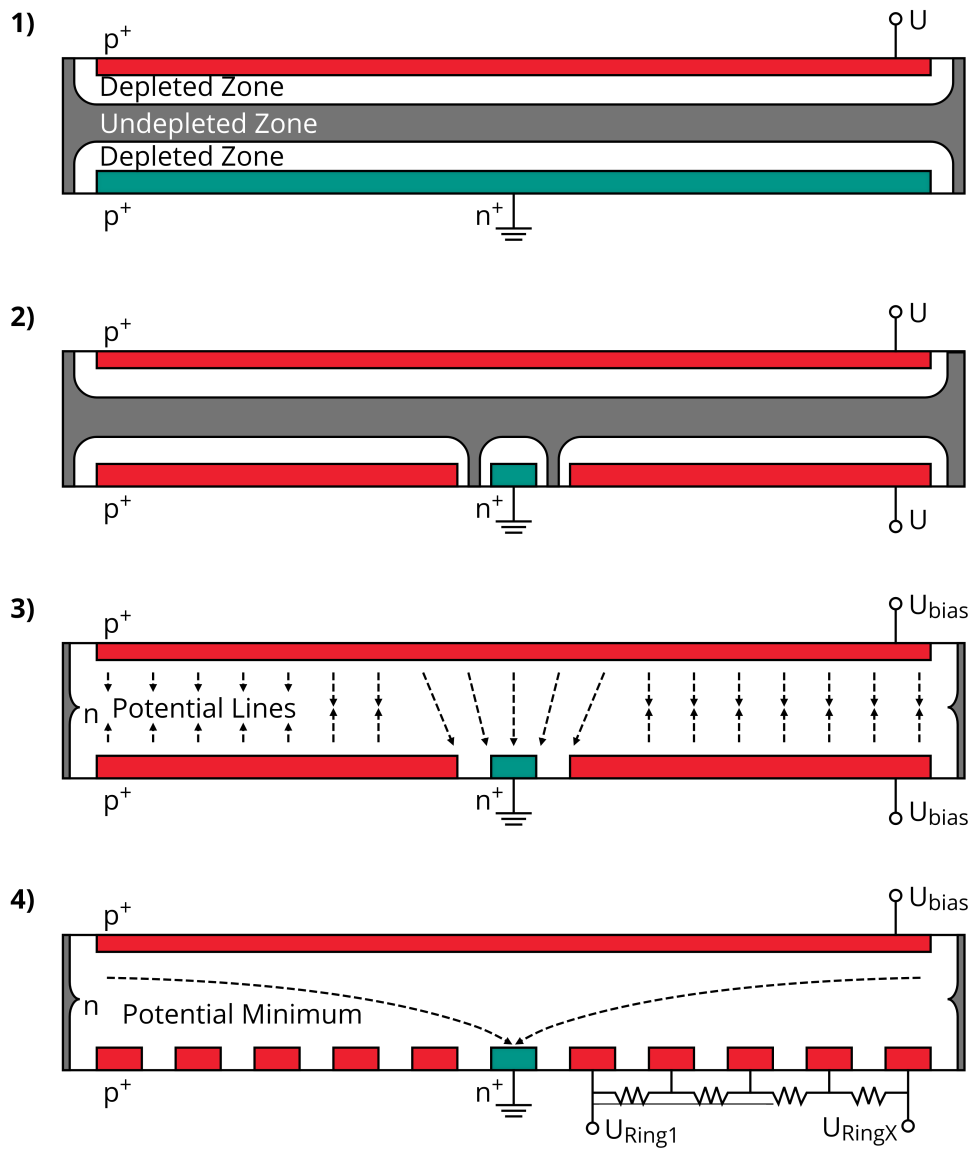
FIGURE 3.4: **Illustration of sidewards depletion**
The steps from a pn-junction or pin-detector to a SDD are shown in the parts 1) to 4). The first picture shows a pin-diode where the ohmic contacts n^+ for the anode (green) and the p^+ electrode (red) extend over the entire surface on both sides of the detector. The principle of sideward depletion shown in the second step. By covering both sides of the detector with p^+ electrodes, the n^+ anode can be designed much smaller to reach the same level of depletion. For 1) and 2) the applied bias-voltage U is chosen to be smaller than needed to deplete the entire detector. The depletied region is illustrated in white. The full depletion can be seen in the third part after applying a high enough voltage U_{bias}. In this way the applied voltage is four times lower compared to a pin-diode of same size[29]. The potential lines for electrons are shown with arrows. To force the electrons to drift towards the anode an additional electric field is applied parallel to the surface. This is achieved by separating the bottom electrode and applying the drift voltages U_{Ring_X} to U_{Ring_1} as shown in 4).
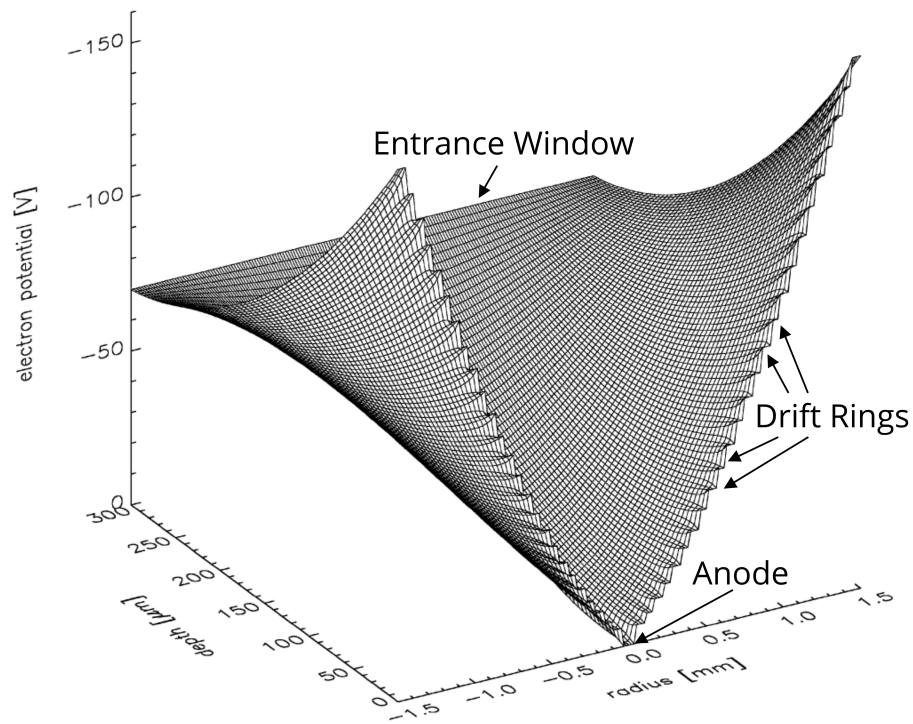
FIGURE 3.5: **Simulation of energy potentials for electrons inside a radial symetric Silicon Drift Detectors (SDD)**
The flat area in the back shows the applied voltage at the entrance window side to the p^+ electrode. On the radial axis, at a depth of zero, the set potential for the drift rings can be seen. The potential reaches its miniumum at the anode in the middle of the detector. From all points inside the detector electrons are guided to the anode. (Simulation adapted from [30])
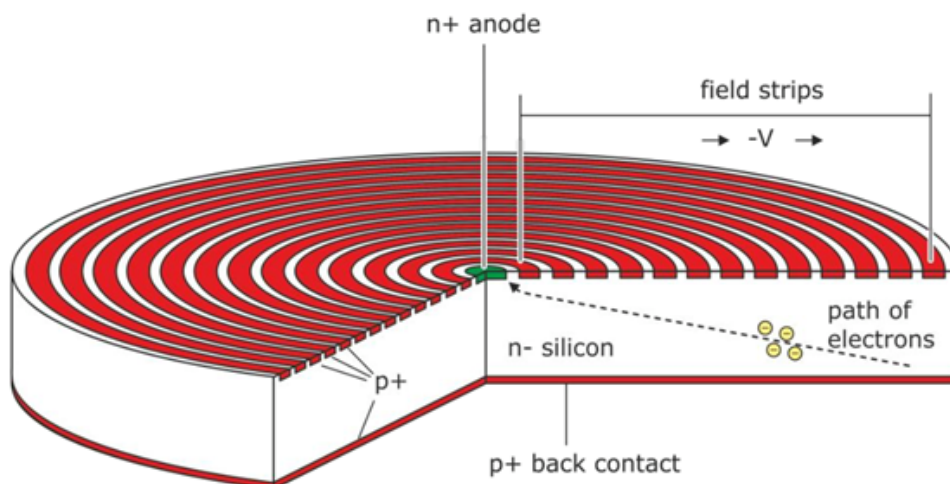

FIGURE 3.6: **Schematic diagramm of an SDD for the TRISTAN project**
The back contact on the entrance window side as well as the drift rings are doped with p^+ material and are shown in red. The n^+ anode is shown in green. (Scheme adapted from [30])

3.3 Entrance Window and Partial Event Model

When electrons pass trough matter like silicon, they interact almost continuously with it and create secondary electrons and holes. Especially the secondary electrons created close to the surface of the detector behave differently than the secondary electrons in the bulk, as shown in [31] and [32] for incoming photons.

This behavior originates from the electric potential close to the surface of the detector, which can be flat or even guiding the electrons away from the anode, due to the depth of the p^+ doping. The simplest model to describe such an effect is a completely non-sensitive layer at the top of the detector, which is called dead-layer. It corresponds to an area where all created secondary electrons are guided to the interface between silicon and silicon oxide, where they recombine with e.g defects and can not be detected any more. This silicon oxide layer is always present, since it builds itself if silicon is in contact with air. By artificially adding a silicon oxide layer it can be created as homogeneously as possible and it also protects the detector from further oxidation. On top of this the silicon oxide layer is required to produce the ultra thin entrance windows as schown in section 4.1.1.

A more sophisticated description of the entrance window effects is given by the partial event model([31], [32]). It takes into account that the charge cloud of secondary electrons can split and only a part of it is lost while the other part gets detected. To encounter this effect the charge collection efficiency of the detector, close to the entrance window, is modified. It is defined as the ratio of collected electrons at the anode compared to the created electrons at a distance z from the entrance window side ($z = 0$). An analytic formula is developed in [32] and is shown in equation (3.1).

$$CCE(z) = \begin{cases} 0 & : z < d \\ S + B \left(\frac{z-d}{l}\right)^c & : d \leq z \leq l + d \\ 1 - Ae^{-\frac{z-d-l}{\tau}} & : l + d \leq z \leq D \end{cases} \tag{3.1}$$

with:

$$A = (1 - S)\left(\frac{\tau c}{l + \tau c}\right) \tag{3.2}$$

$$B = (1 - S)\left(1 - \frac{\tau c}{l + \tau c}\right) \tag{3.3}$$

The detector thickness is denoted as D and z describes the depth into the detector, starting at the entrance window side. The parameter S describes the minimal ratio of
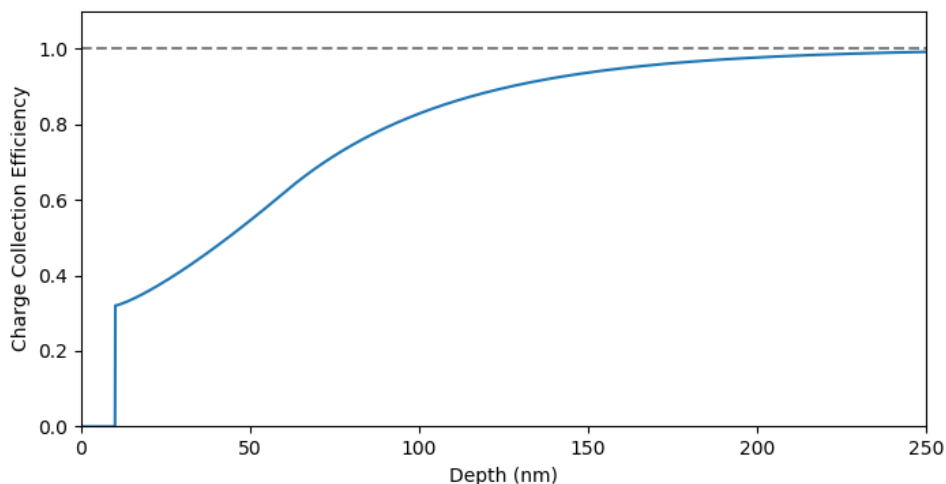
FIGURE 3.7: **Illustration of the charge collection efficiency function**
The displayed charge collection efficiency function is motivated from the partial event model. To draw the collection probability for a SDD the measured values by [33] are used. Silicon oxide thickness $d = 10\,\mathrm{nm}$, minimal collection efficiency $S = 0.32$. Transition parameter $l = 50\,\mathrm{nm}$ and $\tau = 50\,\mathrm{nm}$. Curvature parameter $c = 1.26$.

electrons detected and can take values between 0 and 1. The depth for the influence of the entrance window effects is described by the transition parameter l, which typically lies for SDDs in the range of $50 - 100\,\mathrm{nm}$ and the parameter τ with a typical value of about $100\,\mathrm{nm}$. With the parameter c the curvature in this transition area is adjusted, which can take values between 1 and 2. The thickness of a completely non-sensitive layer on top of the detector (e.g. silicon oxide) is given by d. For the TRISTAN prototypes this oxide layer is about $d = 8 - 10\,\mathrm{nm}$ thick. A representation of a charge collection efficiency with typical values can be seen in figure 3.7.

4 TRISTAN Prototype Detector Setup

In this chapter an overview of the experimental setup is given. The first part describes the detector system with the TRISTAN prototype detectors and the readout system Dante DPP [34]. To generate mono-energetic electrons between $0.3\,\mathrm{keV}$ to $30\,\mathrm{keV}$ the **S**canning **E**lectron **M**icroscope (SEM) at the HLL is used and is described in section 4.2. An optimization to reduce the trigger rate on the noise and to minimize the resolution is shown in section 4.3. To compare the measurements of the electron and photons response, each detector is calibrated with photons from an Am^{241} source. The most intense lines of this source are around $14\,\mathrm{keV}$ an $18\,\mathrm{keV}$. Therefore most of the measurements performed with electrons are chosen close to these values as well to be close to the calibration lines with photons.

4.1 Detector System with the TRISTAN Prototype SDDs

To perform first tests with silicon drift detectors for the application in the TRISTAN project, several prototype detectors have been produced. The key features of these prototypes are shown in the following section, as well as the setup of the readout electronics.

4.1.1 TRISTAN Prototype Detectors

The investigated SDD chips of the TRISTAN prototype detectors are made of a $450\,\mu\mathrm{m}$ thick silicon wafer and consist of seven hexagonal shaped pixels with a diameter of $2\,\mathrm{mm}$. The hexagonal shape of the pixels enables their arrangement in an array like fashion, without any gaps between the pixels, while still having the benefits of a circular SDD. The arrangement of the pixels can be seen from the electronics side of detector board in figure 4.1. The nomenclature for them is chosen as the cardinal points and is represented with two letters, defining the **C**entral pixel as **CC** and the upper pixel as **NN** for **N**orth. The combination of **N**orth and **S**outh with **W**est and **E**ast results in the remaining names **NW**, **SW**, **SS**, **SE**, **NE** for the pixels.
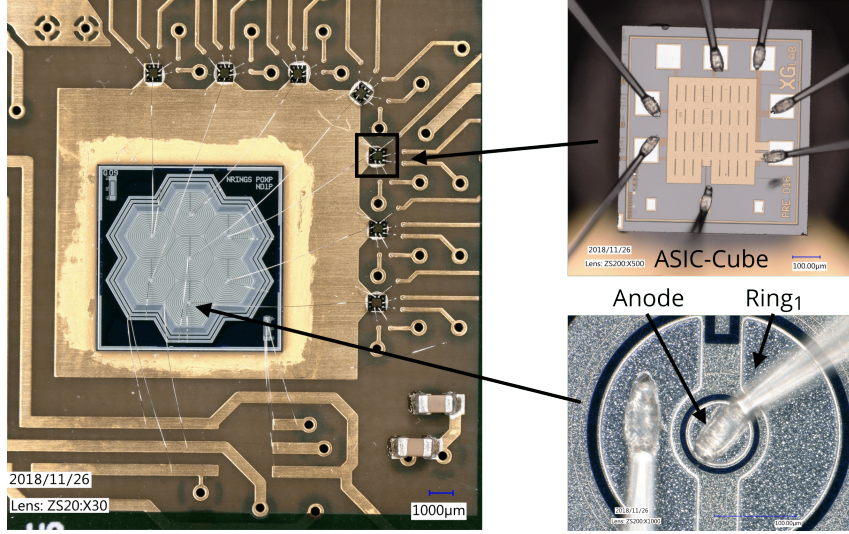
FIGURE 4.1: **Picture of the electronic side of the SDD**
On the left-hand side a mounted SDD chip is shown with all bonds and installed ASICs seen from the top side. A zoom on an ASIC-Cube [34] and on to the Anode can be seen on the right-hand side. The pictures were taken with an optical microscope.

To fully deplete the detector, the p^+-doped area on the entrance window side is set by the back contact voltage to $U_{\mathrm{Back}_C} = U_{\mathrm{Bias}} = -90\,\mathrm{V}$. To keep all electrons created inside the sensitive area, an additional p^+-guard-ring the detector. It is called back frame and is set to a slightly higher voltage of $U_{\mathrm{Back}_F} = -100\,\mathrm{V}$ to prevent that electrons are created close to the edge of the detector from leaving. The two contact points on the back side of the detector can be seen in figure 4.2.

The electric field parallel to the surface is created by twelve drift rings with a gradient between the outer ring at $U_{\mathrm{Ring}_X} = -110\,\mathrm{V}$ and the inner ring at $U_{\mathrm{Ring}_1} = -20\,\mathrm{V}$. With this field all electrons created in the sensitive area are guided towards the anode located in the center as seen in figure 4.1. It has a diameter of $90\,\mu\mathrm{m}$ leading to a capacitance of $110\,\mathrm{fF}$. The anode is connected with a $18\,\mu\mathrm{m}$ thick bond to the first amplification stage, which allows the transport of the signal without further increasing the capacitance. The first amplification is handled by the low noise preamplifier ASIC-CUBE [35]. The position of the ASIC-Cubes around the wafer and the corresponding bonds can be seen in 4.1.

The amplified signal is then routed through the detector-PCB to the output pins. It also handels the routing of the rewired power supplies for the ASIC-Cubes and the detector itself. The detector board can be seen in figure 4.3.

For the investigation of the entrance window different detectors have been produced. To separate them from each other a naming scheme has been applied to the detectors to identified them. The general naming scheme starts with two letters describing the
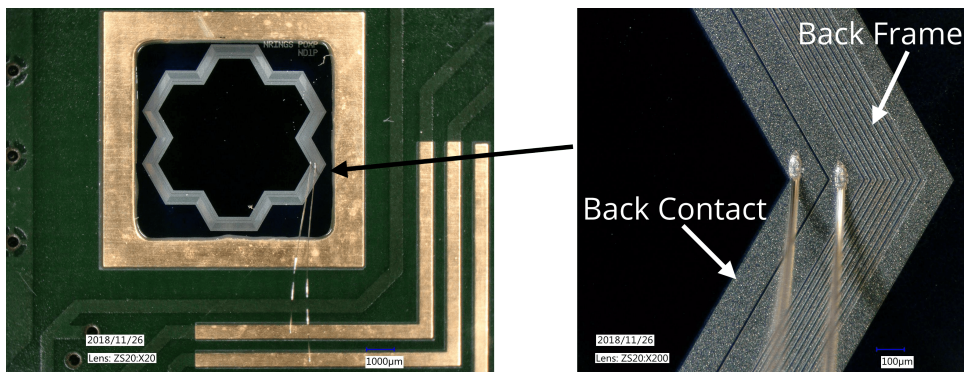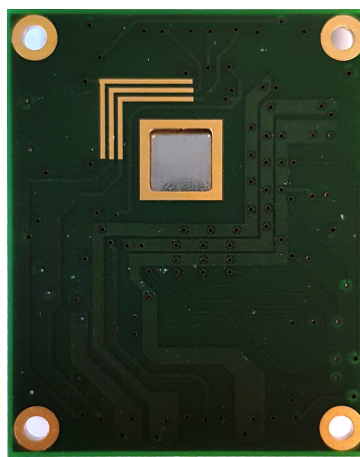
FIGURE 4.2: **Picture of the entrance side of the SDD**
On the left-hand side the entrance window side of the detector is seen, while being mounted onto the PCB. The required voltage to deplete the detector and to keep the electrons inside the detector volume is provided via the two bonds for the back contact and the back frame. A zoom on the bonding connection can be seen on the right-hand side. The pictures were taken with an optical microscope.
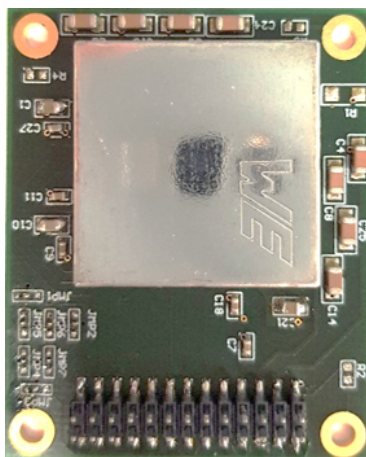
Detector board top side   Detector board entrance window side

FIGURE 4.3: **Detector board overview**
The detector board from the top and bottom is shown in this figure. As seen on the bottom side of the detector no SDD wafer is installed.

TABLE 4.1: **Internal naming scheme for** $2\,\mathrm{mm}$ **prototype detectors**
The naming scheme is chosen to directly represent the different entrance window technologies used to produce the detector.

Abbreviation	Description
S0 - #	**S**tandard radiation
SC - #	**S**tandard radiation with **C**ounter implantation
R0 - #	entrance window with reduced **D**ose
RC - #	entrance window with reduced **D**ose and **C**ounter implantation

entrance window doping profile, as shown in table 4.1, followed by a number.

The doping profile for the standard entrance window has been used in other experiments, too [32], and is highly optimized for the detection of photons. The other versions of the doping profile try to improve this ultra thin entrance window even more. For the entrance window R0 the dose of implants is reduced in the processing which results in an overall reduction of p^+-doping and the depth it enters into the material, as shown in figure 4.4. In theory, this should shift the maximum of the electric field closer to the surface, but it comes with the risk that the detector will not be completely depleted if the concentration of p^+-dopendants can not compensate the n-doping. Another way to bring the maximum of the electric field closer to the surface is achieved by counter implanting with n^+-dopendants behind the p^+-doping. Like the reduced dose technique this entrance window comes with the risk that if the concentrations are not well balanced anymore, the detector does not deplete. The combination of these two techniques whilst producing the RC-detectors, this problem lead to the large inconsistencies up to the malfunction of these detectors. Therefore, in the further work only the working technologies S0, R0 and SC are investigated.
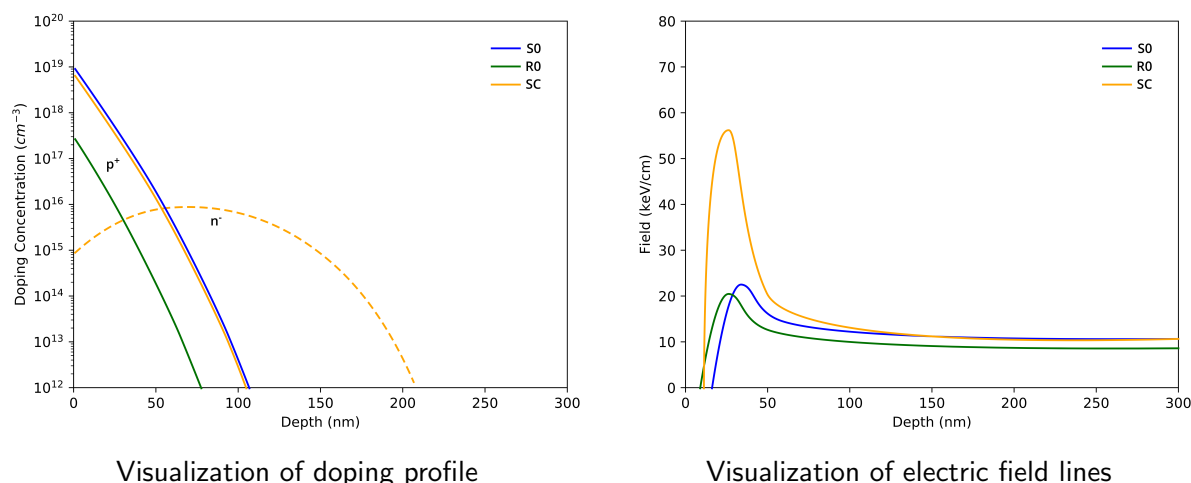
Visualization of doping profile   Visualization of electric field lines

FIGURE 4.4: **Vizualization of doping profiles and electric fields**
On the left-hand side a visualization of the doping profile for the different entrance window
technologies is shown. The standard implantation S0 and the reduced dose R0 are produced
with p^+-doping. In contrast to this, the SC doping profile is produced with an additional
counter implantation of n^+-impurities. An estimation of the electric filed lines is shown on the
right-hand side. The plots are based on [36], but do not represent an actual measurement.

4.1.2 Readout-Chain

The bias board filters and provides the routing for all the needed voltage supplies for the
CUBE-ASIC and the SDD. In addition to this it sends a common reset signal to all the
ASIC-CUBEs on the board. The signal arriving from the detector board gets amplified
a second time to drive a coaxial cable to the **D**ata **A**cquisition **S**ystem (DAQ). The bias
board can be seen in figure 4.5.

An exemplary waveform can be seen between two resets of the ASIC-CUBEs as shown
in figure 4.6. The continuous increase of the waveform is created by the leakage current
of the detector. A particle interacting with the detector will create many electrons (and
holes) in a short time, which charges the input of the ASIC-CUBE and therefore increases
the voltage at its output. This signal manifests itself in the waveform as a sharp step. To
prevent the ASIC-CUBE from saturation a synchronous reset signal is sent to all ASIC-
CUBEs at a set threshold to discharge them. This leads to the steep decrease in the
waveform.

To extract the energy information of each event, the waveform is digitized with the
DANTE DPP (**D**igital **P**ules **P**rocessor) and analyzed with two trapezoidal filters. It
has a sampling rate of 125 MHz with a 16-bit **A**nalog to **D**igital **C**onverter (ADC). To
trigger on all possible events, which could be above the threshold, a fast trapezoidal filter

Bias board   DANTE DPP

FIGURE 4.5: **Read-out chain hardware**
On the left-hand side the bias board is shown. The power supply for the detector and the on board electronics can be connected with a D-Sub 9 connector at the top. Detector and bias board are connected with 25 pin cable on the left. The seven coaxial cables for the signals to the Dante DPP leave on the right. The picture on the right hand side shows the digital pulse processor DANTE DPP by XGLab [34] for eight channels.

is applied to the digitized waveform in the first step. The peaking time and flat top time of this fast filter can be set to values between 8 and 248 ns which allow a fast selection of possible events. This fast filter marks possible events that are above the set threshold. All events that are preselected by the fast filter are then analyzed with a longer and more accurate energy trapezoidal filter. The energy filter peaking time can be set up to 16 μs, while the optimum value for the TRISTAN prototype detectors is around 800 ns with respect to the energy resolution [27]. Events that happen closer together then the time window of the energy filter lead to pileup. Since the fast filter has a much shorter time windows it can detect such events and allows the option to reject these events. For the measurements this feature is used.

The combination of the fast filter and the energy filter allows a precise measurement of the deposited energy in the detector at very high rates and is performed by the **F**ield **P**rogrammable **G**ate **A**rrays (FPGA) of the Dante DPP. The measured events can then be saved in a histogram or as a list of the time stamp and energy for every occurred event. A sketch of the setup with the entire readout chain can be seen in figure 4.7.
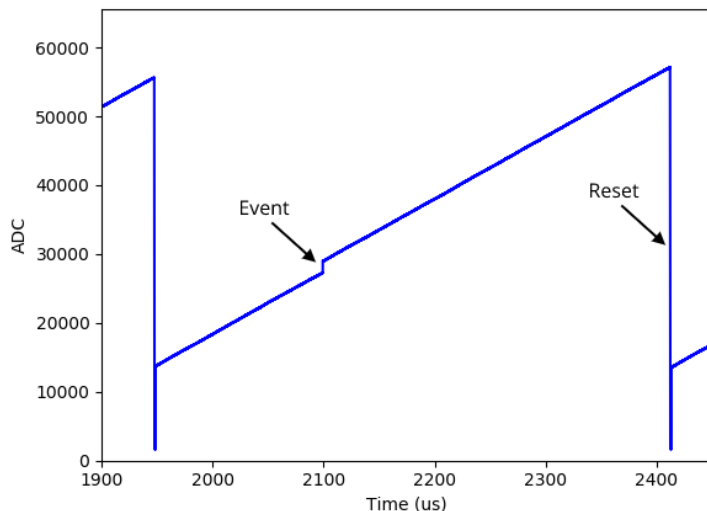
FIGURE 4.6: **Exemplary Waveform of Detector**
Example of a digitized signal waveform taken with the Dante DPP system for a TRISTAN
Prototype-0 detector at room temperature. A signal leads to a step in the waveform while
the leakage current creates the continuously raising ramp. With the common reset signal all
charges collected at the input of the ASIC-Cube are discharged through the ground. This
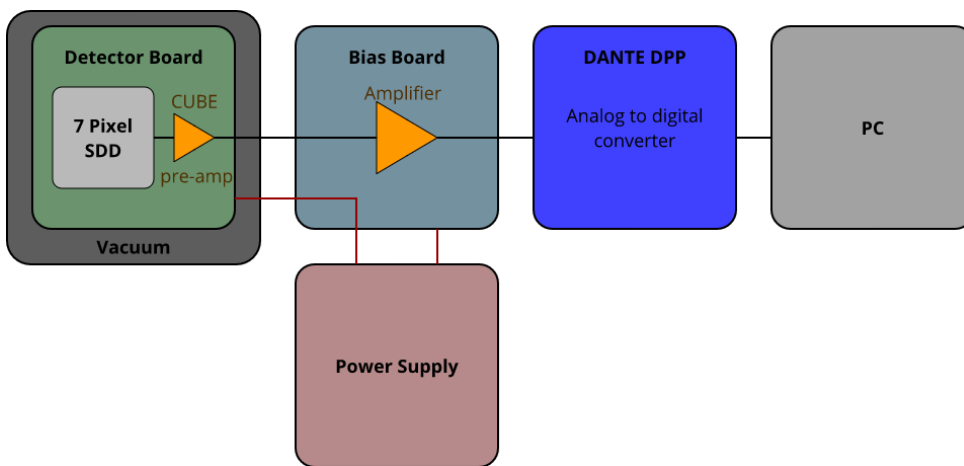creates the steep drop of the waveform.

FIGURE 4.7: **Overview of the readout chain and the experimental setup**
The signal registered at the detector gets amplified at the pre-amplifier in the CUBE-ASIC
on the Detector-PCB and is further routed to the bias board with a flat cable. At the bias
board the signal gets amplified a second time and is connected with coaxial cables to the
DANTE DPP where it is digitized. The required power to deplete the detector and to drive
the electronics on the detector board are generated with a power supply and then properly
divided and filtered by the bias board.

4.2 Scanning Electron Microscope as Source for Mono-Energetic Electrons

The required mono-energetic electrons for the investigations of the TRISTAN prototype detectors are provided by a **S**canning **E**lectron **M**icroscope (SEM) present at the Max-Plank **H**alb**l**eiter **L**abor Munich (HLL). The used SEM of type JSM-IT300[37] is shown in figure 4.8.

At the top of the SEM a tungsten spiral is heated up to 2000 °C to thermally emit electrons which are then accelerated with an electric field to energies between 0.3 keV and 30 keV. The calibration accuracy of the electron gun is about 2% of the set energy while its energy width is smaller than one electron volt [38]. The electron beam itself has a size of approximately 10 nm [37] in diameter. To scan a probe (e.g detector) the focused beam is directed by magnets at the end of the electron gun moving from left to the right. This leads to a periodic illumination of the single pixels as seen in figure 4.9. The overall illumination of the detector can be adjusted by reducing the current that heats the tungsten spiral. This results in a reduction of the electron beam current to not saturate the detector. It was adjusted to have only a small amount of pileup and created count rates up to 15 kcps when the pixel is hit by the moving beam. Since the electron beam is bent to hit all the pixels, the variation of the incident angle can be calculated from the distance to the magnet. For the central pixel the difference form a perpendicular incident angle is below 2° and for the outer pixels below 5°.

The detector is placed inside the vacuum chamber below the electron gun and is centered as shown in figure 4.10. Between the detector and the electron gun a holding structure made for different insertions is mounted. If nothing is installed the electron beam can directly shine on the detector, otherwise e.g a calibration source with mono-energetic photons can be placed inside the holder to illuminate the detector. The detector itself is mounted on a 5 axis movable stage that allows a precise alignment of the detector and the possibility to change the incident angle of the incoming electrons by tilting the detector. For visual checks an infra-red camera is installed at one side of the vacuum camber as shown in figure 4.10.

An exemplary spectrum of the mono-energetic electrons produced by the SEM for 14 keV is shown in figure 4.11 in the units of the readout system. One can see the main peak of the electron spectrum at around 5500 ADC which corresponds to 14 keV. The silicon escape peak can be seen as well, with an expected shift of 1.74 keV from the main peak. The energy shift of the peak corresponds to the silicon K_α line. If a particle deposits energy inside the detector, it can knock-out an electron form the K-shell of silicon. When the hole

FIGURE 4.8: **Picture of the JSM-IT300 InTouchScope Scanning Electron Microscope**
The electron gun of the SEM is positioned on top of the vacuum chamber and can produce
electrons between $0.3\,\mathrm{keV}$ to $30\,\mathrm{keV}$.[37]
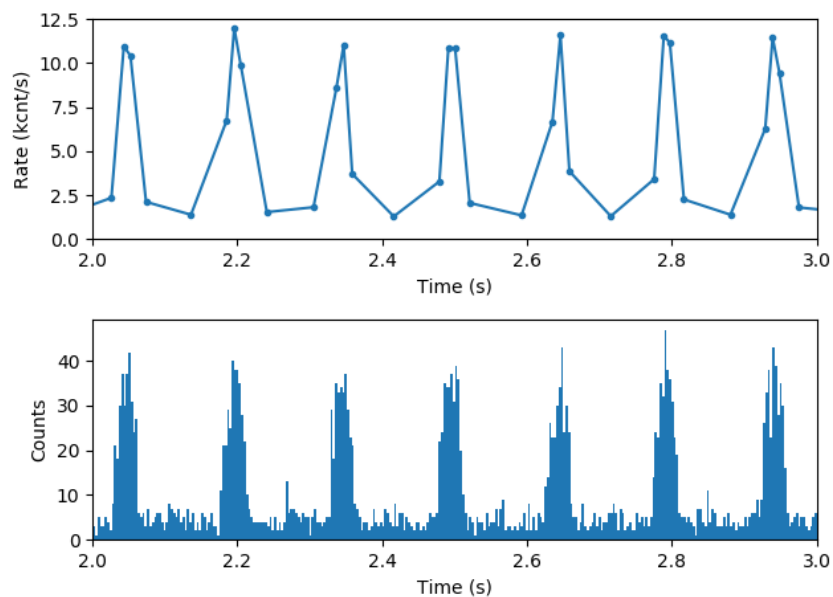

FIGURE 4.9: **Electron count rate over time**
The top plot shows the variation of the electron rate on the central pixel during the measure-
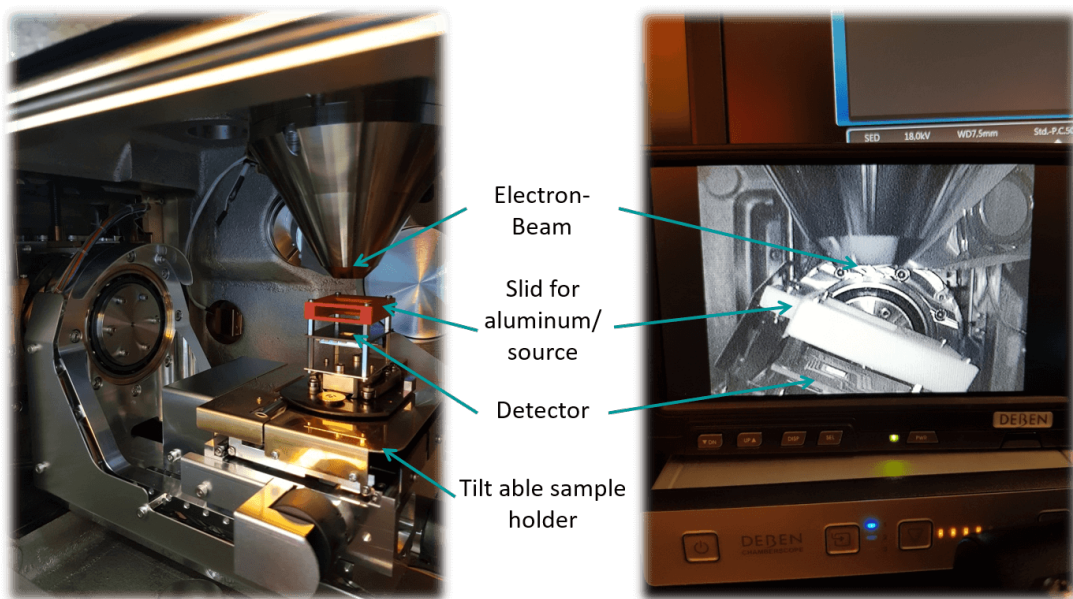ment of $14\,\mathrm{keV}$ electrons. The bottom plot shows the counts in the central pixel with a bin
size of $30\,\mathrm{ns}$.

FIGURE 4.10: **Experimental setup inside SEM**
On the left-hand side the setup inside the vacuum chamber of the SEM is shown. The detector is facing upwards and is centered below the electron gun of the SEM. In between them, the slid holder for e.g. calibration sources is mounted without any slid. On the right-hand side a view of the vacuum chamber with the build in infra-red camera is shown for a tilted detector. In the given picture the alignment of the electron beam was purposely chosen next to the detector.
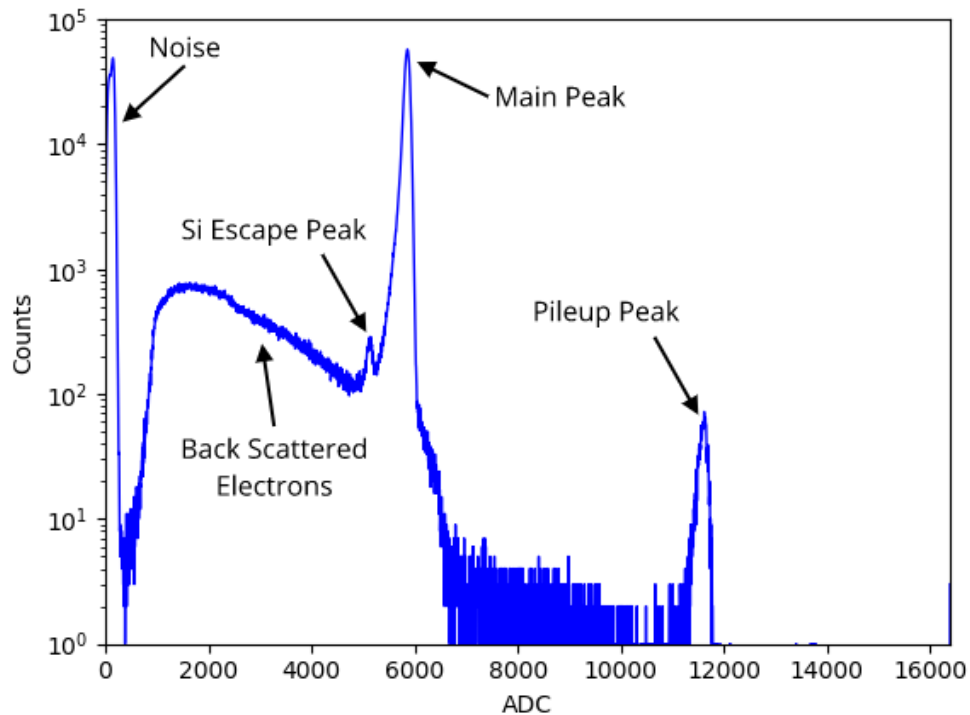
FIGURE 4.11: **Exemplary electron spectrum**
The energy spectrum is taken with detector S0-2 for $14\,\mathrm{keV}$ and shows the entire range of ADC. The gain of 4.4 in the DANTE DPP is chosen to fit the main peak of electrons up to $30\,\mathrm{keV}$ nicely on the entire ADC range. The entire ADC range corresponds then to approximately $40\,\mathrm{keV}$.

in the K-shell is filled by an electron of the M-shell, a photon with an energy of $1.74\,\mathrm{keV}$ is created. With a given probability this photon can leave the detector without getting detected shifting the entire spectrum by its energy. Since the electrons scatter inside matter (e.g. silicon) they can be back scattered and leave the detector after depositing only a fraction of their energy. This area extends from the main peak down to the threshold which is at approximately $1000\,\mathrm{ADC}$ ($\approx 2\,\mathrm{keV}$). The noise of the system can be seen around the origin. This is possible as the threshold for the measurements is given by the fast filter, which can unintentionally trigger on noise due to its short peaking time. The falsely marked events are then evaluated with the energy filter which is more accurate but has no set trigger, determining their energy to be around zero.

At around $11000\,\mathrm{ADC}$ the pileup peak of the main peak can be seen. It corresponds to the doubled energy of the main peak, in this case to $28\,\mathrm{keV}$.

4.3 Optimization of the DAQ-Settings

To perform measurements at the best possible settings for the energy resolution of electrons the DAQ-settings are optimized. In the first measurements inside the SEM a much higher noise level compared to the measurements performed to characterize the detectors with photons[27] is found. Looking at the waveform one can see a periodic noise signal of about 500 kHz probably producing this interference. The periodic ripples are shown in figure 4.12 and can explain the higher noise level. To perform further measurements at an
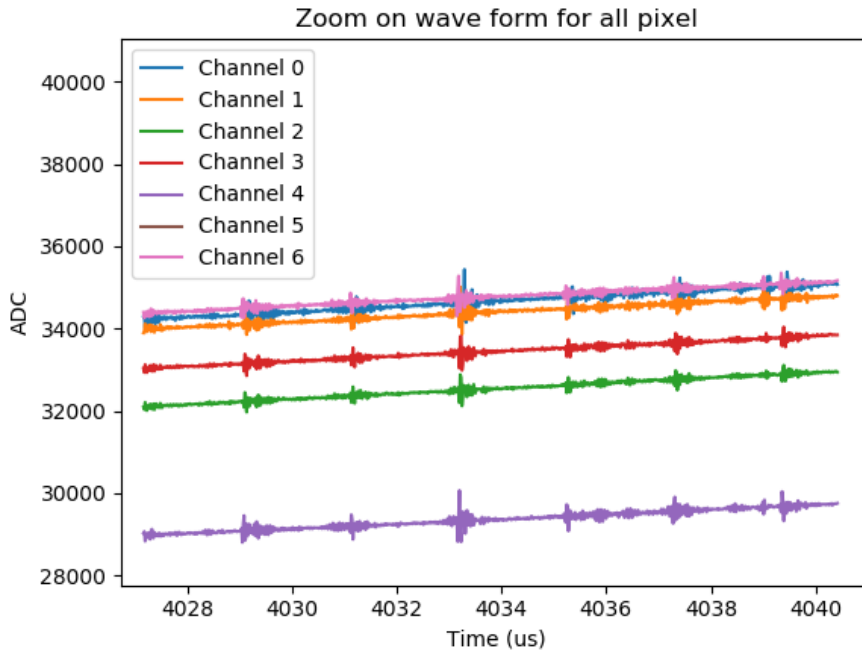
FIGURE 4.12: **Waveform Noise**
Waveform taken in the SEM for all pixel. A periodic noise with a frequency $f_{\text{Noise}} \approx 500\,\text{kHz}$ can be seen over all pixel simultaneously. The origin for these ripples is still unclear and also could not be reduced. An optimization of the fast filter is necessary to not falsely interpret these ripples as signals from the detector.

acceptable noise trigger rate blow 2 kcps the fast filter settings are optimized. To measure the trigger rate of the noise the detector is installed inside the vacuum chamber without any source. The rate is calculated by integration over all events and normalizing it to counts per second. In the first step the fast filter peaking time is varied as shown in figure 4.13 for back ground measurements of 30 s per data point. For higher fast filter peaking times the trigger rate onto the noise is strongly reduced until the settings 10 and 12 (80 ns and 96 ns) where no further improvement is seen. For the further course of this thesis the fast filter peaking time of 10 (80 ns) is used. The same procedure is repeated for the fast
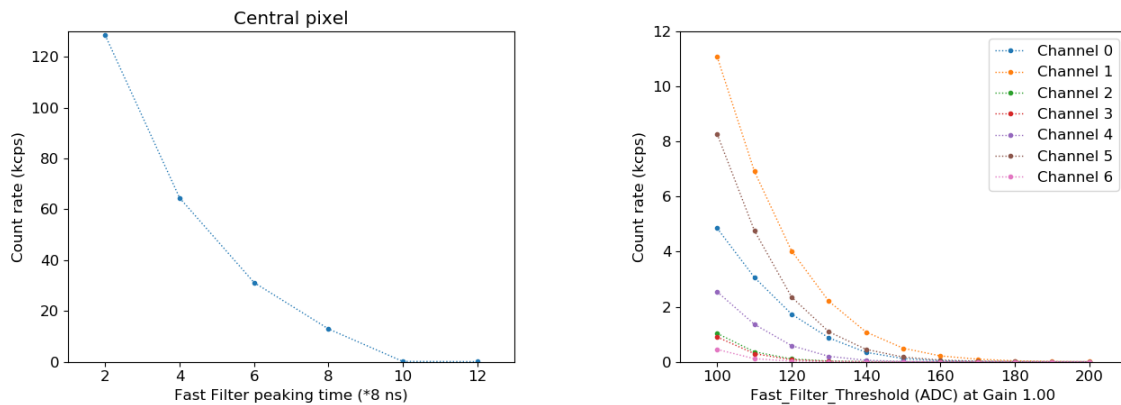
FIGURE 4.13: **Threshold tests measurements**
On the left-hand side the count rate of central pixel over the fast filter peaking time with fixed threshold of 150 ADC is shown. On the right-hand side the count rate of all pixel over the fast filter threshold with a fast filter peaking time of 10 ($80\,\text{ns}$) and fast filter flat top of 2 ($16\,\text{ns}$) is illustrated. The measurements are performed to reduce the false trigger on noise the periodic noise signal by adjusting the fast filter settings. They are taken without any source at a DAQ Gain of 1. Acceptable noise rate found for all pixels at a threshold of 140 ADCs, with a fast filter peaking time of 10 ($80\,\text{ns}$) and fast filter flat top of 2 ($16\,\text{ns}$)

filter flat top time but no noticeable improvement is found. Therefore the standard value of 2 ($16\,\text{ns}$) is used. The last setting that effects the trigger rate onto the noise is the overall threshold of the fast filter. The measured rate over the threshold settings given in ADC can be seen in figure 4.13. As expected the rate decreases with higher threshold settings. The targeted maximal rate of $2\,\text{kcps}$ is reached for $140\,\text{ADC}$ for all pixels. This value corresponds to approximately $1.6\,\text{keV}$ and is used for most of the measurements. It is noticeable that the level of noise differs largely between the pixels. The origin of the difference could not be identified.

In the next step the overall resolution is optimized for electrons. Therefore, the detector is illuminated with $14\,\text{keV}$ electrons. The resolution is estimated with the FWHM of the main peak of the measured spectra. In figure 4.14 the variation of the energy resolution depending on the peaking time can be seen. The picture represents a noise curve for the detector with a minimal resolution for 25 ($800\,\text{ns}$). This value is in agreement with other measurements performed in the past. The same test is performed for the energy filter flat top, even though no improvement could be found. Therefore, the standard value of 4 ($128\,\text{ns}$) is used.
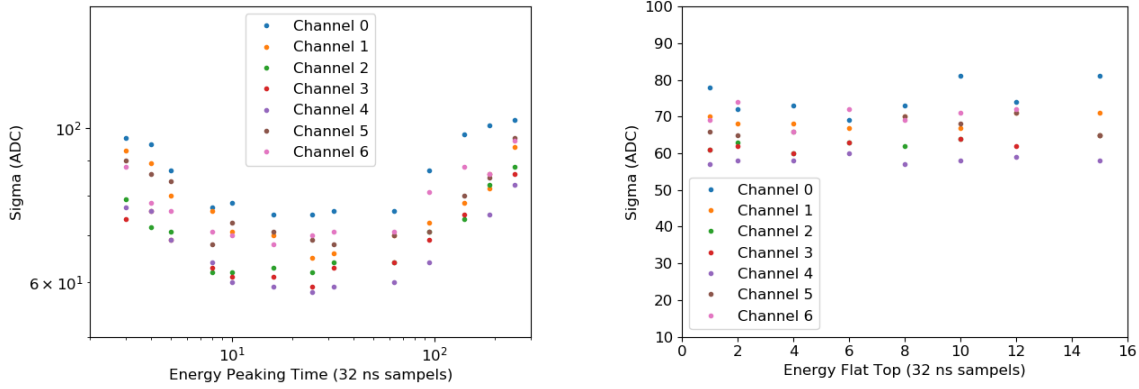
FIGURE 4.14: **Energy filter setting measurements**
On the left-hand side the noise curve for energy filter peaking time is given. On the right-hand side the energy resolution over energy filter flat top is shown. For every data point a measurement with $14\,\text{keV}$ electrons over $30\,\text{s}$ is performed. Optimum found for a energy peaking time of 25 ($800\,\text{ns}$). No optimum is given for energy flat top, therefore the standard value of 4 ($128\,\text{ns}$) from other measurements is used.

4.4 Reference Calibration with Photons from an ^{241}Am-Source

All measurements performed in this thesis are calculated and evaluated in the units of ADC, nevertheless to relate the ADC values of the DANTE DPP to the deposited energy, a calibration is useful. The easiest way to calibrate the detector is to use a source with mono-energetic photon lines. In contrast to electrons, which interact continuously with matter, the interaction of photons with matter is almost point-like. Events that happen outside the area of the entrance window are not effected by it at all and deposit their entire energy in the detector. The depth of the entrance window is in the order of $100\,\text{nm}$ while the entire detector thickness is $450\,\mu\text{m}$. This makes the energy deposition outside the entrance window much more likely and the peak position of a mono-energetic photon is thus not affected by the entrance window at all. Therefore, it can be fitted with a Gaussian function. Nevertheless the effect of the entrance window can be seen in the shape of the spectrum below the peak which represents the events inside the entrance window [32] but is negligible for the peak position[32].

To calibrate the detector, measurements with an ^{241}Am-source are performed inside the vacuum chamber of the SEM, placing the source on top of the detector inside the holding structure. The photon energy lines used for the calibration can be seen in table 4.2. The L_l, L_α and XR_1 peaks of the spectrum are fitted with a Gaussian function to estimate

TABLE 4.2: **Table of Am^{2}41 photnon lines values taken from [39]**The table contains all major lines of the decay that are used for the calibration fit.

Line Name	Line Energy
L_l	11.87 keV
$L_{\alpha 1}$	13.95 keV
$L_{\beta 2}$	16.84 keV
$L_{\beta 1}$	17.75 keV
$L_{\gamma 1}$	20.78 keV
$L_{\gamma 6}$	21.49 keV
XR_1	26.34 keV

their position in ADC. For the other lines two Gaussian functions are used, since two peaks of similar intensity were overlapping. The performed fits can be seen in figure 4.15. For the conversion from ADC to energy, a linear function with one parameter for the slope and one for the y-axis offset is assumed. An exemplary calibration curve, including the error bars on the peak position can be seen in figure 4.16.

Since for the calibration of each detector the vacuum chamber has to be opened and thus the detector voltages have to be turned on and off again, the assumption has been made that the calibration does not change over time or if the detector is restarted. To confirm this assumption, five calibration measurements are performed for one detector over multiple days and multiple restarts of the detector in between. As shown in chapter A.2 this assumption holds true inside the uncertainties of the calibration curve. In the further course of the thesis each detector is calibrated once with an ^{241}Am-source to convert the ADC values to units of energy.
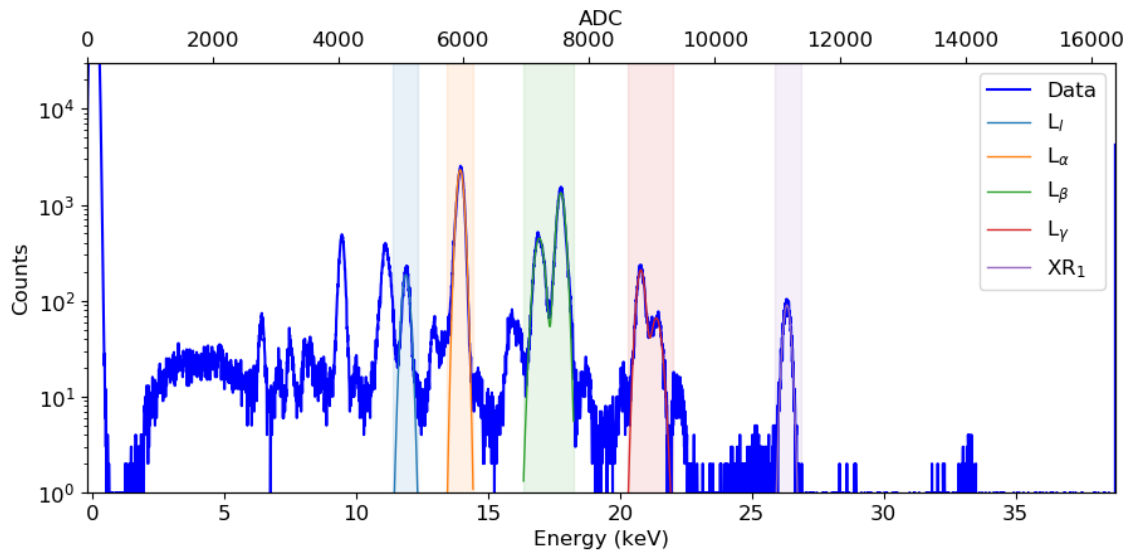
FIGURE 4.15: **Exemplary calibration spectrum of ^{241}Am**
for the calibration the most prominent lines are fitted with one or two Gaussian functions. The fit range for each peak are illustrated in different colors.
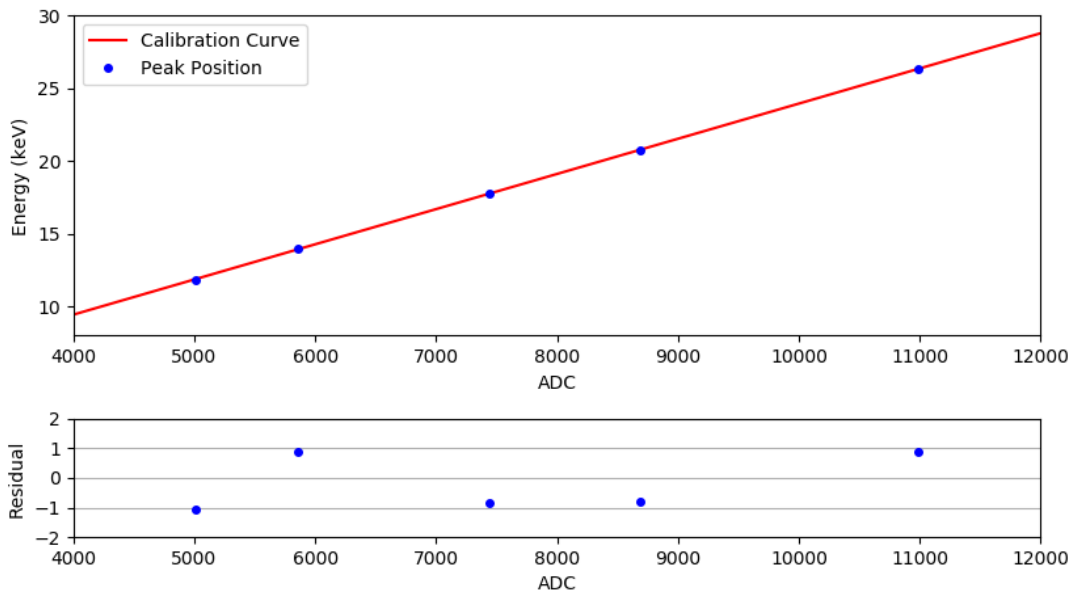

FIGURE 4.16: **Exemplary calibration curve using an ^{241}Am source**
The estimated means of the fitted lines are shown in blue while the calibration linear fit through the points is shown in red. The slope of the linear function is $(2.381 \pm 0.002)\,\frac{\text{eV}}{\text{ADC}}$ and the y-offset $(-213.5 \pm 2.0)\,\text{eV}$. The measurement was performed with detector S0-2 at a gain of 4.4 in the DANTE DPP. At the bottom the residuals are shown in units of the standard deviation.

5 Investigation of Entrance Window Effects with Bremsstrahlung

To investigate the effect of the entrance window and correlate it to a physical quantity independent of the energy of the incoming particle, a specific method is required. In this chapter the overall energy shift due to the entrance window is measured by comparing the deposit energy in the main peak to the expected energy deposited. This can be achieved by comparing the peak position of the electron spectrum to the energy of the incoming electrons. This energy shift can then be related to a thickness of the entrance window by simulations. To enable this method, the energy of the electron beam has to be known with an accuracy of a few electron volts, since the effect of the entrance window is in the order of $100\,\mathrm{eV}$. The energy calibration of the **S**canning **E**lectron **M**icroscope (SEM) is only 2% and therefore of the same order as the investigated effects, thus the electron gun has to be calibrated with a higher precision.

5.1 Calibration of the SEM with Bremsstrahlung

To measure the energy of the SEM electron beam independent of the entrance window effects, the electrons are converted into photons. This is achieved by installing a thin aluminum foil in front of the detector which stops all incoming electrons. The photons created in this process are called Bremsstrahlung. The thickness of the foil is chosen to be as thin as possible to increase the measurable rate at the detector. The thinner the foil is, the less material is in between the creation point of the photon and the detector and thus the probability that the photons are absorbed on their way decreases. Nevertheless the foil has to be thick enough to stop all incoming electrons. In aluminum this is achieved at a distance in the order of 2 to $4\,\mu\mathrm{m}$ depending on the electron energy. Since the available foils can have fluctuations in their thickness up to 15%, a $6\,\mu\mathrm{m}$ thick foil is used. The purity of the foil is chosen to be as large as possible to dampen the fluorescence lines from materials e.g. copper to reduce the additional effects on the spectrum.
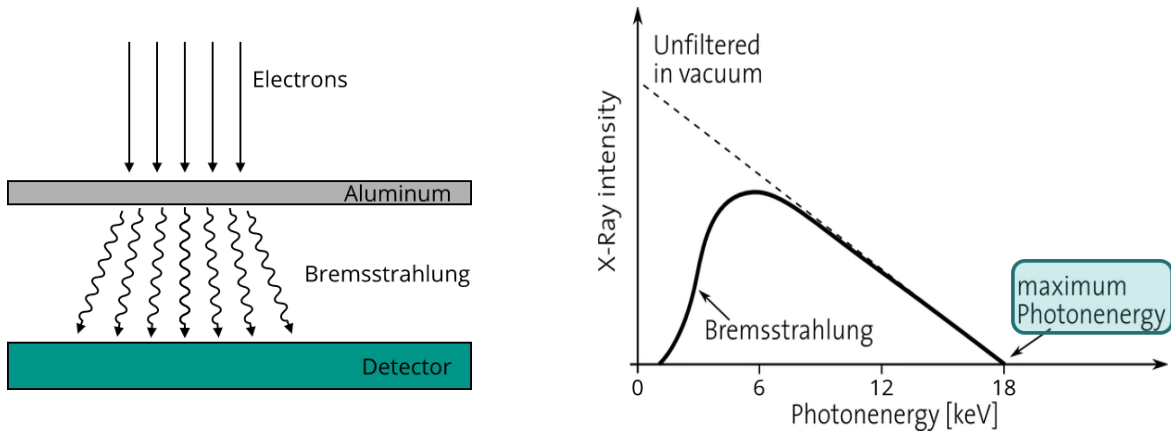
FIGURE 5.1: **Illustration of Bremsstrahlung method**
On the left-hand side the illustration of the experimental setup to produce Bremsstrahlung with electrons can be seen. The right-hand side shows the theoretical spectrum of Bremsstrahlung corresponding to electrons of $18\,\text{keV}$. The endpoint of the spectrum corresponds directly to this energy.

The energy of the electron beam corresponds to the endpoint of the Bremsstrahlung spectrum. An illustration of the method can be seen in figure 5.1.

Since the photons are (almost) not affected by the entrance window the detector can be used for the calibration of the electron gun. This enables a measurement of the energy deposit in the detector with and without influences of the entrance window. It has the benefits that the measurement of the effects of the entrance window are a relative measurement of energies and the accuracy of the absolute calibration of the detector is not important.

To measure the Bremsstrahlung spectrum, the aluminum foil is installed inside the holding structure $9\,\text{mm}$ above the detector resulting in a maximal incoming angle of 6° in the central pixel. Nevertheless the angular dependency of the photons hitting the detector is neglected in the further course of the discussion. Because the created photons are emitted in all directions and only a small fraction of them is hitting the detector, the heating current is elevated to the maximal save value. Nevertheless, to gain reasonable statistics close to the endpoint, the measurement is performed for over 12 hours. The resulting energy spectrum for detector S0-1 can be seen in figure 5.2. To estimate the endpoint of the Bremsstrahlung spectrum, Kramers formula is used. It is shown in equation (5.1) up to the second order [40]. The endpoint of the continuum is labeled E_0. The parameters A and B are scaling factors.
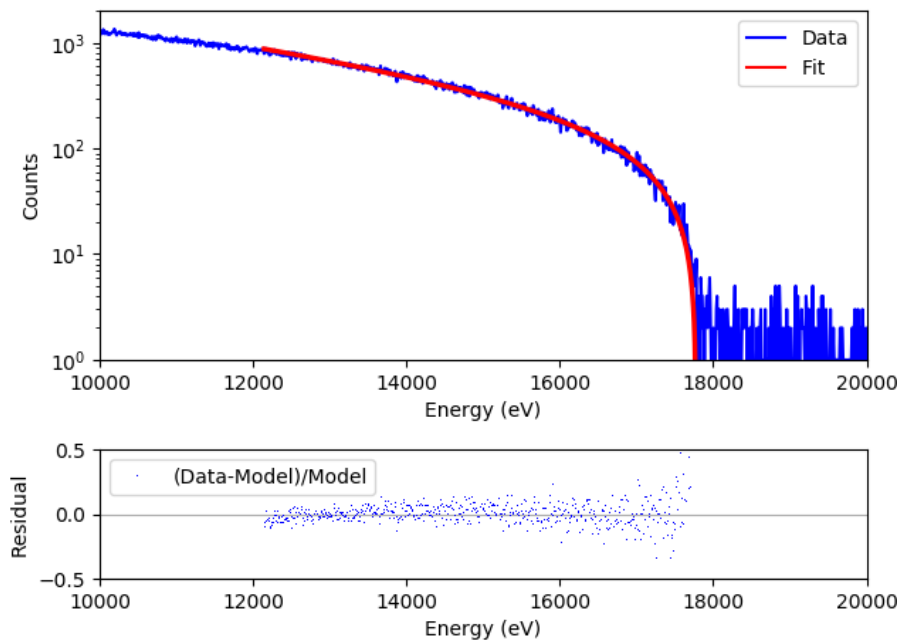
FIGURE 5.2: **Bremsstrahlung spectrum for detector S0-1**
The spectrum in the central pixel of detector S0-1 for electrons at around $18\,\text{keV}$ produced in 12 hours of measurement at maximum rate of the SEM is shown in blue. In red the fit using Kramers formula is shown. The endpoint is estimated around $(17.757 \pm 0.007)\,\text{keV}$. On the bottom of the plot the residuals in units of sigma are shown.
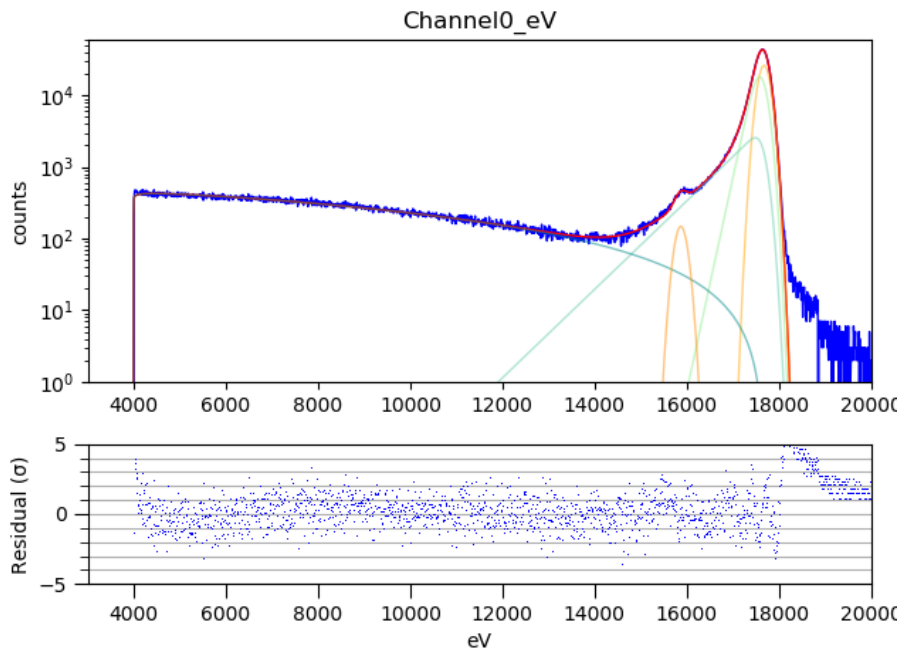

FIGURE 5.3: **Electron Spectrum of detector S0-1**
In blue the electron spectrum of detector S0-1 at around $18\,\text{keV}$ is shown. In red a fit for the entire spectrum is drawn. The sub functions of the fit are shown as well. The maximum of the peak is at $(17.648 \pm 0.001)\,\text{keV}$. On the bottom the residual between the fit and the spectrum can be seen. The empirical fit function is described in chapter 7.2.

$$f(E) = A \cdot \frac{E_0 - E}{E} + B \cdot \frac{E_0 - E}{E^2} \tag{5.1}$$

The fit for the endpoint starts at 12.5 keV and is stopped close to the expected endpoint. This method turned out to be the most accurate and reliable one, since no background model that would improve the fit above the endpoint, could be found. The endpoint is estimated around (17.757 ± 0.007) keV. This value calibrates the electron gun and can simultaneously be used to compare to a electron spectrum created with the same incoming energy.

5.2 Determination of the Energy Shift

To measure the energy shift for electrons the aluminum foil is removed and the heating current is tuned down again. The electron measurement is performed in 30 minutes and is shown in figure 5.3. The most probable energy value deposit in the detector is represented as the maximum of the main peak. Therefore, it is chosen as the reference point for the deposit energy in the detector. To estimate the maximum of the main peak, the spectrum is fitted with an empirical model described in chapter 7.2. The peak position is then defined as the maximum of the fit at (17.648 ± 0.001) keV. To estimate the error on the maximum the fit curve is reproduced 10000 times according to the errors on its parameters. To include all correlations between the parameters as well the set of curves is produced with the covariance matrix of the fit. For the resulting set of fit curves the maximum of each of them is calculated. The probability distribution of the maxima is fitted with a Gaussian function as seen in figure 5.4. The width of this peak is then used as the standard deviation on the maximum while the mean of the Gaussian is used as the value of it.

Comparing the endpoint of the Bremsstrahlung spectrum, which represents the energy deposit without any influences of the entrance window, to the maximum of the electron measurement reveals an energy shift of (99 ± 7) eV at around 18 keV. The error is calculated using quadratic error propagation with the error on the endpoint and the maximum as shown in equation (A.12).
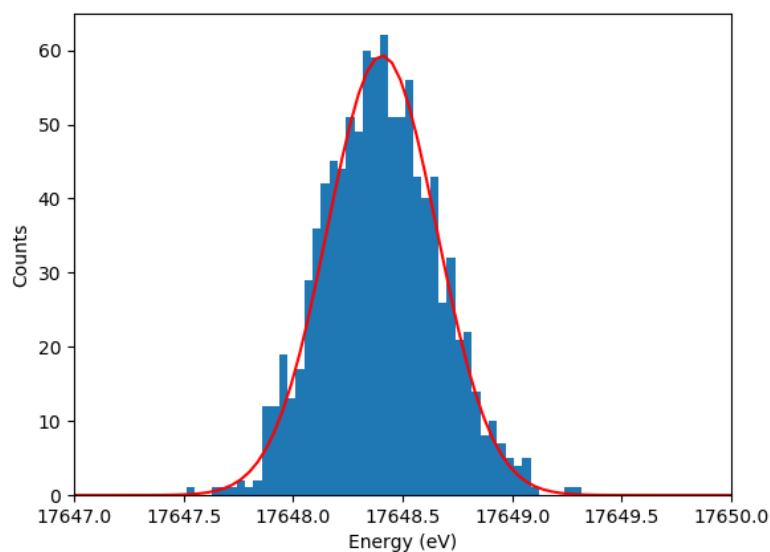
FIGURE 5.4: **Error estimation for peak maximum**
The estimated maxima according to the probability distribution given by the covariance matrix
of the electron peak fit for 10000 tries is shown in blue. The distribution is fitted with a
Gaussian function illustrated in red. The mean of the Gaussian is $E_0 = 1768.4\,\text{eV}$ and the
width is $\sigma = 0.6\,\text{eV}$.

5.3 Determination of Dead-Layer Thickness

To relate this energy shift introduced by the entrance window, the assumption is made
that the entrance window can be described by a dead-layer on top of the sensitive volume
with a thickness d. It can be estimated by comparing the measured energy to a simulation
or theoretical predictions, such as Bethe-Bloch. As shown in detail in chapter 7.1 Bethe-
Bloch is not suitable for the approximation of the dead-layer and differs up to a factor of
two from the dead-layer thickness obtained with simulations. On top of this the Bethe-
Bloch formula can only represent the entrance window in its simplest form, the dead-layer.
If the model is adjusted to a more sophisticated entrance window model, the formula can
not represent it any more. Therefore, to relate the energy shift introduced by the entrance
window to the physical property of the detector, simulations are used. In this chapter
electrons with $18\,\text{keV}$ are simulated with the Monte Carlo simulation software KESS [26]
for different thicknesses of a dead-layer. The energy shift of the maximum of the main
peak in the simulation is estimated in the same way as for the measurements of electrons
and is compared to the set energy of the electrons.

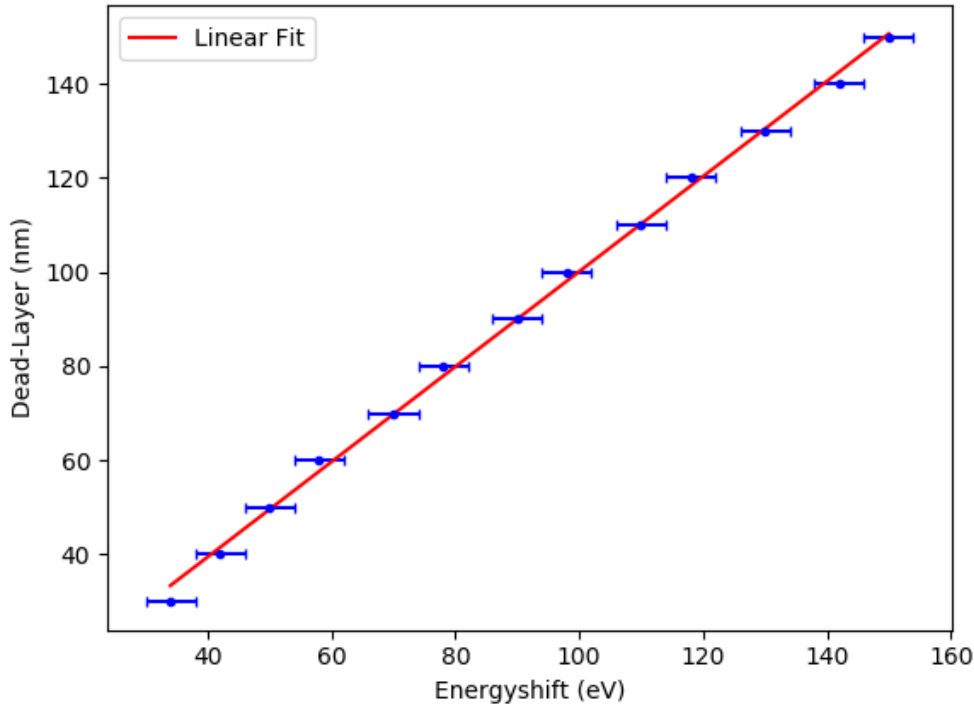Figure 5.5 shows the correlation of the energy shift to the thickness d of the dead-layer

FIGURE 5.5: **Correlation between energy shift and dead-layer at** $18\,\mathrm{keV}$
Estimation of the energy shift of $18\,\mathrm{keV}$ electrons over the thickness d of a dead-layer on top of the sensitive volume from simulation. The correlation between energy shift and dead-layer is approximated with a linear function in the region of interest. For the slope the correlation is $(1.011 \pm 0.013)\,\frac{\mathrm{nm}}{\mathrm{eV}}$ and for the offset $(-1.0 \pm 1.4)\,\mathrm{nm}$.

for electrons at $18\,\mathrm{keV}$. In the region of interest the correlation can be approximated with a linear fit. The conversion of the measured energy shift of detector S0-1 corresponds to a dead-layer of $d = (99 \pm 7)\,\mathrm{nm}$.

5.4 Conclusion

By using a thin aluminum foil it is possible to calibrate the electron gun of the SEM to the order of a few electron volts and measure the energy shift created by the entrance window. The energy shift can be used to relate the physical property of the detector's entrance window to simulations. In this case, the model for the entrance window is assumed as a dead-layer on top of the detector and estimates a thickness of this layer of $d = (99 \pm 7)\,\mathrm{nm}$. To evaluate a more sophisticated entrance window model with more than one parameter, further measurements have to be performed at different energies. Since the effect of the

entrance window is stronger for lower energies, measurements in the low keV-range are preferred. In theory this is possible with the method presented in this chapter, but as the calibration of the electron gun requires a long time, it is not applicable with the current setup in the SEM. A better calibration of the electron beam with another method could solve this issue and would allow an even more precise measurement of the entrance window in much shorter time, since the calibration with Bremsstrahlung would not be required.

6 Investigation of Entrance Window Effects with the Tilted Detector Method

Since the method described in chapter 5 is rather time consuming due to the calibration of the electron gun, another method, which does not heavily rely on a calibration of the electron gun, is required. The method tested in this chapter uses the fact that by tilting the detector, the effective path of electrons increases inside the entrance window proportionally to the cosine of the angle. In the first part of this chapter, this method is applied to measure the entrance window thickness in the dead-layer model and is then compared to the measurements performed in chapter 5 to crosscheck the results. In the second step, different detectors are investigated with this method to compare them with each other. The goal of this investigation is to find the best detector type between the available entrance window doping profiles.

6.1 Measurement of Energy Shift for the Tilted Detector Method with Mono-Energetic Electrons

The method to measure the imprint of the entrance window, tested in this chapter, uses the fact that the 'seen' entrance window thickness by the electrons can be artificially increased by tilting the detector. To illustrate the dependency of the distance traveled over the incoming angle, two assumptions are made to simplify the model. It is assumed that in average electrons travel in a straight line on the scale of the dead-layer thickness. The illustration of the resulting equation (6.1) is shown in figure 6.1. As one can see, the distance traveled in the dead-layer λ increases over the angle and thus the electrons interact effectively with a larger dead-layer. The y-axis is given in units of additional
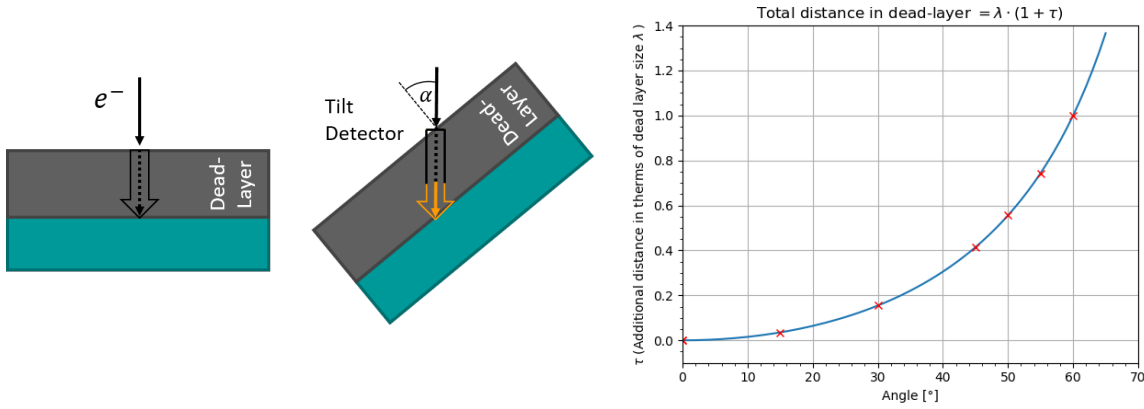
FIGURE 6.1: **Illustration of tilting detector method**
On the left-hand side, an illustration of the effect inside the detector is shown. The additional distance, which an electron has to travel if the detector is tilted, is marked in yellow. On the right-hand side this additional distance traveled in a dead-layer over the angle is shown. The assumption is made that electrons travel in average in a straight line. The dead-layer thickness is given as λ while τ denotes the additional factor traveled in the dead-layer. At the angle of $60°$ the additional distance traveled in the dead-layer is $\tau = 1$ and therefore the total distance traveled is twice the distance of the dead-layer.

dead-layer thickness τ.

$$\cos(\alpha) = \frac{\lambda}{\lambda \cdot (\tau + 1)} \Leftrightarrow \tau = \frac{1}{\cos(\alpha)} - 1 \tag{6.1}$$

Since the absolute thickness is not known, only the relative change can be measured and therefore measurements at $0°$ are used as a reference point. For an angle of $60°$, the additional distance traveled in the dead-layer is at the size of the dead-layer λ itself, which is a good reference point to the dead-layer thickness.

To measure the angular dependency, multiple data points are taken for various angles as illustrated with the red crosses in figure 6.1. For higher angles more data points are taken as the effects of the dead-layer are stronger.

Since the additional dead-layer thickness τ is a quantity that cannot be measured directly, the dependency has to be converted. The information required is the average loss of energy over the distance traveled. With this conversion factor from simulations the peak position of the electron spectrum can then be used to measure the dead-layer.

With the direct comparison to simulations the assumptions made about the path of the electrons and the entrance window model are not required anymore, which makes this method also usable for lower energies and for different entrance window models.

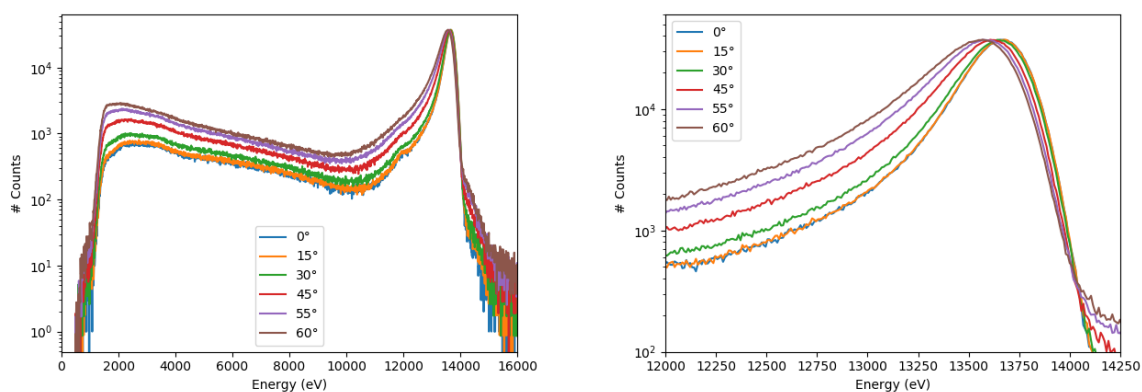The measurements are performed for an electron beam with $14\,\text{keV}$, since the effects

FIGURE 6.2: **Electron Spectrum of detector S0-1 at** $14\,\mathrm{keV}$ **for different angles**
On the left-hand side the entire spectrum is plotted. On the right-hand side a zoom on the main peak is drawn. The measurements are normalized to the measurement at $0°$. The shift to lower energies for an increasing angle can be seen at the maximum.

are larger for lower energies. To collect the same statistics inside the main peak, the measurement time is increased for higher angles to compensate for the smaller effective detector size. To achieve a peak height of 10^4 counts in the finest binning of the ADC the measurement at 0° runs for 30 minutes, while the measurement at 60° takes 60 minutes. In figure 6.2 an exemplary spectrum for detector S0-1 can be seen for various angles. To simplify the comparison by eye, all spectra are slightly re-scaled to the same peak height. As expected the shoulder of the main peak at lower energies increases due to the additional distance the electrons have to travel in the entrance window area for higher angles. As one can see on the right-hand side of the figure, the peak position shifts to lower energies for larger angles. This shift corresponds directly to the additional distance the electrons have to travel in average in the dead-layer of the entrance window.

6.2 Determination of Dead-Layer Thickness

To calculate the energy shift between the measurements at different angles the peak position at an angle of 0° is used as the reference point. The energy shift ΔE is defined positively, even though the peak position E_{max} moves to lower energies for larger angles, and is shown in equation (6.2).

$$\Delta E(\alpha) = E_{\mathrm{max}}(0°) - E_{\mathrm{max}}(\alpha) \tag{6.2}$$
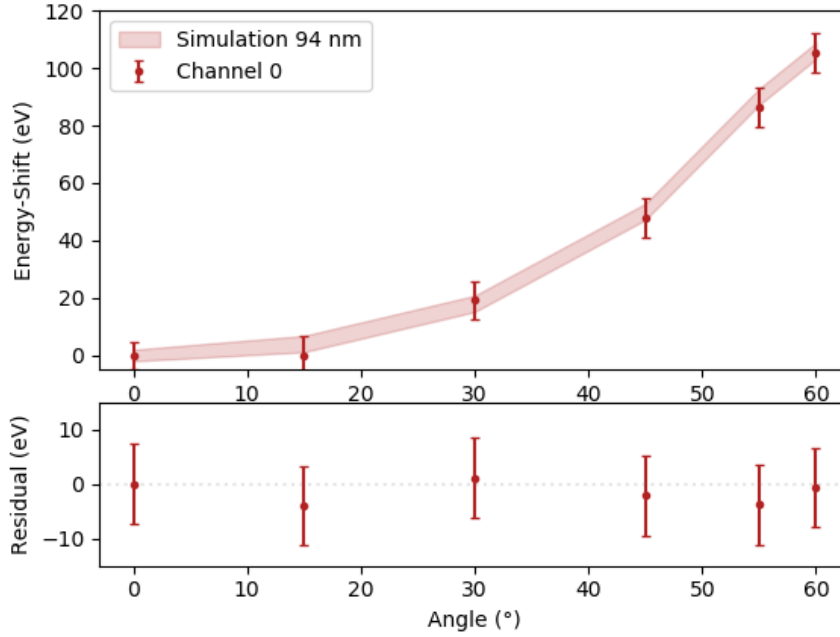
FIGURE 6.3: **Energy shift of detector S0-1 over the angle**
The energy shift of the electron peak position for detector S0-1 in reference to a measurement performed at $0°$ is shown at the top. The best relation to the simulation is found for $94\,\text{nm}$ dead-layer. At the bottom the residuals in electron volts are shown.

The maximum E_{max} of each electron spectrum is estimated by a fit of the main peak. The error of the peak position is estimated by the variation of the fit using the covariance matrix as shown in chapter 5.2. For small energy differences the calculation of the energy shifts is independent of the absolute calibration and only depends on the error $\sigma_{E_{i,\text{max}}}$ of the peak position as given in chapter A.3. Therefore it is independent of the absolute calibration of the electron gun to only 2%.

The measured energy shifts for the central pixel of detector S0-1 are shown in figure 6.3. To estimate the dead-layer, the simulations for the same incident angles as the date are fitted and the peak positions are calculated. The simulations are created for different dead-layer thicknesses with a step size of $2\,\text{nm}$. To receive the best agreement between model and data, the minimum of the χ^2 over the dead-layer thickness is calculated as shown in equation (6.3).

$$\chi^2 = \sum_i \frac{(\text{Data}_i - \text{Model}_i)^2}{\text{Model}_i} \tag{6.3}$$

The error is sized up as the width of the almost parabolic shaped χ^2-curve over the dead-layer thickness at $\chi^2 + 1$. This results in a dead-layer thickness for detector S0-1 of $(94 \pm 7)\,\text{nm}$. The corresponding simulation, including errors, can be seen in figure 6.3 in the shaded band. Simulation and data both resemble in the angular dependency as described in section 6.1. The residuals in units of energy are shown at the bottom. Within the errors, simulation and data points are in good agreement.

6.3 Conclusion

With the method of tilting the detector and therefore artificially increasing the effects of the entrance window, it is possible to measure the entrance window thickness. No additional calibration of the electron gun is required, which makes this method much more applicable and faster to perform, compared to the method described in chapter 5. The comparison of both methods shows a nice agreement between them, with estimations of the dead-layer for detector S0-1 to be $(99 \pm 7)\,\text{nm}$ in case of the Bremsstrahlung method and $(94 \pm 7)\,\text{nm}$ for the tilting detector method. As both methods are performed at different energies and with different types of determining the dead-layer thickness, they are independent from each other and therefore can be used to crosscheck each other. On top of this, it also confirms the possibility that the effects of the entrance window can be related to a physical property of the detector, which is independent of the energy of the incoming electrons. This property of the detector can be used as input for the model of the detector response in either simulation or in an analytic model.

With further measurements at different energies, especially for lower energies, it could be possible to calculate the entrance window with a more sophisticated model and to a higher precision, which can then be used in simulations for a more accurate reproduction of the detector electron response. Nevertheless the method presented in this chapter can be used to directly compare different detectors in regard of their entrance window thickness.

6.4 Comparison of Standard Technology Detectors

In the first step, two detectors of the same doping profile, S0-1 and S0-2 are compared with the method of tilting the detector. The energy spectra at $14\,\text{keV}$ for both detectors are shown on the left-hand side in figure 6.4. To improve the visibility of shape effects, which correspond to the entrance window thickness, the spectra are slightly re-scaled to

the same height and the same peak position. As one can clearly see, the peak shape of detector S0-1 is much broader (FWHM = 326 eV) compared to detector S0-2 (FWHM = 286 eV). Also the escape peak for detector S0-1 is barely visible compared to the escape peak of detector S0-2. Nevertheless the comparison of the energy resolution for photons of these two detectors shows that they are very similar. The combination of these two observations, with a worse energy resolution for electrons, but the same for photons, can be explained by a thicker entrance window of detector S0-1. This hypothesis is supported by the higher energy shift (and therefore entrance window thickness) measured for detector S0-1, which is almost twice as high compared to S0-2, as seen on the right-hand side in figure 6.4.

To rule out that this discrepancy of the entrance window thicknesses between the detectors is an aging effect of the detectors, the resolution of S0-1 over the time is checked, since S0-1 has been used in multiple measurement campaigns and different setups. Nevertheless no dependency on the time nor the radiation dose could be found. Therefore, the detector's entrance window has been thicker from the beginning on. Currently the best hypothesis is that during the first wave of production of 7 channel TRISTAN prototype detectors some effect lead to a larger entrance window. This hypothesis is supported by the fact that all other detector chips possess an entrance window thickness of only half of the measured value for detector S0-1. The reason for this discrepancy is still unclear and requires further investigations.
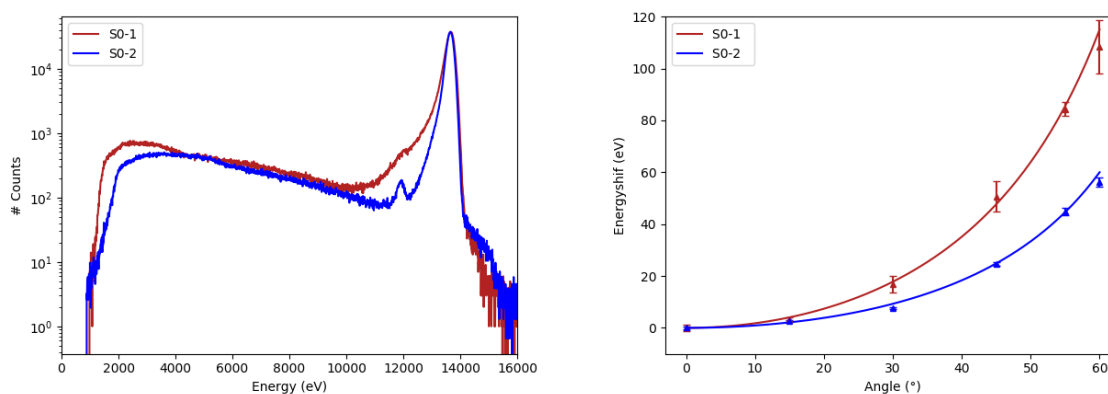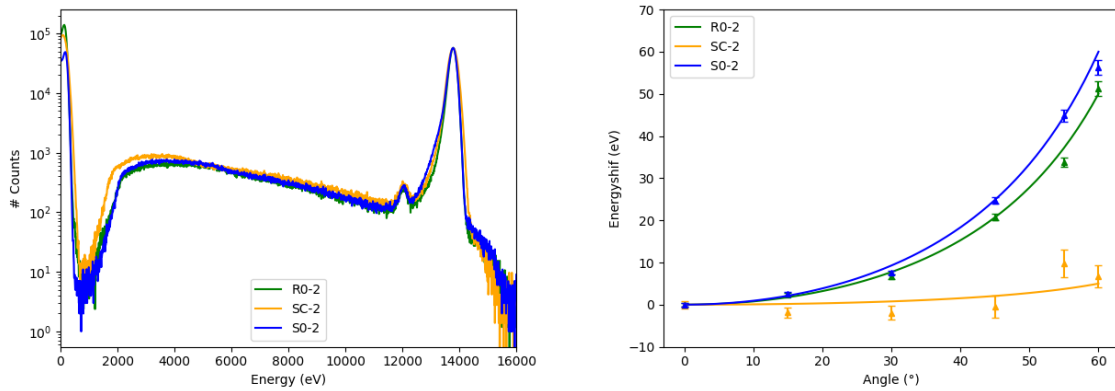
FIGURE 6.4: **Detector comparison S0-1 and S0-2**
On the left-hand side the electron spectrum for detector S0-1 and S0-2 can be seen. The amplitude and position of the main peak are overlapped to simplify the comparison of the peak shape. On the right-hand side the energy shift of both detectors is shown to illustrate the effect of the entrance window for each detector. Each data point corresponds to the weighted mean for all 7 pixels. For easier visual comparison a rough regression curve for the data points is drawn.

## 6.5 Comparison of Entrance Window Doping Profiles

In the next step, different detectors with different entrance window doping profiles will be compared to each other to validate if a large improvement compared to the standard technology can be achieved. This comparison is made to find the best suitable detector for the TRISTAN project, assessing three mayor requirements for the project. As shown in chapter 2.3 the first requirement is that the energy resolution has to be below $300\,\mathrm{eV}$ at $20\,\mathrm{keV}$. Additionally a low energy threshold is required to understand effects like back scattering and charge sharing. Both motivate a thin entrance window or dead-layer.

To compare all the different detector types, the most important properties concerning these requirements are shown in table 6.1. The spectra for the investigated detectors S0-2, R0-2 and SC-2 in the central pixel can be seen in figure 6.5. Again the spectra are slightly re-scaled and the peak positions are overlapped to simplify the visual comparison in the plot. On the right hand side, the energy shift over the angle for the different detectors is drawn. As one can clearly see detector SC-2 is almost not effected by the entrance window, leading to a thin dead-layer and almost no dependency of the energy shift and resolution over the angle. Nevertheless the overall resolution for electrons is about 20% worse, compared to the standard technology detector S0-2. The same effect can be seen for the resolution for photons, which are independent of the dead-layer. Looking at the waveforms of both detectors, this difference in the resolution can be explained by the 5

TABLE 6.1: **Overview table of measured properties for the different 7 channel TRIS-TAN detectors**

All measurements are performed at room temperature inside the scanning electron microscope. The resolutions are calculated as the average of all pixels. For the measurements the FWHM is approximated by the width at the half height of the main peak.

Property Detector	S0-2	R0-2	SC-2	S0-1
Dead-Layer	$(52 \pm 7)\,\mathrm{nm}$	$(46 \pm 6)\,\mathrm{nm}$	$(6 \pm 7)\,\mathrm{nm}$	$(94 \pm 7)\,\mathrm{nm}$
FWHM(e^-) at 0° for 14 keV	$(261 \pm 6)\,\mathrm{eV}$	$(259 \pm 6)\,\mathrm{eV}$	$(323 \pm 6)\,\mathrm{eV}$	$(314 \pm 6)\,\mathrm{eV}$
FWHM(e^-) at 60° for 14 keV	$(313 \pm 6)\,\mathrm{eV}$	$(310 \pm 6)\,\mathrm{eV}$	$(357 \pm 6)\,\mathrm{eV}$	$(451 \pm 6)\,\mathrm{eV}$

FIGURE 6.5: **Detector Comparison S0-2, R0-2 and SC-2**

On the left-hand side the electron spectrum for the detectors S0-2, RC-2 and SC-2 can be seen. The amplitude and position of the main peak are overlapped to simplify the comparison of the peak shape. On the right-hand side, the energy shifts of all detectors are shown to illustrate the effect of the entrance window for each detector. Each data point corresponds to the weighted mean for all 7 pixel. For easier visual comparison rough regression curves for the data points are drawn.
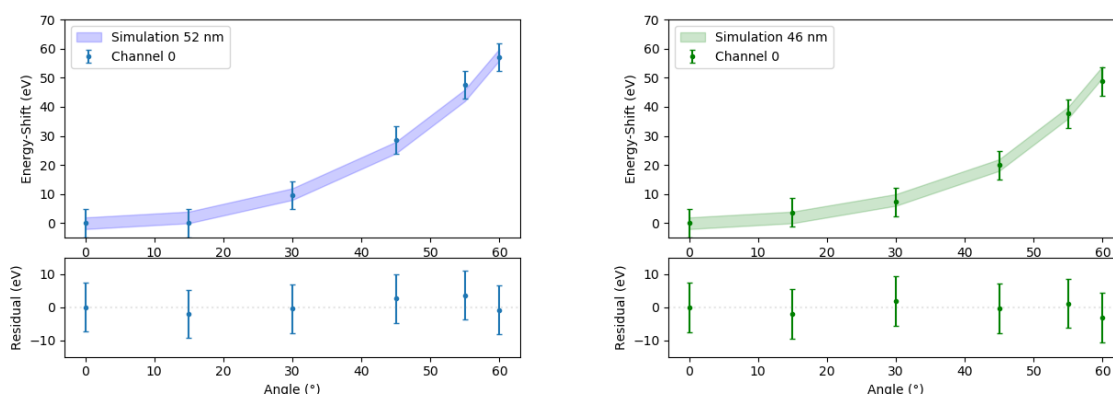
FIGURE 6.6: **Energy shift of detector S0-2 and R0-2 over the angle**
The energy shift of the electron peak position for detector S0-2 (left-hand side) and R0-2 (right-hand side) in reference to measurement performed at $0°$ is shown at the top. The best relation to the simulation for S0-2 is found for $(52 \pm 7)\,\mathrm{nm}$ dead-layer. For detector R0-2 the optimum is found at a dead-layer of $(48 \pm 6)\,\mathrm{nm}$. At the bottom of both plots the residuals between the data and the simulation are shown in units of electron volts.

times higher leakage current for detector SC-2. Even though detector SC-2 has a much thinner entrance window, the drawback of this doping profile is a much worse energy resolution. Cooling the detector could reduce this effect, but not to the same level as S0-2. Therefore this doping profile is probably not applicable for the final TRISTAN detector, nevertheless a sensitivity study is required to check this hypothesis in detail.

The two energy shift curves to estimate the dead-layers of detector S0-2 and R0-2 for the central pixel can be seen in figure 6.6. The absolute values are shown in table 6.1 and it can be seen that dead-layer and energy resolution of both detector overlap inside the error bars. Even though the values for detector R0-2 are slightly better than for S0-2, both of the detectors fulfill the requirement of energy resolution less than 300 keV and the difference between them is less than 1%. Therefore, both of these detectors could be applicable for the TRISTAN project.

From the point of view of the overall energy threshold, these measurements can not make any statements, since they are performed at higher energies. In addition to this the measurement technique in this thesis can not measure shape distortions to such a precision to differentiate the two detector types. To answer this question precisely, investigations have to be performed to estimate the influence of the effects on threshold and the overall shape distortion on the sensitivity of TRISTAN for keV sterile neutrinos.

7 First Steps Towards a Full Model of the Detector Response

The response of a detector can be defined as the modification of the spectrum obtained from a mono-energetic electron beam. To reproduce and understand the detector response of the TRISTAN prototype detectors, simulations of mono-energetic electrons entering silicon are produced and compared to measurements. On top of this the effects on the peak position of the electron spectrum are extracted for the dead-layer model. In the second part of this chapter an empirical model is developed and tested to describe the detector response. The dependency of the model parameters are investigated for different incident angles.

7.1 Full Monte Carlo Simulation to Model the Detector Response

To understand the detector response of the TRISTAN prototype detectors more precisely, the energy spectrum of mono-energetic electrons entering a silicon detector is simulated and compared to measurements. Electrons with $18\,\mathrm{keV}$ interact in average only 3.8 times over the distance of $100\,\mathrm{nm}$, which makes the energy loss in a layer of this size basically random[26]. These statistical fluctuations of the energy deposit in thin layers can be accounted for in a simulation, but not in analytic formulas, like Bethe Bloch, which describe the average loss for many interactions. Nevertheless these fluctuations of the energy loss in a thin layer are important to model the effects of the entrance window. With Monte-Carlo simulations it is possible to describe every interaction point of the electron from fundamental principles and therefore account for these fluctuations. The effect of the entrance window can then be integrated into the simulation by a variation of the charge collection efficiency depending on the position in the detector.

In this thesis the Monte Carlo simulation software KESS [26] is used to accomplish this task, since it especially has been written to investigate entrance window profiles for silicon

detectors.

An exemplary energy spectrum at 14 keV, produced with simulations, can be seen in figure 7.1. To model the entrance window, a dead-layer with a size of 52 nm is used. The data to compare to the simulation is taken with detector S0-2 inside the SEM. For energies above the main peak the data differs strongly from the simulation. The reason for this is pile-up which has been measured in the data but has not been simulated. The pile-up seen in the data is rather high in comparison to the expected rate given the average count rate in the detector and the energy filter settings. The explanation for this are the noisy waveforms seen in figure 4.12. Even though it is possible to recreate this effect, the impact on the spectrum in the main peak and below is rather small and therefore is neglected in the further investigations.

As seen in the spectrum and the residuals, simulation and measurement match nicely in the area around the main peak and the back-scatter part of the spectrum. But at the lower part of the main peak, around the energy of the escape peak, the simulation differs from the measurement. This difference is also seen in the residuals and indicates that the entrance window is not perfectly modeled by a dead-layer. A more sophisticated model like the partial event model described in section 3.3 could solve this deviance. Nevertheless such a model increases the number of parameters and therefore the complexity. Since the overall agreement is good, especially around the maximum of the main peak, which is used for the investigations in chapter 5 and 6, the step away from the dead-layer model to a more sophisticated model has not been made.

As shown in chapter 5 and 6, one parameter that can represent the effects of a dead-layer is the energy shift of the spectrum. To measure this effect, the peak position of the main peak is compared to the peak position without any dead-layer, and therefore the energy of the incoming particle. The dependency of the energy shift over the thickness of the dead-layer can be seen in figure 7.2. On the left-hand side the simulated energy shift of the main peak for various energies is shown. As one can see, the effect introduced by the dead-layer increases for lower energies.

On the right-hand side of figure 7.2 the simulated energy shift of the main peak for electrons at 14 keV over the angle can be seen. The peak position at 0° is chosen as the reference point and therefore the observed curve defines the additional energy loss in a dead-layer when the detector is tilted. With these simulations the dead-layer of a given detector can now be estimated by comparison to the measured energy shift of the main peak with these simulations.
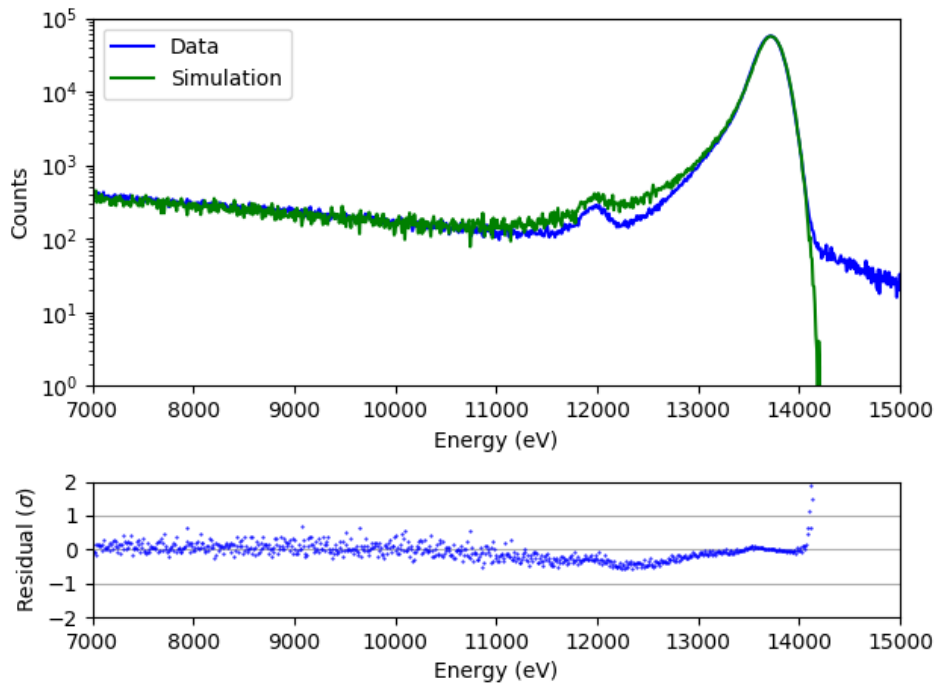
FIGURE 7.1: **Comparison of energy spectrum between simulation and data**
The simulations are produced with the dead-layer model and a thickness of $52\,\text{nm}$ at an energy of $14\,\text{keV}$. The spectrum is illustrated in green. The data is taken with detector S0-2 and is shown in blue. The pile-up seen for the date above the main peak is not modeled. At the bottom the residuals between data and model in units of the standard deviation can be seen.
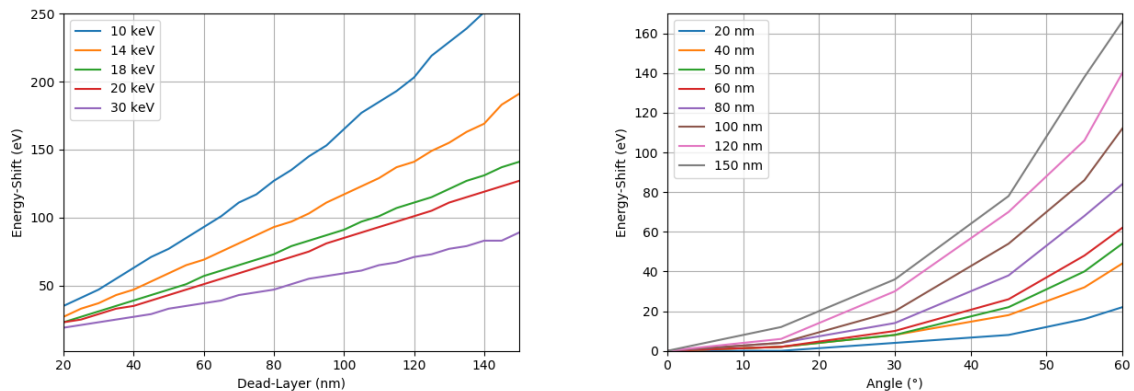

FIGURE 7.2: **Dead-layer thickness over the energy shift**
On the left-hand side the energy shift of the main peak for electrons at different energies is shown over the thickness of a dead-layer. On the right hand side the additional energy shift depending on the incident angle is shown for electrons with $14\,\text{keV}$. Both plots are obtained from simulations.

7.2 Modeling an Analytic Detector Response

Even though simulations are very useful to model the response of detectors, it is rather time consuming to produce them. To simplify this task, an empirical model is designed to describe the detector response for mono-energetic electrons. In equation (7.6) the empirical model used to describe the intensity curve for mono-energetic electrons is shown. To model the electrons in the main peak a Gaussian function I_G is assumed. Without entrance window effects this part would represent the electrons that deposit all their energy in the detector, while the width σ of the Gaussian accounts for the noise and statistical fluctuations in the production of secondary electrons. To account for the entrance window effects an exponential step function I_{D1} is introduced [41]. It describes the electrons that interact more often in the entrance window area and therefore models the lower energy part of the main peak. Especially at lower energies or thicker entrance windows it has been found that a second exponential step function I_{D2} improves the agreement of measurement and model. The parameter β characterizes the steepness of this tail while A_D describes the overall amplitude. Since electrons scatter when they interact with matter, it is possible that they leave the detector again, without depositing their entire energy. To describe the back scatter part of the spectrum and the area around the thrshold, function I_B is used [41]. Hereby a denotes the energy where the threshold is set and b describes the shape around this area. The parameter c models the part of the spectrum where the electrons have deposit most of their energy but still left the detector with some energy remaining. Therefore the function ends at the position of the main peak. To model the silicon escape peak a Gaussian function I_{esc} is used. This energy loss created by the escape of a K_α photon is denoted with ΔE_{esc} and is expected to be $1,74\,\text{keV}$.

$$I_G = A_G \cdot \exp\left(\frac{-(E_0 - E)^2}{2\sigma^2}\right) \tag{7.1}$$

$$I_{D1} = A_{D1} \cdot \exp\left(\frac{E - E_0}{\beta_{D1}}\right) \cdot \text{erfc}\left(\frac{E - E_0}{\sqrt{2}\cdot\sigma} + \frac{\sigma}{\sqrt{2}\cdot\beta_{D1}}\right) \tag{7.2}$$

$$I_{D2} = A_{D2} \cdot \exp\left(\frac{E - E_0}{\beta_{D2}}\right) \cdot \text{erfc}\left(\frac{E - E_0}{\sqrt{2}\cdot\sigma} + \frac{\sigma}{\sqrt{2}\cdot\beta_{D2}}\right) \tag{7.3}$$

$$I_B = A_B \cdot \left(\frac{E}{E_0 - a}\right)^b \cdot \left(1 - \frac{E}{E_0}\right)^c \tag{7.4}$$

$$I_{esc} = A_{esc} \cdot \exp\left(\frac{-(E_0 - \Delta E_{esc} - E)^2}{2\sigma^2}\right) \tag{7.5}$$

$$\Rightarrow I = I_G + I_{D1} + I_{D2} + I_B + I_{esc} \tag{7.6}$$
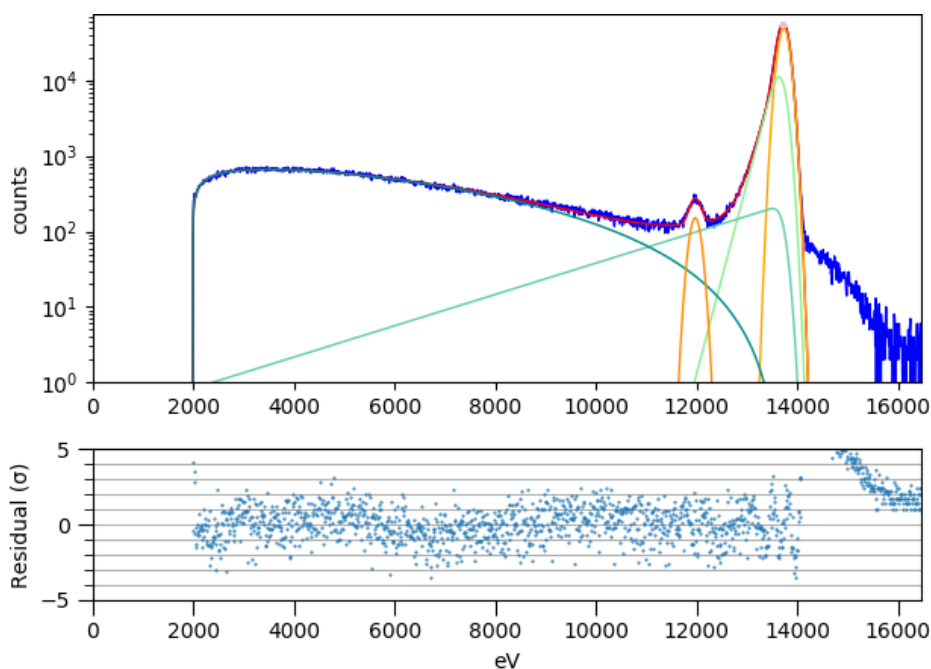
FIGURE 7.3: **Exemplary energy spectrum at** $14\,\text{keV}$ **for detector S0-2**
The red line represents the empirical model that is fit to the spectrum. The different parts of
the model are illustrated in yellow, green and cyan. The pile-up part above the main peak is
neglected for the fit. At the bottom the residuals between the model and the data are shown.

A fit of the empirical model described in equation (7.6) can be seen in figure 7.3. Since
a rather large periodic noise was apparent for the measurements in the SEM, a pileup
shoulder at energies higher than the main peak can be seen. Nevertheless, for the analysis
and tests in the thesis, this part is neglected for the fit. For the rest of the spectrum the
agreement between the empirical model and the data is good.

To test if the empirical model can be used to describe the electron spectrum for different
incident angles, the dependence of the model parameters is investigated. Therefore mea-
surements of mono-energetic electrons are performed for $14\,\text{keV}$ with different incident
angles and fitted with the empirical model. All parameters that are related to the effects
of the entrance window are expected to depend on the incident angle α. To model this,
the dependence in formula (7.7) can be used. Thereby denotes τ the parameter that
is investigated. τ_s describes the curvature and τ_0 the offset. This formula is motivated
by the angular dependence of the dead-layer as derived in chapter 6.1. For clarity and
simplicity reasons only the dependence of the most important parameters is discussed in
the next paragraphs.

$$f(\alpha)_\tau = \tau_s \cdot \left(\frac{1}{\cos(\alpha)} - 1 \right) + \tau_0 \tag{7.7}$$

In figure 7.4 the maxima of the peaks and the resolution are shown over the incident angle of the electrons. As expected, the peak position shifts to lower energies as the incident angle increases and therefore also the entrance window seen by each particle increases. The dependence of this shift can be nicely fitted with the function given in equation (7.7). For the energy resolution a similar effect is seen. Since the effective entrance window increases with the angle, the peak broadens. Inside the rather large errors also the resolution follows the dependency in (7.7).

The parts of the detector response that directly try to model the effects of the entrance window are given by the parameter β_{D1} and the amplitude A_{D1} (and β_D and A_{D2}). Since the amplitude A_{D1} depends also on the height of the Gaussian A_G, the ratio $R_{D1} = \frac{A_{D1}}{A_G}$ is shown in figure 7.5. One can nicely see that both parameters follow the dependency given by equation (7.7). The last important parameter is the probability of back scattering since it increases with the incident angle. Even though it is not directly related to the effects of the entrance window, the overall probability to back scatter follows the same function. As seen in figure 7.6 the ratio $R_B = \frac{A_B}{A_G}$, given by the quotient of the height of the back scattered part and the amplitude of the main peak, can also be described with the formula given in equation (7.7).

The dependency of the parameters above demonstrate that the model can be used in a predictable manner, for various incident angles between 0° and 60° or even further at a fixed energy. Therefore, it is possible to predict the detector response in an analytic form continuously for the incident angle with only a few measurements.

The next step is to verify that the empirical model also behaves in a predictable manner over different energies. A first quick analysis of energy spectra at different energies shows that the model can represent the shape of the spectrum above $4\,\mathrm{keV}$.

Peak Maximum   Energy resolution in FWHM
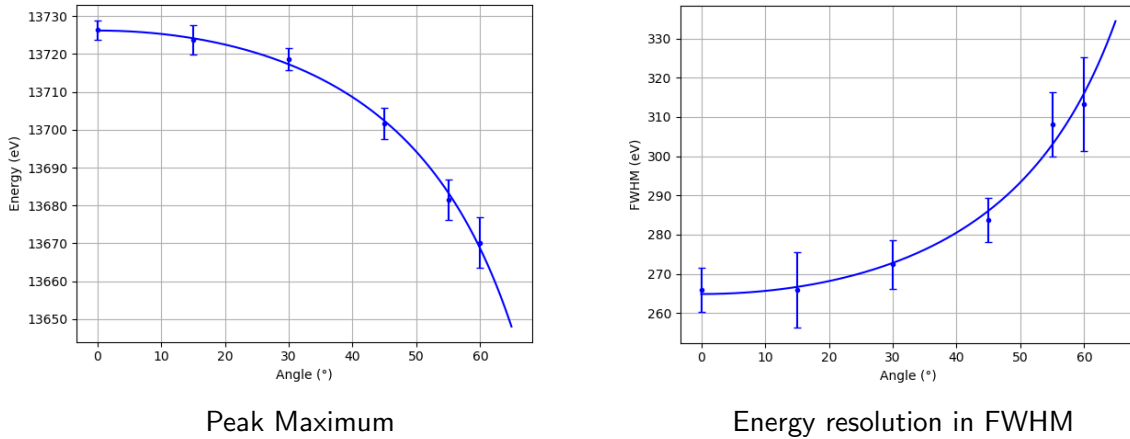
FIGURE 7.4: **Angular dependence of peak maximum and resolution**
On the left-hand side the behavior of the maximum of the main peak can be seen over the angle. On the right-hand side the resolution as FWHM is shown over the angle of incident electrons. The data points in all plots are fitted with formula (7.7). The measurements are performed with detector S0-2 for $14\,\text{keV}$ and the data points represent the average over all pixels.
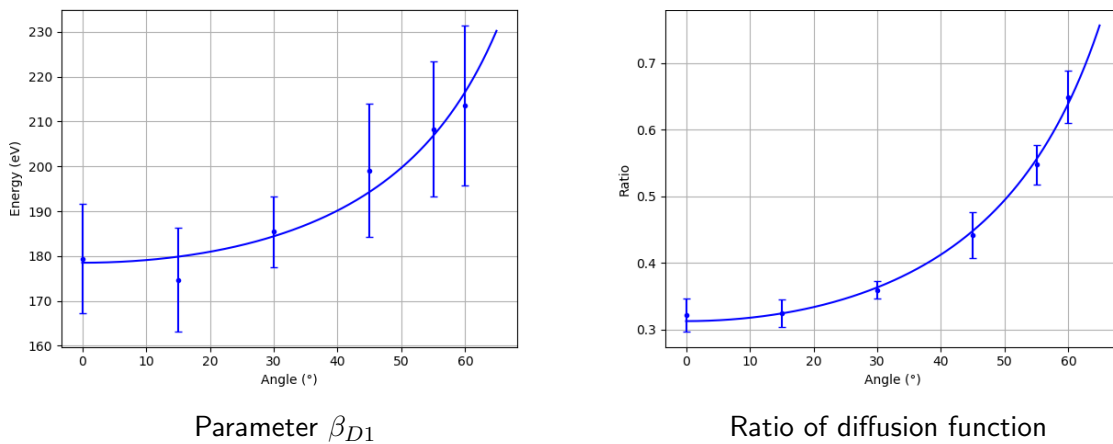

Parameter β_{D1} Ratio of diffusion function

FIGURE 7.5: **Angular dependence of entrance window parameters**
The two plots show the behavior of the parameter β_{D1} and the ratio of the amplitude of the diffusion function compared to the height of the amplitude of the Gaussian. The data points in both plots are fitted with formula (7.7). The measurements are performed with detector S0-2 for $14\,\text{keV}$ and the data points represent the average over all pixels.
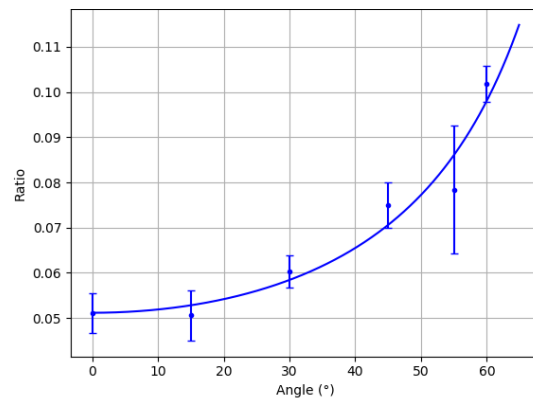
FIGURE 7.6: **Angular dependence of back scatter ratio**
In this plot the ratio $R_B = \frac{A_B}{A_G}$ that corresponds to the quotient of the amplitude of the back scattering part to the height of the main peak, is shown. The data points in the plot are fitted with formula (7.7). The measurements are performed with detector S0-2 for $14\,\mathrm{keV}$ and the data points represent the average over all pixels.

8 Conclusion

In the scope of this thesis, two different methods to estimate the thickness of the entrance window for silicon drift detectors are investigated. With these methods a comparison of different detector technologies was performed, which aimed at reducing the dead layer thickness.

The first method is based on comparing the measured energy peak position to the actual incoming energy. As source for the mono energetic electrons a scanning electron microscope is used, which allows for investigations between $0.5\,\text{keV}$ and $30\,\text{keV}$. Nevertheless, the absolute energy calibration of the electron gun was not precise enough for these investigations. Therefore, it was calibrated to a precision of $7\,\text{eV}$ for electrons at $18\,\text{keV}$, using Bremsstrahlung. To estimate the deposited energy of the electrons the difference from the true energy to the maximum of the main peak was calculated. Simulations were performed to convert the energy shift into a dead-layer thickness.

The second method artificially increases the effective entrance window, through which the electrons travel, by tilting the detector. This allows an estimation of the entrance window thickness without a precise calibration of the electron gun and therefore is less prone to systematic uncertainties and can be performed much faster in the current setup. The link between the energy shift measured from the main peak of the detected electrons to the dead-layer thickness was again made through Monte Carlo simulations.

The comparison of both methods shows good agreement to the estimated dead-layer thickness within the uncertainties. For the Bremsstrahlung method the measured dead-layer of detector S0-1 is $(99 \pm 7)\,\text{nm}$, while it is $(94 \pm 7)\,\text{nm}$ for the tilted detector method. Nevertheless, this detector is not representative of the thinnest achieved entrance window among the measured detectors.

In the next step, the two detectors S0-1 and S0-2, that have the same doping profile and therefore in theory the same entrance window, were compared. Using the method of tilting the detector a dead-layer thickness of $(52 \pm 7)\,\text{nm}$ for detector S0-2 was measured. The reason for this discrepancy of almost a factor of two is still unclear.

Additionally two other detectors with different doping profiles were investigated for their applicability in the final TRISTAN project. Detector SC-2 was produced with an additional counter implementation that reduces the dead-layer to (6 ± 7) nm. But this variation leads to a five times higher leakage current and therefore a much worse energy resolution of (323 ± 6) eV which exceeds the requirements for the TRISTAN project. With additional cooling of the detector, the resolution could be improved but the effectiveness has to be further investigated.

The second detector R0-2 with a different doping profile was produced using a reduced dose of dopendants during the production. The measurements show a slightly thinner dead-layer of (46 ± 6) nm. With the precision of the measurements performed in this thesis detectors S0-2 and R0-2 overlap within uncertainties. To validate an improved performance for the non-standard entrance window detector further investigations are required.

First steps to model the response of the TRISTAN detectors were made with Monte Carlo simulations. An overall good agreement of the spectrum was achieved with simulations that used the measured dead-layer thickness as input parameter. Nevertheless, at the lower part of the main peak a difference between simulation and measurement is seen. To solve this deviation a more sophisticated model like the partial event model is required and has to be tested.

Next to the simulation an empirical model was developed to describe the detector response. Investigations of the model parameters as a function of incident angle show a predictable behavior, which is reproducible. The finalization of the model and its parameters is subject to future work.

The investigations presented in this thesis are an important step towards the final design of the novel TRISTAN detector system. It is the first time that the novel technologies for ultra thin entrance windows were compared and the response to electrons was measured. The results provide a basis for the decision on which technology will be used in the final TRISTAN detector. The next generation of prototype detectors are being produced and first tests will be carried out this year for the more sophisticated 166 pixel module.

A Appendix

A.1 Calculation for Fano-Limit of Silicon

The peak width given by the Fano-statistic can be calculated be with equation (A.1)[42].

$$\sigma_{\text{Fano}} = \sqrt{F \cdot w \cdot E_0} \tag{A.1}$$

For the calculation the Fano-factor at $77\,\text{K}$ $F = 0.114$ is used[1]. The energy per electron-hole pair at this temperature is $w = 3.76\,\text{eV}$[43]. Using an energy of $E_0 = 20\,\text{keV}$ this leads to a Fano limit of

$$\sigma_{\text{Fano}} = 93\,\text{eV} \tag{A.2}$$

$$\sigma_{\text{Fano,FWHM}} = 2\sqrt{2\ln 2}\sigma_{\text{Fano}} \approx 218\,\text{eV} \tag{A.3}$$

In addition to the Fano-statistic one can also add the effect of the noise of the detector and readout chain as shown equation (A.4) with σ_{el}.

$$\sigma_{\text{Fano+Noise}} = \sqrt{F \cdot w \cdot E_0 + \sigma_{el}^2} \tag{A.4}$$

Using the characterization of the TRISTAN prototype detector in [27] at $5.9\,\text{keV}$ one can roughly estimate the electronic noise to $\sigma_{el} \approx 33\,\text{eV}$. Therefore, one can set a lower bound for the resolution that is closer to the conditions in the actual setup. The two different cases for the lower limits can be seen in figure A.1.
Using the estimation for the electronic noise, one can set an limit for electrons at $20\,\text{keV}$ of $\text{FWHM}_{\text{Fano+Noise}} \approx 235\,\text{eV}$ and for electrons at $14\,\text{keV}$ of $\text{FWHM}_{\text{Fano+Noise}} \approx 200\,\text{eV}$.

---

[1]Mean of values in literature. [43]
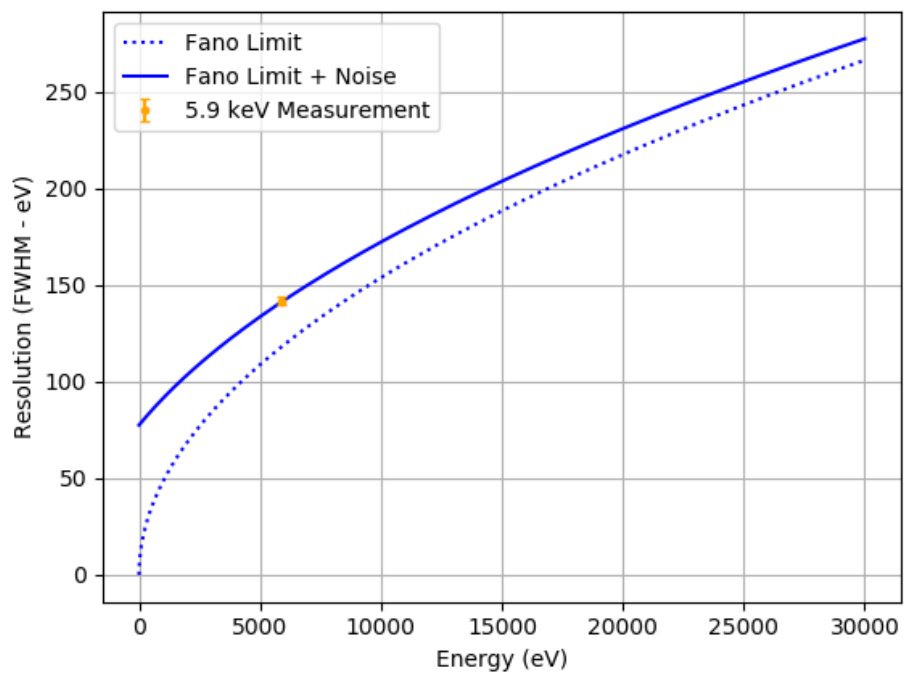
FIGURE A.1: **Fano-Limit**
Visualization of the energy resolution given by the Fano-limit and the Fano-limit and noise as measured in [27]. For the measurement photons have been used.
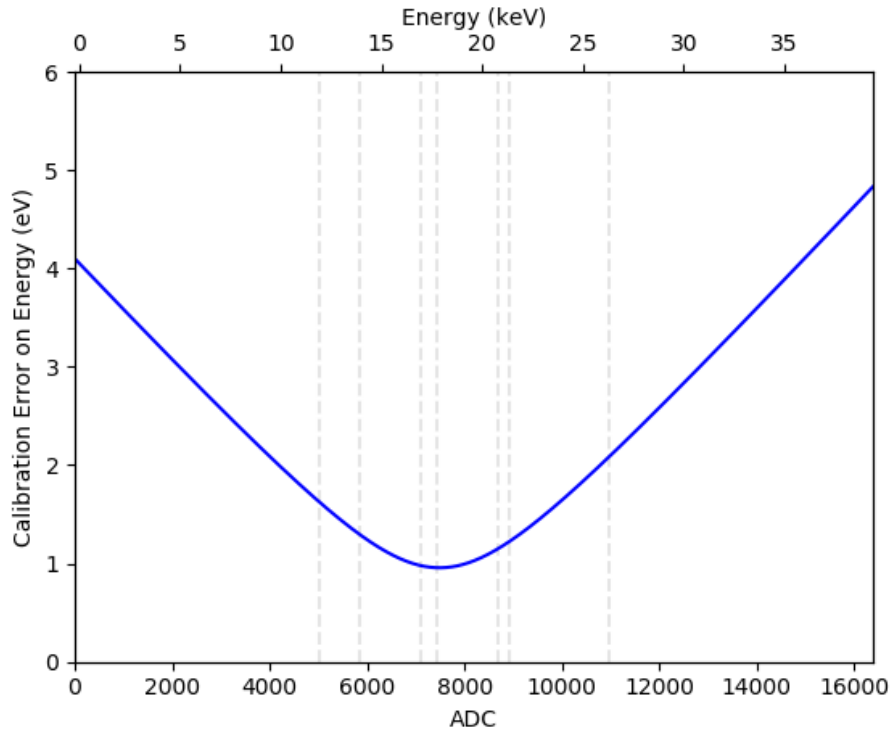
FIGURE A.2: **Estimation of absolute calibration error**
For the estimation the calibration spectrum in section 4.4 is used. In blue the error on the absolute energy is shown. The dashed lines represent the points used for the calibration.

A.2 Error Calculation for Calibration

To relate the ADC values of the DANTE DPP to units in energy the detector is calibrated using a linear function with one parameter for the slope and one parameter for a constant offset. To estimate the error on this calibration curve, the entries of the co-variance matrix for the calibration fit are used as shown in figure A.5. While σ^2_{slope} and σ^2_{offset} describe the diagonal entries of the matrix and correspond to the squared errors, the two parameters the off-diagonal element $\sigma_{\text{slope,offset}}$ represents their correlated error.

$$\sigma_E(\text{keV}) = \sqrt{\sigma^2_{\text{slope}} \cdot x^2 + \sigma^2_{\text{offset}} + \sigma_{\text{slope,offset}} \cdot x} \tag{A.5}$$

The estimation for the error of the exemplary calibration shown in chapter 4.4 can be seen in figure A.2. The absolute error on the energy calibration over the entire ADC range is shown. As expected, the absolute error on the energy calibration is more accurate close to the calibration points and worsens further away from these points. To

perform the calibration, the vacuum chamber has to be opened and the detector turned off. It is assumed that the calibration stays the same inside of one standard deviation given by the error on the calibration. To confirm this assumption inside the precision of the calibration, the energy calibration of the detector S0-1 is performed five times. The different calibration measurements are distributed over three days, while restarting the detector multiple times in between.

The assumption can be made if the error σ_k on the two fit parameter (with k denoting either the slope or the offset of the calibration) is comparable to the statistical fluctuation of the five measurements. The calculation is performed in units of the variance of each parameter. The variance $\mathrm{Var}_{\mathrm{est}}(k)$ of a given parameter k for N measurements is shown in equation(A.6). The error $\sigma_{\mathrm{Var}_{\mathrm{est}}}(k)$ on this variance for N measurements is shown in equation (A.7). To compare the statistical fluctuation $\mathrm{Var}_{\mathrm{est}}(k)$ to the error σ_k of the fit, formula A.8 is used. The significance in units of the error on the statistical fluctuation is for both fit parameter, slope and offset, of around -0.7. Therefore, a change of the calibration between measurements can not be resolved inside the uncertainty of the calibration itself and the assumption that the calibration does not change can be used.

$$\mathrm{Var}_{\mathrm{est}}(k) = \frac{1}{N-1} \sum_i^N (k_i - \bar{k})^2 \tag{A.6}$$

$$\sigma_{\mathrm{Var}_{\mathrm{est}}}(k) = \sqrt{\frac{s \cdot \mathrm{Var}_{\mathrm{est}}^2(k)}{N-1}} \tag{A.7}$$

$$\mathrm{Significance} = \frac{\mathrm{Var}_{\mathrm{est}}(k) - \sigma_k^2}{\sigma_{\mathrm{Var}_{\mathrm{est}}}(k)} \tag{A.8}$$

A.3 Error Calculation for Energy Shift Measurements

The error for calculations of energy shifts is shown in equation (A.11) using the quadratic error estimation. As illustrate in equation (A.9) and (A.10) the error introduced by the calibration of the detector depends on the error of the slope and the difference in ADC. For differences in the order of a few hundred ADC the error introduced from the uncertainty slope is less then one electron volt. For all measurements performed in this thesis this assumption is valid. Therefore the error coming from the calibration of the detector is

neglected. The error estimation for energy differences then simplifies to A.12.

$$\Delta E_{\text{keV}} = E_{1,\text{keV}} - E_{2,\text{keV}} \tag{A.9}$$

$$= (s \cdot E_{1,\text{ADC}} + o) - (s \cdot E_{2,\text{ADC}} + o)$$

$$= s \cdot E_{1,\text{ADC}} + s \cdot E_{1,\text{ADC}} + o - o$$

$$= s \cdot (E_{1,\text{ADC}} - E_{2,\text{ADC}})$$

$$\Delta E_{\text{keV}} = s \cdot \Delta E_{\text{ADC}} \tag{A.10}$$

$$\Rightarrow \sigma_{\Delta E_{leV}} = \sqrt{\sigma_{slope}^2 \cdot \Delta E_{\text{ADC}}^2 + s \cdot \sigma_{\Delta E_{\text{ADC}}}^2} \text{ with } \sigma_{\Delta E_{\text{ADC}}}^2 = \sigma_{E_{1,\text{ADC}}}^2 + \sigma_{E_{2,\text{ADC}}}^2 \tag{A.11}$$

$$\text{using: } \sigma_{slope} \cdot \Delta E_{\text{ADC}} \ll \sigma_{\Delta E_{\text{ADC}}}$$

$$\rightsquigarrow \sigma_{\Delta E_{leV}} = \sqrt{\sigma_{s \cdot E_{1,\text{ADC}}}^2 + s \cdot \sigma_{E_{2,\text{ADC}}}^2} = \sqrt{\sigma_{E_{1,\text{keV}}}^2 + \sigma_{E_{2,\text{keV}}}^2} \tag{A.12}$$

A.4 Current Status of the TRISTAN Project

The TRISTAN project aims to fulfill all the requirements seen in chapter 2.3 using the promising technology of **S**ilicon **D**rift **D**etectors (SDD). The working principle of SDDs is explained in chapter 3.

The high rates of electrons are handled by distributing the count rate among many pixels. The current design is composed of 3486 pixels to divide the high rate among the pixels, resulting in an expected rate of ≈ 100 kcps per pixel. To cover most of the circular electron beam each pixel has a diameter of 3 mm with a hexagonal shape to minimize the non-sensitive area. Even though the pixel size is quite large for semiconductor detectors, the anode itself is very small because of the drift fields involved for SDDs. The diameter of the anode is 90 μm, which results in a tiny capacity of $C_d = 110$ fF and therefore excellent noise performances.

To make the system easier to handle and maintain (e.g installation and/or replacement in case of damage), the entire detector is divided into 21 modules. The full system can be seen in figure A.3 and a more detailed illustration of one module is presend in figure A.4. Each module holds a SDD chip with 166 pixels on top of the T-shaped mounting structure and cooling block. All lanes that provide power and read the signal are included in the waver. A picture of a dummy-waver provided by the Halbleiterlabor der Max-Plank-Gesellschaft [44] can be seen in figure A.5. With adhesive foil the waver chip is mounted to the cooling block. This keeps the SDD in place and allows thermal contact to the cooling block. The contacts on the bottom side of the waver are connected with about 200 bonds of a diameter of 17 μm to a rigid-flex **P**rinted **C**ircuit **B**oard (PCB) on both
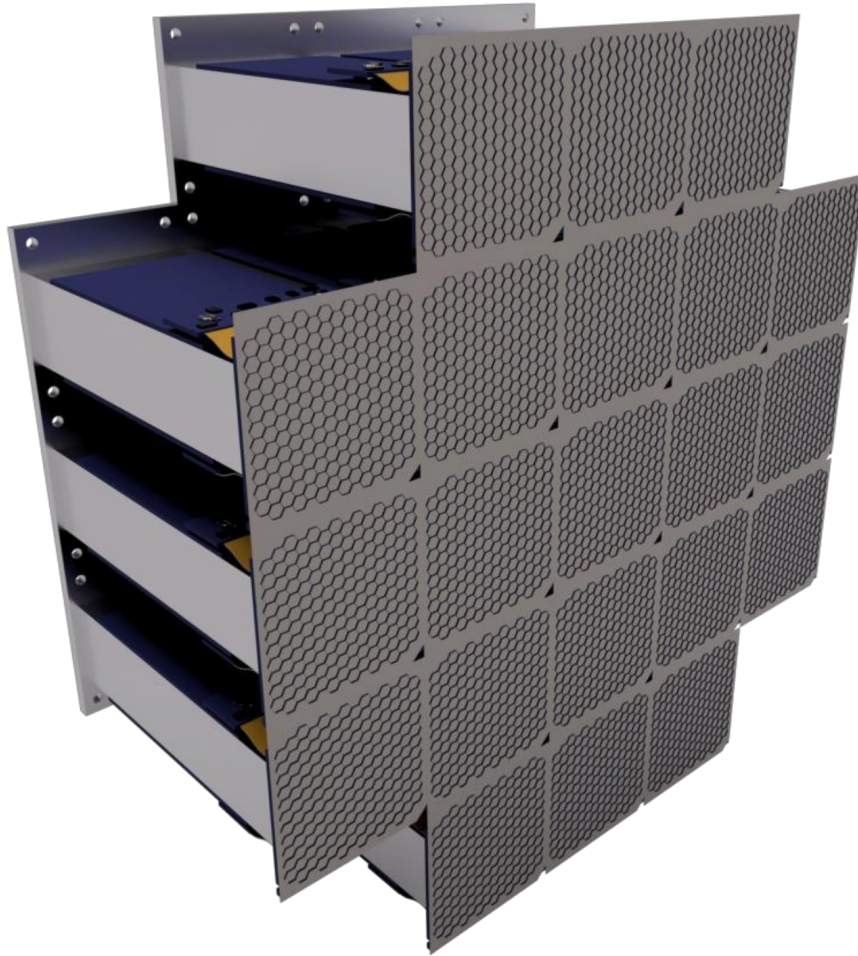
FIGURE A.3: **Preliminary design for the TRISTAN detector system composed of 21 modules**
Each module holds a SDD waver with each 166 pixel ($\varnothing\,3\,\mathrm{mm}$) and two amplification boards. (Plot adapted from [45])

sides of the cooling block. The two PCBs hold the first low-noise amplification stage made of **A**pplication-**S**pecific **I**ntegrated **C**ircuits (ASIC) provided by XGLab [34]. From there the signal is then transported to the **D**ata **A**cquisition **S**ystem (DAQ).
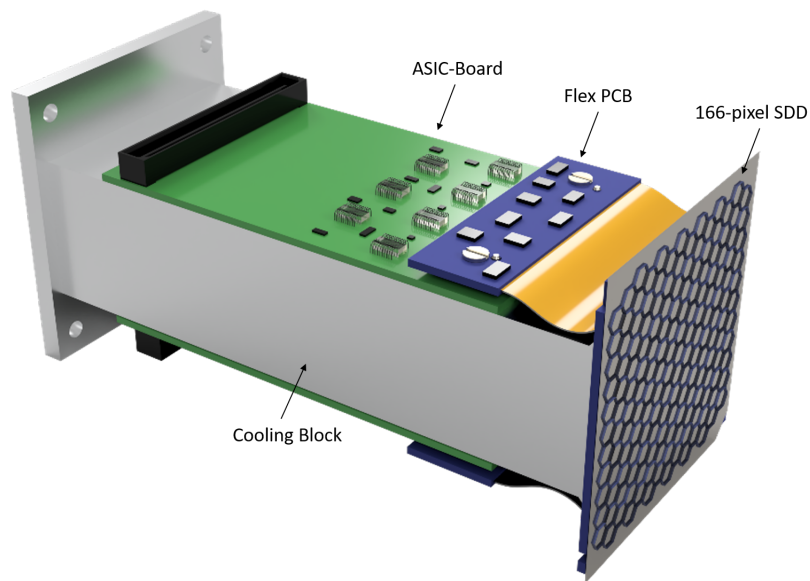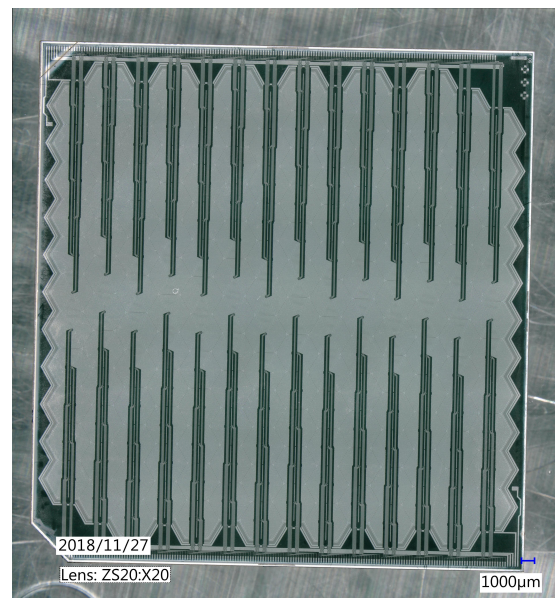
FIGURE A.4: **Perliminary design for a detector module**
In silver the cooling block is shown. At the top of it the SDD chip with 166 pixel is mounted. Two flex PCBs (blue-orange) are bonded with each about 100 bonds to the SDD chip on the bottom side. This adapter then connects the SDD with the ASIC-board (green), containing the first aplification stage. (Plot adapted from [45])

FIGURE A.5: **166 Pixel 'Dummy SDD'**
The 'Dummy SDD' is composed of 166 pixels with a diameter of $3\,\mathrm{mm}$ and made of aluminum. Shown is the chip including the layout for all electric lanes and bond-pads. The detector chip dummy is provided by the HLL [44].

Bibliography

[1] Kerry Whisnant Veron Barger, Danny Marfatia. *The Physics of Neutrinos.* Princeton University Press, 2012.

[2] Kai Zuber. *Nuetrino Physics.* CRC Press, 2011.

[3] D. Decamp, B. Deschizeaux, and J.-P. Lees et al. A precise determination of the number of families with light neutrinos and of the z boson partial widths. *Physics Letters B*, 235(3):399 – 411, 1990.

[4] J. Conrad and M. Shaevitz. *Sterile Neutrinos: An Introduction to Experiments*, chapter Chapter 10, pages 391–442.

[5] S. N. Gninenko, D. S. Gorbunov, and M. E. Shaposhnikov. Search for GeV-scale sterile neutrinos responsible for active neutrino oscillations and baryon asymmetry of the Universe. *Adv. High Energy Phys.*, 2012:718259, 2012.

[6] Raymond Davis, Don S. Harmer, and Kenneth C. Hoffman. Search for neutrinos from the sun. *Phys. Rev. Lett.*, 20:1205–1209, May 1968.

[7] M. Cribier, W. Hampel, and G. Heusser et al. Results of the whole gallex experiment. *Nuclear Physics B - Proceedings Supplements*, 70(1):284 – 291, 1999. Proceedings of the Fifth International Workshop on topics in Astroparticle and Underground Physics.

[8] Y. Suzuki. Solar neutrino results from super-kamiokande. *Nuclear Physics B - Proceedings Supplements*, 91(1):29 – 35, 2001. Neutrino 2000.

[9] N Tolich and. Final results from SNO. *Journal of Physics: Conference Series*, 375(4):042049, jul 2012.

[10] M. C. Gonzalez-Garcia and Yosef Nir. Neutrino masses and mixing: evidence and implications. *Rev. Mod. Phys.*, 75:345–402, Mar 2003.

Bibliography

[11] C Kraus, B Bornschein, and et al. Bornschein. Final results from phase ii of the mainz neutrino mass searchin tritium beta decay. *European Physical Journal C - EUR PHYS J C*, 40:447–468, 04 2005.

[12] V N. Aseev, A I. Belesev, A Berlev, E V. Geraskin, A A. Golubev, N Likhovid, V M. Lobashev, Alexander Nozik, V S. Pantuev, V I. Parfenov, Aino Skasyrskaya, Fyodor Tkachov, and Sergey Zadorozhny. An upper limit on electron antineutrino mass from troitsk experiment. *Physical Review D*, 84, 08 2011.

[13] KATRIN Collaboration and KATRIN Collaboration. Katrin design report 2004. Technical report, Forschungszentrum, Karlsruhe, 2005. 51.54.01; LK 01.

[14] Frank Avignone, Steven R. Elliott, and Jonathan Engel. Double beta decay, majorana neutrinos, and neutrino mass. *Reviews of Modern Physics*, 80, 08 2007.

[15] Johannes Simon Schwarz. *The Detector System of the KATRIN Experiment - Implementation and First Measurements with the Spectrometer*. PhD thesis, 2014.

[16] S. Mertens, T. Lasserre, S. Groh, G. Drexlin, F. Glück, A. Huber, A.W.P. Poon, M. Steidl, N. Steinbrink, and C. Weinheimer. Sensitivity of next-generation tritium beta-decay experiments for keV-scale sterile neutrinos. *Journal of Cosmology and Astroparticle Physics*, 2015(02):020–020, feb 2015.

[17] R. Adhikari, M. Agostini, and N. Anh Ky et. al. A white paper on keV sterile neutrino dark matter. *Journal of Cosmology and Astroparticle Physics*, 2017(01):025–025, jan 2017.

[18] Alexey Boyarsky, Oleg Ruchayskiy, and Dmytro Iakubovskyi. A lower bound on the mass of dark matter particles. *Journal of Cosmology and Astroparticle Physics*, 2009(03):005–005, mar 2009.

[19] Dmytro Iakubovskyi. Observation of the new line at 3.55 kev in x-ray spectra of galaxies and galaxy clusters. *Advances in Astronomy and Space Physics*, 6, 10 2015.

[20] Martin Slezak. Personal programming scripts.

[21] Lisa Schlüter. Development of new methods to include systematic effects in the first tritium data analysis and sensitivity studies of the katrin experiment. Master's thesis, Technical University of Munich, 2019.

[22] Christian Karl. Analysis of first tritium data of the katrin experiment. Master's thesis, Technical University of Munich, 2018.

[23] Kai Dolde. Detector and read-out development to search for sterile neutrinos with katrin. Master's thesis, Karlsruhe Institude of Technology, 2016.

[24] S. Mertens, T. Lasserre, S. Groh, G. Drexlin, F. Glueck, A. Huber, A. W. P. Poon, M. Steidl, N. Steinbrink, and C. Weinheimer. Sensitivity of Next-Generation Tritium Beta-Decay Experiments for keV-Scale Sterile Neutrinos. *JCAP*, 1502(02):020, 2015.

[25] Helmuth Spieler. *Semiconductor Detection Systems*. Oxford University Press, 2005.

[26] Pascal Renschler. *KESS - A new Monte Carlo simulation code for low-energy electron interactions in silicon detectors*. PhD thesis, KIT, Karlsruhe, 2011.

[27] T Brunst, Luca Bombelli, Marco Carminati, C Fiorini, D Fink, T Houdy, Peter Lechner, and S Mertens. Development of a silicon drift detector system for the tristan project—future search for sterile neutrinos. *Nuclear Instruments and Methods in Physics Research Section A: Accelerators, Spectrometers, Detectors and Associated Equipment*, 2018.

[28] Frank Hartmann. *Evolution of Silicon Sensor Technology in Particle Physics*. Springer Interantional Publishing Ag, second edition, 2017.

[29] Norbert Langhoff et al. Burkhard Beckhof, Brigit Kanngießer. *Particle X-Ray Fluorescence Analysis*. Springer Science+Buissiness Media, 2006.

[30] P. Lechner, C. Fiorini, R. Hartmann, J. Kemmer, N. Krause, P. Leutenegger, A. Longoni, H. Soltau, D. Stötter, R. Stötter, L. Strüder, and U. Weber. Silicon drift detectors for high count rate x-ray spectroscopy at room temperature. *Nuclear Instruments and Methods in Physics Research Section A: Accelerators, Spectrometers, Detectors and Associated Equipment*, 458(1):281 – 287, 2001. Proc. 11th Inbt. Workshop on Room Temperature Semiconductor X- and Gamma-Ray Detectors and Associated Electronics.

[31] Peter Lechner. *Zur Ionisationsstatistik in Silicium*. PhD thesis, Technische Universität München, 1998.

[32] Martin Popp. *Untersuchung und analytische Modellierung der Systemantwort von pn-CCD Detektoren*. PhD thesis, Ludwig-Maximilians-Univeristät München, 2000.

Bibliography

[33] Daniel Greenwald. Characterization of the proton source in the frictional cooling demonstration experiment. Master's thesis, Technische Universität München, 2007.

[34] XGLab. Via Conte Rosso 23, I-20134 Milano (Italy).

[35] L. Bombelli, C. Fiorini, T. Frizzi, R. Alberti, and A. Longoni. "cube", a low-noise cmos preamplifier as alternative to jfet front-end for high-count rate spectroscopy. In *2011 IEEE Nuclear Science Symposium Conference Record*, pages 1972–1975, Oct 2011.

[36] Robert Hartmann, Lothar Strüder, J Kemmer, Peter Lechner, O Fries, Eckart Lorenz, and Razmik Mirzoyan. Ultrathin entrance windows for silicon drift detectors. *Nuclear Instruments and Methods in Physics Research Section A: Accelerators, Spectrometers, Detectors and Associated Equipment*, 387:250–254, 03 1997.

[37] JEOL Ltd. Jsm-it300 intouchscope scanning electron microscope, 2019.

[38] Florian Schopper, 2018. private communication.

[39] M.C. Lépy, B. Duchemin, and J. Morel. Comparison of experimental and theoretical l x — ray emission probabilities of 241am, 239pu and 240pu. *Nuclear Instruments and Methods in Physics Research Section A: Accelerators, Spectrometers, Detectors and Associated Equipment*, 353(1):10 – 15, 1994.

[40] Hendrik Ferdinande, G Knuyt, R van de Vijver, and R Jacobs. Numerical calculation of absolute forward thick-target bremsstrahlung spectra. *Nuclear Instruments and Methods*, 91:135–140, 01 1971.

[41] Private Conversation David Radford.

[42] Tobias Eggert. *Die spektrale Antwort von Silizium-Röntgendetektoren*. PhD thesis, Technische Universität München, 2004.

[43] Glenn F. Knoll. *Radiation Detection and Measurement*. John Wiley and Sons, Inc., third edition, 2000.

[44] Halbleiterlabor der Max-Planck-Gesellschaft in München, Contact Person Peter Lechner.

[45] Internal Report presented by Marco Carminati et al., Politecnico di Milano University.

List of Figures

List of Figures

List of Tables

Acknowledgement

This thesis would have not been possible without the help of many other people and I want to thank all of you for the support and encouragement.

First and foremost I want to thank **Prof. Dr. Susanne Mertens** for the opportunity to work at your chair and the scientific research I was able to perform here. I really enjoyed the time in the laboratory and want to thank you for the opportunities that I got to help at other projects and locations to broaden my general knowledge of physics.

I also want to thank **Tim Brunst** for the supervision during my master thesis and the endurance to answer all my questions no matter how random they sometimes might have been. Especially I want to thank you for the support in the laboratory and the really helpful tips if I got stuck in my research.

I am also grateful for the help of **Martin Slezak** concerning many questions about statistics, error propagation and general coding improvements. These mini-lectures in between have really been useful and I want to thank you for the time you have spent for me.

In addition to this I want to thank **Thibaut Houdy** for the support during the analysis of my measurements and the time spent to validate and cross-check my simulations. I also want to thank you for the proof reading of my thesis even though there have been many other things on your ToDo-list.

In the following I also want to thank **David Fink** for the assistance in times of noise reduction and the many advices concerning the electronics of my setup.

For the support and input on questions like the pileup in my measurements I want to thank **Dr. David Radford**. The well documented und nicely explained suggestions have been very useful for me.

Erklärung der Selbstständigkeit

Ich versichere hiermit, dass ich die von mir eingereichte Arbeit zum Erlangen des Abschlusses Master of Science vollständig und selbstständig verfasst habe. Keine anderen Hilfsmitte, als die angegebenen Quellen wurden zum Verfassen dieser Arbeit verwendet.

Declaration of Authorship

Hereby I declare that the submitted thesis to receive the degree in Master of Science, has been written independently and by myself. No other resources than the quoted references have been used to write this thesis.

Daniel Siegmann

München, 15. April 2019